学术展望

ACADEMIC PERSPECTIVES

美国华裔教授学者协会专刊

US CHINESE SCHOLARS ASSOCIATION

ACADEMIC PERSPECTIVES

USA Chinese Scholars Association

Volume 15, 2021

ISBN 1936-1246

Editor-in-Chief

Responsible Editor

Editorial Board

© Copyright Ownership and Viewpoints

目 录

►Humanities and Social Sciences / 人文与社会科学

►Natural Sciences / 自然科学

ACADEMIC PERSPECTIVES

学术展望

人文与社会科学

HUMANITIES AND SOCIAL SCIENCES

Two Tales of a City: An Ethnic and Cultural Study

James J. Lu, PhD

Charles Dickens' novel *A Tale of Two Cities* opens with a proverbial paragraph, "It was the best of times, it was the worst of times, it was the age of wisdom, it was the age of foolishness, it was the epoch of belief, it was the epoch of incredulity, it was the season of Light, it was the season of Darkness, it was the spring of hope, it was the winter of despair…" (1). Dickens' novel, published in 1859, focuses on some extraordinary events taking place in London and Paris during a turbulent time in history. That I allude to the Dickens' title and quote his famous opening passage certainly carries a purpose: to call attention to the two contrastive tales which continue to unfold before our eyes.[1]

The City of Riverside has been taking pride in its cultural heritage preservation, as seen through a considerable list of landmarks designated by the city's Cultural Heritage Board. The official list contains 108 significant landmarks, representing heritages from the various ethnic communities across a wide spectrum. On top of the list stands the Mission Inn which is also listed as a treasure on the national register, Washington, DC. On the same list is the historic Chinatown Site. Although the Chinatown no longer exists as a "town" because there is no visible structure at all, like the Mission Inn it is a site officially recognized at all four levels of the government--the City, the County, the State, and the Nation. In short, it is listed on the National Register of Historic Places (NRHP). Scholars, particularly historians, consider the Riverside Chinatown one of the most important Chinese sites in the United States.

---

[1]This article is a new version rewritten and expanded by James J. Lu, an article based on a conference paper copresented by this author and Vince Moses at Harvard University in 2010.

A SHARP CONTRAST BETWEEN THE MISSION INN AND THE HISTORIC CHINATOWN SITE

Mission Inn is indeed magnificent. To fully appreciate the Inn one really needs to pay a visit in person. The hotel's website offers a charming and fairly accurate self-portrayal, though partly for advertising purposes:

> Surrounded by breathtaking architecture, timeless beauty and old-world charm, [t]he Mission Inn Hotel & Spa welcomes you to a destination where rich history, modern luxury, and classic elegance exist in perfect balance.
>
> Where magnificent grand vistas harbor countless intimate hidden treasures. And where the outside world is left behind, setting a grand stage for memories that will last a lifetime.
>
> For over a century, world leaders and Hollywood stars have chosen The Mission Inn …as a place of refuge and renewal. Originally built as a two-story adobe guesthouse in 1876, the Inn has become the crown jewel of Inland Southern California, occupying an entire city block. (https://www.missioninn.com/)

Now, how does Riverside's Chinatown look like? Unfortunately, it looks completely desolate. It can be described as virtually a wasteland. To understand why, we need a flashback into distant history. Since 1870s, the two tales of a city, Riverside's Mission Inn and Chinatown, have been unfolding side by side. Put explicitly, the two tales may be understood in terms of Dickensian conceptual opposites--the best times and the worst times; the age of wisdom and of foolishness; the epoch of belief and the epoch of incredulity; the season of Light, and the season of Darkness; and the spring of hope and the winter of despair. These paring opposites, of course, should not be taken as absolute or static, because the Mission Inn and the Chinatown, while parallel and contrastive, at times also interrelate and interact. Thanks to the prominence of two charismatic protagonists — Frank Miller and George Wong, these two tales together offer a complex dialogue which Mikhail Bakhtin would consider "dynamic" and "polyphonic." Other factors involved (social, cultural, historical and political) have been shaping forces in the development of the two tales.

A FLASHBACK: EARLY CHINESE AMERICAN SETTLEMENT IN RIVERSIDE

The California Gold Rush of 1848 drew thousands of Chinese from Guangdong and Fujian to a place they called "Gold Mountain" — California. Thousands more came to this

new State to build the Union Pacific Railroad in the 1860s. Driven from the gold fields by violence and the foreign miner's tax, they moved on to work on the Central Pacific Railroad. Between 12,000 and 14,000 Chinese worked on the construction of the Central Pacific. They were paid from $25 to $35 per month for strenuous labor, which included blasting rock and laying track through the High Sierras. The death toll was heavy, but Chinese courage, skill, and endurance accomplished an early completion of the transcontinental railroad (See, 1996).

Completion of the transcontinental railroad in 1869 furloughed thousands of Chinese laborers at a time when California agriculture needed a massive labor force. Access to the seemingly tireless Chinese workers enabled growers to change from extensive low-care farming to labor intensive cultivation of specialty crops that yielded greater profits. Many immigrants from Guangdong possessed superior orchard and truck gardening skills, the result of centuries of farming the fertile region of southeastern China. The Chinese applied their skills to California agriculture in various capacities, as truck gardeners, vegetable peddlers, farm cooks, ranch foremen, harvest laborers, commission merchants, large-scale tenant farmers, and owner-operators (Chan, 1986; Moses and Focht, 1985).

According to historical records, the City of Riverside was founded in 1870. The next year 1871, a group of Chinese immigrants arrived in Riverside for a place to live and labor. In "A Selected Chronological History of Chinese Pioneers in Riverside and the Southern California Citrus Belt," UCR scholar Harry Lawton narrates: "[In] 1871--New Settlers arrived almost daily in Riverside to establish ranches. Chinese cooks, servants, and field hands are among the first settlers" (*Wong, An American Chinatown*, 60-61). Three years later, in 1874, Christopher Miller, father of Frank Miller who later became the owner of the Mission Inn, brought his family to settle in Riverside for business opportunities. Biographer Maurice Hodegen describes the Miller family's trip almost cinematically: "…Christopher Miller left the [Wisconsin] village for California in bitter February weather of 1874…. In the dimness of a rising moon the horses hauled the wagon up from the river onto a mesa and to the settlement called Riverside" (*Master of the Mission Inn*, 2015). In the new city, the Millers and the early Chinese immigrants were, likewise, looking for a better life.

In the 1870s, citrus, a second kind of gold rush pulled the early Chinese immigrants to the new city Riverside, originally the hometown of the famous Washington Navel Orange. Between 1885 and the early 1930s, early Chinese pioneers lived and worked in this citrus town. They established a flourishing Chinatown of more than 450 full-time residents, and housed an additional 2,500 during harvest season (Moses and Focht, 1985; Lawton, 1987).

Riverside's Chinese pioneers belonged primarily to the Taishan District Association, from regions immediately around the mouth of the Pearl River on the Canton Delta. They

were almost all members of the Wong Family Association and from Gom-Benn village. The Chee Kung Tong, a Triad Society, had a chapter headquartered in Riverside's Chinatown (Wong, 1987). In 1879 the first Chinese were reported to be working in the raisin packing sheds. The year 1880 found the Chinese migrant laborers replacing Native Americans as agricultural workers. The citrus and grape crops did not have conflicting picking seasons; the grape harvest preceded the citrus harvest. The citrus industry soon felt the impact of the Chinese labor force. Finally, some Chinese workers were able to find almost continuous employment in one geographic area with different agricultural crops. This situation enabled them to maintain the same residence for eight months of a year and took some of the migrant quality out of their lifestyle (Chan, 1986; Moses and Focht, 1985).

Cultivation of a number of citrus varieties was a precautionary measure against the kind of disaster which had happened with the mono-variety potato crop in the 19th century Ireland. Citrus seedlings planted in the groves around Riverside included the Chinese Mandarin orange. Growers discovered, however, that none of the varieties brought from China were successful in the Riverside environment. The stock of a new orange variety from Bahia, Brazil, which came into the Riverside area via the United States Department of Agriculture, proved to be absolutely correct for regional climate and soil. Nevertheless, the Chinese did assist with the experimental development of methods for cultivating and caring for the variety and provided the intensive labor necessary to grow it (UC, *The Citrus Industry*, Vol. 5, 1989).

In Riverside, Chinese ranch "cooks" and harvest laborers assisted growers with planting, grafting, pruning, fertilizing, tilling, irritating, and various other aspects of navel orange production. The Chinese offered suggestions for solutions to insect control. For example, during the 1880s the Duey Woo Lung Company suggested an established Chinese method of pest control for the Cottony Cushion Scale. This company proposed that local growers subscribe to them for Chinese workers to hand wash the leaves of every tree in the city. The proposal was met with horror by the local anti-Chinese agitators (*Wong, An American Chinatown,* 1987).

Riverside had become a principal shipper of citrus fruit in the United States; during 1890 more than 487,882 boxes of oranges and other citrus crops were packed. By combining Chinese knowledge and labor with professional promotional techniques, the 1895 Riverside citrus growers had made their community the richest city per capita in the United States. Land prices shot up, which reinforced the "need" for a low wage Chinese labor force to continue intense cultivation of the "highly profitable" Washington Navel orange. One innovation of the Chinese became known as the "Chinese pack" — a method that allowed a

worker to pack various sizes of fruit and still achieve an even top layer.

Riverside's citrus industry, built on the backs and with the brains of the Chinese, helped capitalize Southern California and turned the city into a mecca for world-wide citrus research and technology. Sunkist Growers, Inc., the Citrus Experiment Station of the University of California, citrus packing house machinery, orchard heating, and a host of related developments all originated in Riverside. The citrus industry was not the only route to economic security for Riverside's pioneer Chinese. The Chinese truck farmers for around 50 years supplied Riverside residents with vegetables. These crops were grown in the fertile soil of the Santa Ana River bottom land. The Chinese entrepreneurial spirit expanded into other enterprises such as the laundry business. The Duey Woo and Hong Woo laundries in Riverside dried the clothing on racks behind the shops. Efforts in the 1880's and 1890's to stamp out Riverside's Chinese laundries met with failure. Duey Woo Lung even forced one competitive Anglo steam laundry into bankruptcy (Moses and Focht, 1985).

ANTI-CHINESE AGITATION AND THE CHINESE EXCLUSION ACT OF 1882

As mentioned earlier, after the city of Riverside was established in 1771, the Millers and the early Chinese immigrants were arrived almost at the same time; they were looking for a better life. But due to their different ethnic identities and social status, their subsequent experiences differed vastly. While the Millers enjoyed respect and prestige, the Chinese early immigrants had to confront racism often in violent forms.

Because Chinese language, culture, religion, and race militated against the acceptance by the dominant white culture, the early Chinese immigrants were treated badly, although citrus growers supported the Chinese presence, due to their skills and labor. Most Chinese men immigrating to Gold Mountain, including Riverside, retained their traditional customs including their dress, shaved forehead, and queue ("pigtail"). In China, the shaved forehead and queue were required signs of subjugation to the Manchu dynasty. By the same token, powerful traditions, coupled with a desire by immigrants to return home, were barriers to melding with the host culture. The results proved tragic for any of these strangers in an alien land. At the same time, immigrants to Gold Mountain maintained strong ties with their families and villages in China, including Gom-Benn. Through Taoist and Confucian rituals, festivals, and practices, they reinforced their memories of home and reminded themselves that they were "sojourners" in a strange land. Temples, or "Joss Hoses," were nearly always built in Chinatown. They were financed by public subscription or through large individual donations. Many were dedicated to Guan Gong, the God of War, who symbolized both

martial valor and brotherly devotion. Riverside was no exception to this rule.

By 1882, anti-Chinese agitation led by recent Irish immigrants, under the rubric of the Workingmen's Party, had become so widespread in America that the United States Congress passed the Chinese Exclusion Act, which prohibited Chinese laborers from entering the country. Congress renewed the exclusion in 1892 as the Geary Act. These acts would lead to the demise of most local and medium-sized Chinatowns throughout the country by the 1920s. Riverside's once thriving town took the same turn. The last lone resident of the town died in 1974, and the last structures on site were demolished by a prospective developer in 1977 (Saxton, *1975)*.

THE ESTABLISHMENT OF RIVERSIDE HISTORIC CHINATOWN

The historic Chinatown was established by early Chinese pioneers in 1885, also known as the second Chinatown in Riverside, for there had been a Chinese Quarter in downtown, a smaller, less concentrated section located the north side of Ninth Street between Main and Orange streets. From 1871 to 1885, the Chinese residents worked and lived there, but as anti-Chinese violence spread, particularly after the 1882 Chinese Exclusion Act became a federal law, they were forced out of downtown to settle on the city's outskirts, currently along Tequesquite between Brockton and Pine Streets. There they survived, and continued to work diligently. Over the years, the Chinatown gradually became a flourishing community. It normally housed around 450 full-time residents, and an additional 2,500 during the harvest season from January through April. The Chinese pioneers made great contributions to the City of Riverside. For example,

- They contributed horticultural techniques brought with them to California from the citrus-producing regions of southern China, including furrow irrigation (claimed as the "Riverside Method"), pattern packing of fruit, called the "China Pack," and insect pest control techniques for scale pests. They were also the chief skilled labor force for the Inland Citrus Belt. It is fair to say that they were instrumental in making possible the rise of Riverside's famous navel Orange Empire.
- Furthermore, as the Chinatown developed, some of its residents became labor contractors, merchants, businessmen, as well as vegetable growers and dealers in all the Riverside citrus districts, providing a strong middleman minority that helped build up Riverside as a powerful economic and cultural capital of southern California, rivaling Los Angeles at the time,
- The Chinese Remittance Banker, Wong Sai Chee, served more than 2,500 of

his countrymen in Riverside and San Bernardino, and acted as a liaison with the Anglo citrus barons of Riverside, creating a solid bridge between the two cultural groups.

• Duey Woo Lung Co., a laundry owned by Wong Nim, provided the best laundry service in the Riverside area for many years.

THE STEADY AND RAPID ASCENT OF THE MISSION INN

The Mission Inn evolved from the Glenwood Cottages built in 1876 which Frank Miller later purchased from his father and spent years to improve before redesigning it into a grand hotel. Opened in 1903, the Mission Inn became an instant sensation near and far, its name reflecting owner Frank's passion for Mission Revival, an architectural style inspired by the late 18th and early 19th century Spanish missions in California. As soon as the Inn was opened, Frank Miller received virtually a delightful advertising gift: President Franklin Roosevelt visited the Inn on May 7, 1903. In the following 30 or so years, the Mission Inn saw the best of times. As Maurice Hodgen notes in his *Master of the Mission Inn* (2014), only did the Inn continue to expand, adding the Mission wing, the Cloister Wing, the Spanish Wing, the Gallery and the Rotunda Wing, but the luxury hotel also steadily became a prestigious gathering place for politicians, artists, entrepreneurs as well as travelers in general. Readily accepted by the mainstream society and culture, the Mission Inn along with Frank Miller enjoyed advantages that neither the early Chinese immigrants nor their Chinatown could even dream of. Between 1903 and earl 1930s, for the Mission Inn and for Frank Miller, it was the best of times, the age of wisdom, the epoch of belief, the season of Light, the spring of hope.

In an article titled "Grande Dames: Historic hotels in California," scholar Lydia Kremer observed:

Working with prominent architect Arthur Benton and financed by railroad baron Henry Huntington, Miller opened the first wing of the current Mission Inn building in 1903…For 30 years, it evolved with new wings that reflected various architectural trends and the work of several California architects including Arthur Benton, Myron Hunt and G. Stanley Wilson… In 1977 — thanks to the efforts of Friends of the Mission Inn as well as government officials — the inn was designated a National Historic Landmark, sparking a $50 million renovation in the 1980s. (*Desert Sun*, 2015)

According to the website of *Evergreen Memorial Historic Cemetery*, "Presidents as well as barons of business enjoyed the Inn. In the early days these included Benjamin Harrison, William McKinley, Theodore Roosevelt, Taft, and Herbert Hoover. In later years, it

included both Nixon and Kennedy as well as Ronald Reagan, who honeymooned there with Nancy" (http://evergreen-cemetery.info/people/frank-augustus-miller/).

THE MISFORTUNES OF EARLY CHINSE PIONEERS

As the Mission Inn arose to become increasingly charming, historic Chinatown site continued to decline. After they first arrived in Riverside, the Chinese pioneers frequently experienced hard times marked by hatred and violence against them. Despite their significant contributions to the city's economy and cultural diversity, they were treated not only as strange aliens with weird exotic customs, but worse, as heathens and usual suspects of immoral acts. In 1892, the US Congress passed the Geary Act, a renewal of the 1882 Chinese Exclusion Act, to continue excluding the Chinese immigrants from naturalization and prohibiting their wives from coming over for family reunion. The Geary Act went further, requiring all Chinese residents in the US to carry a certificate of residence, or they would be subject to deportation or one-year imprisonment. Such worsening conditions, local and national, caused the demise of most Chinatowns throughout the country by the 1920s. Riverside's Chinatown, as a result, suffered drastic decline. Many residents left to scatter elsewhere. In short, for the early Chinese pioneers, those few decades could be considered perhaps the worst of times, the age of foolishness, the epoch of incredulity, the season of Darkness, and the winter of despair.

UNIQUE INTERETHNIC CONTACTS

It was against such a backdrop that in 1914 George Wong (his Chinese name was Wong Ho Leun) emigrated to Riverside to join his father who had been living and working as a laborer in Riverside. Upon arrival in the Chinatown, although facing a broad adverse environment, Ho Leun, at the age of 14, had his aspirations. First of all, he wanted to help his father. From the records kept by the Evergreen Cemetery, we know that the teenager soon found a job as a houseboy. His master was Stephen Herrick, a real estate developer and founder of both the East Riverside Land Company and East Riverside Water Company. It was Herrick's wife who gave Ho Leun the English name "George." George attended the Chinese Mission School, and later even taught English to younger Chinese children. A graduate of 1923 class from Poly High School, he attended Riverside City College. He had to drop out because someone falsely accused him of selling drugs. Eventually, he was exonerated, but the painful experience discouraged him from returning to finish college (http://

www.evergreen-cemetery.info/founders.php?id=25312). Several sources indicate that George Wong worked in the Mission Inn as a cook (Evergreen, etc.). Although not much detail is available of George's time spent working in the Inn, this episode of the story is historically and narratologically significant. George Wong and Frank Miller must have come very close to each other in real life. They could have even met in the Inn.

In fact, the year George Wong emigrated to Riverside was the same year when Frank Miller warmly received Booker T. Washington in the Mission Inn. Washington was a former slave who, after emancipation, made himself a prominent African-American educator and social activist. Back then in the early 19th century, befriending a black man in public would not be viewed kindly. By doing that anyways, Frank Miller proved himself a progressive visionary ahead of his time. He also gave moral support to the Japanese immigrant Jukichi Harada when the latter in 1918 fought a legal batter for the right to own a home in Riverside through his American-born children. Biographer Zona Gale observed in 1938, "He [Frank Miller] had great feeling and fondness of other races…" (131). It must be with that same feeling, the same fondness that Frank hired George Wong as a cook and other Chinese immigrants as employees for his hotel. In addition, as an art collector, Frank sought artifacts from different parts of the world, including Asia. He brought back from China, among other antiques, the famous Nanking Bell. [See PowerPoint Picture 12?]. Biographer Hodgen has written a book intended to explain the significance of Miller's Asian collection: "Many asked about the unexpected Asian emphasis in decoration, furniture and architecture. In response I wrote a book — 130 pages — called *More Than Decoration, the Asian Objects at the Mission Inn.* Using the best scholarship I describe fifty significant artifacts in detail and have included an essay interpreting Miller's attraction to things Asian." Although Hodgen's book does not seem to have been published, the point is clear: that in his life time Frank Miller liked and respected different cultures.

One would wonder if Frank Miller might have invited George Wong into his Rotunda Wing to look at the Chinese decorations and the Nanking Bell, or if George, during his work as a cook in the Mission Inn, found himself naturally attracted by all the Chinese artifacts on display in the hotel. Regardless, it is known that in his later years George Wong became himself a passionate collector: he collected more than 40 cars in addition to many Chinese antiques and artifacts. Equally interesting is the fact that after purchasing the Chinatown property in a court sale in 1941, George built a restaurant called Bamboo Gardens on the site where he lived largely alone. The idea of running a restaurant on the Chinatown must have resulted at least partly from his previous experience as a cook in the Mission Inn. That George Wong refused to leave Chinatown but instead bought and protected it as his

permanent home while other residents left due to extreme social pressure and financial hardship made him almost a hero. Just as Frank Miller has become a shining symbol of the Mission Inn, so has George Wong of the Chinatown. At this point, it is important to point out that during World War II, because China joined the Allied Powers, President Franklin Roosevelt signed the Magnuson Act that repealed the Chinese Exclusion Acts, thereby lifting the restrictions on the Chinese from being considered as American citizens. The subsequent 1952 McCarran-Walters Act and 1965 Immigration and Naturalization Act further improved the social conditions for Asians ("Golden Venture," http://www.goldenventuremovie.com/Chinese Immigration.htm). Significant changes in the larger social context for a minority group could make a huge difference in their personal lives. In 1961, the City of Riverside decided to honor George Wong by naming a short street near the Chinatown "Wong Ho Leun" in Chinese and "Wong Way" in English. Seven years later, in 1968, the County of Riverside recognized the Chinatown as a Historical Landmark before the State of California in the same year designated it as a State Point of Historical Interest. Only during and after World War II did a breeze of "spring of hope" finally arrive for the Chinese immigrants in the U.S.

THE INTERSECTIONS BETWEEN FICTIONAL AND REAL WORLDS

In the fictional world, a story, however long or short, usually ends if and when the protagonist dies. In his theory Bakhtin advocates the open-endedness of the novel as a genre, but in most novels that open-endedness can find suggestive meaning only in a definitive narrative closure. In the real world, even after a historical figure or legendary person long passed away, life would go on, and the closely - related people or things would continue to extend the story. Now, in real life and in our historical tales, what has happened to the Mission Inn after Frank Miller died in 1935? And what has happened to the Chinatown after George Wong passed away in 1974?

In the case of the Mission Inn, Steve Lech and Kim Jarrell Johnson, authors of a book titled *Riverside's Mission Inn*, describe Frank Miller's passing in June 1935 as "the end of an era" (8). Over the next 50 or so years, the hotel continued to function as a local treasure, but not without some extraordinary difficulties. For example, after changing hands twice with new owners, the Inn faced an aging problem in its structure, as well as a far less desirable management. Then, in 1984, it was closed for renovation, but what was expected as a two-year renovation lasted for seven years. In spite of those difficulties, both the government and capable groups always came to its rescue. So write Lech and Johnson, "In 1969, the friends

of the Mission Inn formed to help save the aging structure. The City of Riverside purchased it in 1976 and formed the Mission Inn Foundation to oversee its operation" (8) Indeed, the current owner, local businessman and entrepreneur Duane R. Roberts, who bought the renovated hotel in 1992, is best known as the "Keeper of the Inn." That is why and how the Mission Inn has managed to retain its charm, its magnificence. Arguably it is more gorgeous today than ever.

In the case of the Chinatown, there has not been such luck. After George Wong's death, the last structure on the site was demolished by a prospective land developer in 1977, despite the site's designations as an important landmark of the City, of the County, and of the State (Saxton, *1975)*. In 1980 the Office of the Riverside County bought the land, yet instead of preserving it and making it a decent educational site for students to learn of an important part of the city's history, the site since then has remained a barren, dirty, deserted, and debris-filled wasteland. Meanwhile, competing for space property, commercial developers have been eyeing its potential use for business. Attempts to commercialize the site continued even after the 1984-85 limited archaeological excavations which led to the recognition of the site as a national historic place listed on the National Register. In 2008, developer Doug Jacobs entered into escrow with the County Office of Education to buy the land and construct a 65,500 square-feet medical office building on it. Riverside citizens of different ethnic backgrounds, particularly the Chinese and Chinese-American communities, gathered over 4,000 petitions against the project; they spontaneously organized the Riverside Chinese Culture Preservation Committee (RCCPC) to prevent a complete erasure of Riverside's historic Chinatown under the name of necessary commercial development. Nonetheless, the Riverside City Council unanimously approved the Jacobs project. A lawsuit followed, filed by a new organization Save Our Chinatown Committee. SOCC won the case, thereby putting a stop to the commercial development of the Chinatown site. However, the historic stie remains a ruined and miserable wasteland. Ideally, the site should be cultivated into a Chinese American memorial park, but the risk of this nationally-significant historic yet long-neglected, largely-abandoned to be completely erased remains high.

Charles Dickens' historical novel *A Tale of Two Cities* carries profound social and moral messages. One such message is a moral lesson: that discriminatory practices such as the Poor Law enacted in London during Dickens' time could cause unrepairable social damage, whereas caring for the poor and marginalized can bring hope, transformation, and spiritual redemption. A visit to Riverside City's government website probably gives a ray of hope. Under the web page "City of Arts & Innovation: History of Riverside," we find the following instructive passages:

Riverside is fortunate to have a wealth of sites and buildings that provide a link to the city's past and a strong sense of place. This is the result of the hard work and careful planning of the city's Historic Preservation Program. Created by the City Council in 1969, it identifies and advances the preservation of Riverside's historic neighborhoods, and civic and commercial resources.

Examples include the Mission Inn, the Chinatown site, the National Packing House, Citrus Experiment Station and engineering feats like the Gage Canal. *(http://www.riversideca.gov/visiting-aboutriv.asp)*

Let's hope that by placing the Mission Inn and the Chinatown site together as two quintessential examples of the city's historic preservation goals and accomplishments, the Riverside government, along with its citizens, will eventually find the best way to balance cultural preservation and commercial development with respect to the future of the Chinatown site. The two tales of a city should not be diverged to the extreme: one with a heart-breaking gloomy ending, while the other with what seems to have been relatively too-easy an elevation of magnificence as well as a "living happily ever after" scenario.

REFERENCES

Chan, Sucheng. "This Bittersweet Soil: The Chinese in California Agriculture,1860-1900." University of California Press, 1986.

Dickens, Charles. A Tale of Two Cities, Independently published, 2020. Print.

Gale, Zona, *Frank Miller of Mission Inn.* Appleton-Century Company, 1939. Print.

Hodgen, Maurice. *Master of the Mission Inn: Frank A. Miller, a Life*. Ashburton Publishing, 2014. Print.

Kremer, Lydia. "Grande Dames: Historic hotels in California." *Desert Sun.* April 28, 2015. "Frank Augustus Miller." *Evergreen Memorial Historic Cemetery*. http://evergreen-cemetery.info/people/frank-augustus-miller/.

Lawton, Harry W. (1959). *Riverside's Pioneer Chinese.* A Collection of Newspaper Articles by Harry W. Lawton, with an introduction by George Wong. On file at the Riverside Metropolitan Museum, Riverside, CA. 1987 Riverside's First Chinatown and the Boom of the Eighties. In *Wong Ho Leun, An American Chinatown*, Vol. 1, History, pp. 1–52.

Lech, Steve & John, Kim Jarrell. *Riverside's Mission Inn*. Arcadia Publishing, 2006. Print.

Moses, Vincent, and Brenda Buller Focht, 1991 *Life in Little Gom-Benn: Chinese*

Immigrant Society if Riverside, 1885–1930. Riverside Museum Press, Riverside, CA.

Moses, Vincent, and Kate Whitmore. “Table of the Dragon: Foodways of the Overseas Chinese of Riverside, 1885–1920.” In *Wong Ho Leun, an American Chinatown*, Vol. 2, Archaeology, pp. 249–258. Great Basin Foundation, San Diego, CA.

Saxton, Alexander. *The Indispensable Enemy: Labor and the Anti-Chinese Movement in California First.* University of California Press, 1975. Print.

See, Lisa. “On Gold Mountain.” http://cprr.org/Museum/Chinese.html

Wong, Ho Leun. *An American Chinatown* (History, Volume 1; Archaeology, Volume 2). Great Basin Foundation, 1987.

彼岸·江南

丁凌

江南
彼岸的江南
总是在
梦里的深深浅浅

春的柳浪
夏的风荷
秋的湖月
冬的残雪

不断的断
不孤的孤
不长的长

晚钟莺啼
桂雨流霞
那些江南的点点滴滴啊
总是
在思绪间辗辗转转

彼岸
江南的彼岸
吴语依旧
笑意嫣然
相互间的一句
“我是杭州人”
眼神里都透露着
亲切的喜欢

干炸的响铃
宋嫂的鱼羹
龙井的清香盈袖
西子的旗袍微摆
彼岸的江南
就这样来到了
江南的彼岸

江南
遥望着彼岸
紧紧拽着风筝的线
彼岸
念叨着江南
恋恋不舍
一线挂牵
飞得再远
都是五里一徘徊

两处的牵连
万般的依恋
茶香日醇
衣带渐宽
都在彼此的心心念念

彼岸的江南
湖光山色
那是我们的故乡
江南的彼岸
棕榈海蓝
这有我们的家园

故乡、家园
彼岸、江南
注定了
一生一世的
梦萦魂牵
……

浅议“金融为实体经济服务”

陈岳云 ▶ 洛杉矶西来大学

摘要

本文探讨了为什么中国金融业没有很好地为实体经济服务。指出对中小型和民营公司的融资，与它们对经济的贡献相比，不成比例。此外，与发达国家相比，直接融资（非金融公司发行股票和债券）非常低。因此，要解决金融业服务不足的问题，中国需要解决这两个问题。此外，中国民营银行很少，导致融资短缺，因此中国应该进一步开放金融业，允许拥有更多的民营银行。文章最后指出，进一步解放思想，坚持实事求是，既要注意防右，更要特别注意反左，将是解决所有问题的关键。这也是中国最重大的历史经验和教训。

关键词：实体经济，中小型民营企业，融资难，防右反左

金融为实体经济服务，中国已讲多年，近来更加强調並且提到更重高度，說明其重要性并间接意指收效不佳，至少未达要求。金融的本质是为经济服务，主要是，特别是为实体经济服务，否则就如无水之渔，无地之楼，无根之木。由此产生了若干相关的问题：怎么定义实体经济？中国金融没有很好服务实体经济吗？为什么金融行业对服务实体经济缺乏主动性和积极性？如何才能促进其更多更好地服务于实体经济？

实体经济一般指包括各种产品和服务的生产、消费及流通的各种行为和活动。有别于金融经济，此为单纯的金钱交易，包括金融资产所有权转移的服务。按此定义，所有经济体，包括美国这样的发达经济体，实体经济占绝对的多数，中国更应如此。换句话说，非实体经济或金融经济在整个经济中占很小的比例。以美国为例，整个金融行业包括银行、保险、风投、证券等的 GDP 产值只占总 GDP 的约 7.8%。金融以服务为生，若金融没有以服务实体经济为主，那么其服务谁了？确有各种金钱交易需要

金融服务，例如若干投资人有边际（margin）帐戶，需借钱作投资，但这样或类似的借贷总额是非常有限的。因此可以这样说，不管怎样的经济体及其状况，其金融都是在主要为实体经济服务。中国亦不可能有例外。

既然如此，为什么中国仍在不断讨论强调金融应该为实体经济服务呢？原因应为如下几个方面：首先是实体经济定义不同，把若干行业排除了。比如，经常所说的，“电子商务挤垮了实体经济”,“房地产业的发展损害了制造业”, 这里，直接地把电商和房地产业排除实体经济之外了。从而，金融为这类企业服务，就是在支持非实体经济。

其次，若干行业、企业、群体或地区没有得到金融的有效或均等服务。这应该是问题的根源或起应。中国共有 2 千多个县或县级市，目前中国共有农村信用社约 800 个，村镇银行 1 千 700 个 , 农村商业银行 1 千 500 个。以此推算，中国极大部分县及乡镇没有农村信用社，仍有相当多的县或乡镇没有村镇银行。这就是金融服务的不全面，不均衡。

金融难，特别是贷款难，主要是中小型和微型企业贷款难，私有或民营企业贷款难。据调查，中国中小企业因无法落实担保而拒贷的比例高达 23.8%，因没有落实抵押而发生拒贷的比例达到 34.3%，二者合计总拒贷率高达 58.1%。在中国经济中，中小、微型企业占全国企业总数的 99.3%, 创造的最终产品和服务价值占总 GDP 约 60%，上缴税收约为税收总额的 50%，提供了 75% 以上的城镇就业岗位。但中小企业从国家银行系统中获得的贷款占整个企业贷款的比例不足 30%。民营（私营）企业贡献了全国税收的 50% 以上，创造的 GDP、固定资产投资以及对外直接投资均超过 60%，民营企业中的高新技术企业占全国高新技术企业的比重超过 70%，民营企业城镇就业人数占全国城镇就业人数的 80% 以上，民营企业对新增就业贡献率达到 90%, 但其贷款占整个企业贷款的比例不足 40%。

中国每年货币供给甚高，M2 每年供给大大超过了发达国家水平。根据有关资料，按相比性计算，中国每年的 M2/GDP 比率超过 200%, 美国约为 100%。那为什么中国许多企业仍感货币短缺，贷款难呢？主要原因包括：外贸盈余转换成了人民币 , 国家重点项目及重大工程建设投资，大中型国有企业的借贷及各地方政府项目的建设资金，从而留下来，能借贷给中小企业，特别是中小民营企业甚少。

中国企业融资难的另一个直接重要原因是融资渠道受限，特别是企业直接融资比例低，要求高。美国企业直接融资（发行股票及债券）的比例约为 70-80%，在债务融资中，银行贷款约占 20%。而中国企业直接融资平均比例只占约 20-30%，中小或民营企业的比例更低。债务融资更依赖银行贷款。这样，万众企业都需走银行借贷这一独木桥，

难免拥挤不堪。

要从根本上解决企业融资难的问题，就要大力发展股票债券市场，改革调整股票上市规则和要求，规范、更好监管企业财务审核审报，扩大各种机构 / 财务基金在股债市的投入和占比，从而逐步提高企业直接融资的比例，减少对银行贷款的依赖。

要解决融资难的问题，就要创设更多的银行 , 直接服务于急需而未能获得有效覆盖的地区 , 企业及个人。比如前面提到的，许多县级及乡镇，仍然没有相应的信用合作社或乡镇银行。极大部份中小微企业，无法获得银行贷款。美国设有小型企业管理局，对小微企业提供各种支持和服务，特别是提供贷款和担保，从而使众多缺乏信贷资质的企业，特别是初创企业能无足够自我或第三方担保的情况下简易快速获得贷款。这也是美国创新创业持续不断发展和成功的一个重要原因。这一经验和做法值得中国借鉴。

要解决融资难，很重要的是，要大力支持发展民营银行。在中国约 4 千 700 家各种银行中，共有近 120 家外资法人銀行，但只有约 20 家民营银行。吸引外资，包括吸引外资银行，对中国经济发展很重要，更是中国改革开放的象征和成功的标志。银行业对外资开放，为什么不能更多更大地对民营企业开放？中国有大量的民间资金，更有众多有实力的企业，开放开设更多的更多样化的不同层次及服务对象的民营银行，应是解决实体经济融资难的根本之道。中国四十多年经济社会的巨大飞跃 , 得益于伟大的改革开放，更直接得益于市场经济的发展，特别是民营经济和民营企业的蓬勃成长和发展。中国金融业的未来，也有赖于更多更大更好的民营银行的崛起。外资银行值得信赖和支持，为什么中国自己的民营银行不值得信赖和扶持？

纵观中国经济和金融发展史，是民间经济，民间或民营银行，引领了各种创新，使金融服务遍及天涯海角，长城内外，大江南北，乡村城镇，从而普惠大众，直接服务各种企业和个人，促进整个经济和社会的有序有效运转。在历史上，山西的民营银行能昂立服务全中国甚至触及邻邦，上海十里洋场众多的民营银行能经得起富有名气实力的洋行的竞争仍能稳定发展，充分说明中国有充足的民营银行成长发展的良好土壤和条件。万事俱备，只欠东风。这个东风就是政策松绑，支持鼓励更多更大民营银行的创办和发展。特别是要解放思想，彻底改变观念，要像相信国有银行那样相信民营银行，要像支持鼓励外资银行那样支持鼓励民营银行。中国历朝历代有能力掌控民营金融，当代中国更应有能力和自信这样做。

人们在讨论金融没能有效服务实体经济时，往往是指经济实体特别是工业或制造业融资摊。这应该是事实。许多中小型制造企业，所需的资金比其他行业大，投资周

期较其他行业长，且制造业竞争激烈，近几年成本上升快，获利低，这些因素决定了企业乃至整个行业的融资难。特别是众多民营制造企业更是如此。然后，制造业的发展，不仅要解决有效资金供应问题，更要首先解决产能过剩，产业落后，产品质量，规模经济不足及过度竞争等问题，才能使资金投入更有效且有较低或有限的风险。本人作过一项研究，收集了中国，美国，德国及日本几十年的各种相关资料，得到的基本结论是，中国制造业短期内的稳定发展，主要仍靠出口导向，因此必须继续鼓励出口，开拓更多元化的国际市场，提高产品质量和等级，增加产品品种，控制、降低成本，不断提高竞争力。中长期内，则要学习美国和日本，以提高生产力和投资回报率为核心，从而稳固制造业，吸引更多投资，并提升竞争力，从而提升制造业在国际上的地位。另外，如本人在几年前的一篇文章中所详细阐述的，中国发展制造业，创新和供给侧结构性改革，应集中于大力支持和发展进口替代型制造业。芯片产业，光刻机等，均为此例。

近来人们议论较多的另一个话题是个人消费金融。根据有关研究，中国消费金融近几年增长迅速，尽管消费金融占 GDP 的比率仍比发达国家低，但快速增长的势头，带来巨大的潜在金融和经济风险。据分析，中国消费金融年增长率，是居民平均可支配收入年增长率的近两倍 , 值得引起注意并采取必要的措施，防范破解可能的风险。美国 2007 年的金融和经济危机，就是由消费金融引起的，称作次贷危机。但有人据此而归罪于网贷及网贷公司，似乎有违事实。近几年网贷行业发展太兴猛，渔龙混杂，这是事实，近期大量倒闭，必须进行有效及时的整顿，正本清源，是非常必要的。但中国消费信贷的主要业务在房贷及车贷。在美国还包括信用卡及学生贷款。网贷极大部份都是小额贷款，况且未及时偿还前期的贷款利息和本金，就会立刻影响其再贷款，所以风险有限。相信极大部份网贷公司的倒闭，是其经营成本太高，入不敷出，连年亏损，而不是贷款呆账所至。有人更以单个事例，因为网贷而提前消费，导致个人大的负担，影响日常生活，从而指责网贷，一棍子打死一大片，颇有不公之处。正是有民众所指，玩游戏沉迷，严重影响学习 , 生活和工作，为什么不指责、处罚游戏开发商？许多银行，包括大的国有银行，锦上添花，诱使众多成功的企业，接受其颇有吸引力的贷款，从而导致这些企业盲目扩张，无节制的投资，最终破产，为什么不指责、处理这样的银行？

中国革命和建设的最重大的经验和教训，就是要坚持实事求是，既要注意防右，更要特别注意反左。中国改革开放四十多年所取得的史无前例的成就，是坚持这一基本思想和原则的伟大胜利。“右倾主义”动摇人民的信仰，篡改中国道路，危害中国

革命和建设，但“左倾思想”更具欺骗性，煽动性，从而更具危险性，这些是已有历史定论的 , 人们绝对不能忘记。实事求是就要客观公正全面地审视人和事，特别是对新生事物，要用开放的心态，思维和思想去作分析和判断。实事求是就要以事实为依据，了解掌握全面的事实而不是以偏概全，同时注意事实的历史性，时效性 ; 不能以新政策新法规去判断或衡量过去的各种情况或问题。

明事理方能思良策。记往昔峥嵘岁月，艰难困苦，吸取经验和教训，才能更好更快地发展。世界的多样性和复杂性，未来的不确定性和高风险性，带给人类巨大的挑战。而所有这些又是公平的，人类所共同面临的。胜利属于勇敢，有智慧并善于学习不断提高，勇于承认并及时改正错误，并能积极大胆尝试、创新的人们。历史是人民大众创造的，路是人走出来的。相信世界的明天是灿烂的 , 中国的未来是美好的 , 中国的金融业也会在更好更全面服务经济中稳定健康发展。

参考文献

Chen Yueyun, *et al*. The Relationship of the Manufacturing Growth with the Financial Industry and Real Estate Industry. *Journal of Business and Economic Policy*. Vol. 6, No. 2; June, 2019.

Chen Yueyun, *et al*. The Business Cycle and Economic Crisis—When Will China Experience Them? *Journal of Advances in Economics and Finance*. Volume 4, Number 2, May 2019.

陈岳云 , “中国民营企业要敢担当争创世界一流的跨国企业 ,”《人民论坛》, 12 月 (上), 2018。

陈岳云 ,“ 中国下一步怎么走 ?”, 《人民论坛》， 十一月 , 2017。

Chen Yueyun, *et al*. The Productivity, Economic Structure and Middle-Income Trap—Can China Avoid this Trap? *Journal of Applied Business and Economics*. Volume 19 (11), 2017.

ACADEMIC PERSPECTIVES
学术展望

自然科学
NATURAL SCIENCES

The Potential Role of Acupuncture Induced Nitric Oxide Release in Treatment of SARS-CoV 19

Sheng-Xing Ma

Lundquist Institute for Biomedical Innovation at Harbor-University of California at Los Angeles (UCLA) Medical Center and Department of Obstetrics and Gynecology, David Geffen School of Medicine at UCLA and Harbor-UCLA Medical Center, Torrance, CA 90502

ABSTRACT

The ongoing outbreak of COVID-19 has quickly become a daunting challenge to global health. In the absence of satisfied therapy, effective treatment interventions are urgently needed. Previous studies have demonstrated that acupuncture is effectively relieving common symptoms of COVID-19 including breathlessness, nausea, insomnia, leukopenia, fatigue, vomiting, and abdominal pain. Experiments have shown that nitric oxide (NO) inhibits the replication cycle of severe acute respiratory syndrome (SARS) coronavirus with similar structures of COVID-19. NO gas inhalation to increase the level of NO results in restoring lung function by reducing airway resistance and improving virus-induced lung infections in SARS patients. Recent case report showed that a medical acupuncturist with symptoms likely consistent with severe COVID pneumonia was full recovery by self-administered medical acupuncture and cupping therapy at home. Clinical features and pathophysiology demonstrated that NO deficiency and endothelial dysfunction contribute to the development of COVID-19. Several studies from different groups consistently demonstrated that acupuncture increase NO synthase

Corresponding author: Sheng-Xing Ma, Ph.D., Professor, Lundquist Institute for Biomedical Innovation at Harbor-Harbor-UCLA Medical Center, 1124 W. Carson Street, E6-room 219, Torrance, CA 90502, USA. Tel: (310) 974-9573; E-mail: sxma@lundquist.org.

expression and induce an elevation of NO production and release in plasma and the local skin regions in both animals and humans. It is suggested that exogenous NO supplies or interventions to induce NO can play an important role in protective effects against inflammation and acute lung injury for patients during this pandemic. This article reviews the rationale for mechanisms of NO induction induced by acupuncture in the possible treatment of COVID-19 and highlights its potential for contributing to better clinical outcomes and improving future clinical studies of acupuncture on treatment of COVID-19.

Keyword: COVID-19, SARS, nitric oxide, acupuncture, endothelial dysfunction, inflammation, mechanisms

INTRODUCTION

The ongoing outbreak of COVID-19, known as severe acute respiratory syndrome coronavirus 2 (SARS-CoV-2) (2019), has quickly become a daunting challenge to global health. The COVID-19 epidemic is spreading all over the world with a 6.9% mortality rate, but there is no targeted treatment satisfied and confirmed by well-designed clinical trials [1, 2]. Supportive treatment is currently being employed for the most common symptoms being fever, chills, shortness of breath, myalgia, headache, anosmia, dysgeusia, cough, and sore throat [3, 4]. China has reported that, as of February 17, 2020, about 85% of confirmed COVID-19 patients have been treated with TCM [5, 6]. In response to a call by the Chinese government to employ Traditional Chinese Medicine (TCM) to help with prevention, treatment, and rehabilitation, the China Association of Acupuncture-Moxibustion developed guidance for acupuncture and moxibustion intervention on COVID-19 [6, 7]. This guidance included advice on how to self-administer acupuncture and moxibustion under the direction of a physician in the various stages of disease process and recovery [7].

Acupuncture and electroacupuncture (EA) have long been used in Asia for various types of pain relief including pain and treat respiratory diseases, and are increasing in popularity in the West [8-11]. Previous randomized controlled trial reported that acupuncture is an effective therapeutic approach for chronic obstructive pulmonary disease (COPD) associated breathlessness [12]. The recent systematic review and meta-analysis show that acupuncture can relieve breathlessness in subjects with advanced diseases supported by a number of randomized controlled trials [13-15]. Previous clinical studies have also demonstrated

that acupuncture is effectively relieving common symptoms including nausea, insomnia, leukopenia, fatigue, vomiting, abdominal pain, abdominal distension, and anxiety disorders [16-22]. It is believed that some symptoms of COVID-19, breathlessness, insomnia, leucopenia, fatigue, nausea and vomiting, abdominal pain and abdominal distension as well as anxiety, may be improved by acupuncture treatment [15]. Recently, a case report indicated a patient as a frontline anesthesiologist and medical acupuncturist with pulmonary symptoms likely consistent with severe COVID pneumonia who was full recovery by self-administered medical acupuncture and cupping therapy at home [23]. Acupuncture may play a role in the treatment and rehabilitation of the COVID-19, and relieve the symptoms caused by COVID-19. However, there is no well-designed clinical trial to elucidate the effectiveness and safety of acupuncture with high-quality evidence in the treatment of COVID-19. Relevant studies have recently proved that acupuncture improves multiple symptoms involved in COVID-19 and has a case reporting the therapeutic effects, therefore, it is urgent to introduce novel research ideas into the research of the potential mechanisms of acupuncture for treatment of COVID-19 [11]. In this review, the evidence and understanding of the role of nitric oxide (NO) in the pathophysiology of new coronary pneumonia have been summarized with an emphasis on recent development of endothelial dysfunction and NO deficiency in the development of COVID-19. Acupuncture and related stimuli-induced NO production and release have been aimed to reveal the possible mechanisms of acupuncture against SARS/COVID-19 through the effects of NO on inhibition of coronavirus, improvements of inflammation and a cytokine storm. The increased interest in the NO on COVID-19 development and treatment has led to an open-minded attitude towards understanding this system, which is fundamental important to establish the valid aspects of scientific basis of the mechanisms and therapeutic effects of acupuncture on treatment of COVID-19.

THE ROLE OF NITRIC OXIDE (NO) IN THE PATHOPHYSIOLOGY OF COVID-19

NO deficiency and endothelial dysfunction in the development of COVID-19

It is well-documented that NO is one of the most important messenger molecules, and NO stimulates guanylyl cyclase to generate cGMP, a second messenger directing vasodilatation [24]. Intrinsic vasodilator action of NO-cGMP is critical important in microvascular endothelial dysfunction (MEF) and serves as a surrogate index of MEF [25-27]. Endothelial dysfunction (ED) contributed to various cardiovascular disorders including

essential hypertension, coronary artery disease, and thrombus formation [27-29].

A recent review (Martel *et al*., 2020) on strategies suggested to increase airway nitric oxide for treatment and possibly prevention of Covid-19 [30]. The clinical presentation of Covid-19 begins with acute respiratory distress in the lungs that moves quickly to vascular networks throughout the gut, kidney, heart, brain and skin with associated ED and abnormally rapid life-threatening blood clotting [2, 30, 31]. It is believed that Covid-19 is emerging as a thrombotic and vascular disease targeting endothelial cells throughout the body and is particularly evident in patients with cardiometabolic comorbidities associated with ED [30, 32]. Since the endothelium releases NO as the vasodilator and antithrombotic factor, nitric oxide whereas in injured vessels, NO is impaired contributing to hypertension and thrombus formation [31]. A hallmark of MED and thrombotic events is suppressed endothelial nitric oxide synthase (eNOS) with concomitant nitric oxide deficiency. It is suggested that restoring nitric oxide, independent of eNOS, may counter endothelitis and contribute to pulmonary vasodilation, antithrombotic, and direct antiviral activity [30, 32]. Moreover, NO has been demonstrated to interfere with the interaction between coronavirus viral S-protein and its cognate host receptor, ACE-2 while NO-mediated S-nitrosylation of viral cysteine proteases and host serine protease, TMPRSS2, which are both critical in viral cellular entry, appear to be NO sensitive [33-36].

The therapeutic effects of nitric oxide (NO) on SARS-CoV 19

Previous experiments have shown that NO inhibits the replication cycle of severe acute respiratory syndrome (SARS) coronavirus [37]. NO also inhibits the virus by reducing the production of viral RNA and reducing the expression of thioprotein and its binding receptor Angiotensin Converting Enzyme 2 [38]. The thioprotein binds to Angiotensin Converting Enzyme 2, which is also the pathogenic target receptor of the 2019 new coronavirus [2]. A trial analysis of a coronavirus extracted from SARS clinical patients published in The Lancet in 2003 showed that glycyrrhizin extracted from licorice root produces NO release effect, thereby inhibiting the replication of SARS virus [39]. In a small clinical study in Beijing during the SARS prevention and treatment period in 2004, inhaling NO gas in 6 patients not only reduced airway resistance, increased arterial oxygen partial pressure and oxygen saturation, but also took a chest radiograph after stopping NO gas inhalation [40]. Interestedly, after stopping NO gas inhalation the density and range of lung infiltration and physiological functions continued to be improved. Obviously, NO gas not only reduces airway resistance and improves lung function, but it also has obvious benefits for virus-induced lung infections [40]. The 2019-nCoV and SARS-CoV belong to different subtypes

of coronaviruses and have similar structures [2]. Clinical evidence shows that NO gas inhalation to increase the level of NO which results in restoring lung function by reducing airway resistance and improving virus-induced lung infections. Clinical features, pathology and homology suggest that uncontrolled inflammation and a cytokine storm likely drive COVID-19's unrelenting disease process [2, 30]. Interventions that are protective against inflammation, cytokine storm, and acute lung injury can play a critical role for patients and health systems during this pandemic. NO is an antimicrobial and anti-inflammatory molecule with key roles in pulmonary vascular function in the context of viral infections and other pulmonary disease states. Increased evidence supports the rationale for exogenous NO supplements and interventions to increase endogenous NO synthesis/release against the pathogenesis of COVID-19, which is potential for contributing to better clinical outcomes and healthcare capacity.

ACUPUNCTURE INDUCED NITRIC OXIDE PRODUCTION AND RELEASE

Acupuncture induces nNOS expression and NO release in acupuncture points (acupoints) and the brain of rats

Our previous studies demonstrated that neuronal NO synthase (nNOS) expression is increased in the dorsal medulla, the gracile nucleus and nucleus tractus solitarius (NTS), by electroacupuncture (EA) stimulation of ST36 (Zusanli) in rats [41]. EA ST36, an acupoint on the leg, induced nNOS-NO generation in the dorsal medulla causes a decrease in arterial blood pressure [42]. Withdrawal latencies to mechanical and noxious heat stimuli are reduced in Zucker Diabetic Fatty (ZDF) neuropathic rats and improved by EA ST36 in the rats associated with increased NO release in the gracile nucleus [43]. EA ST36-induced alleviation of pain/mechanical hypersensitivities in ZDF neuropathic rats are potentiated by an NO donor and inhibited by a selective inhibitor of neuronal NO synthesis infused into the gracile nucleus. Consistent with the postulated role of the dorsal column pathway in nociceptive regulation, our results show that expressions of transient receptor potential vanilloid type-1 (TRPV1) endowed with nNOS are predominantly increased in the gracile nucleus and in local acupoints following EA ST36 in rats [44, 45]. Other study reported that EA stimulation increases the circulating concentration of endothelial NO synthase in rats with hypoxia-induced pulmonary hypertension [46]. Consistently, EA stimulation of acupoint ST36 induced antinociception are blocked by both inhibitors of NO synthase and guanylyl cyclase, which suggest that NO-cGMP pathway mediates orofacial antinociception induced by EA ST36 [47]. Intraperitoneal administration of specific inhibitors of nNOS, inducible

NO synthase and a ATP-sensitive K+ channels blocker reversed the antinociception induced by EA. The results suggest that NO participates of antinociceptive effect of EA through nNOS, iNOS and ATP-sensitive K+ channels activation [48].

Double immunostaining of transient receptor potential vanilloid type-1 (TRPV1) receptor and nNOS revealed co-localization of TRPV1 and nNOS in both subepidermal nerve fibers and in dermal connective tissue cells [45]. A high expression of TRPV1 endowed with nNOS in subepidermal nerve fibers exist in the acupoints and the expression is increased by EA [44, 45]. The results suggest that the higher expression of TRPV1 in the subepidermal nerve fibers and its upregulation after EA stimulation may play a key role in mediating the transduction of EA signals to the CNS, and its expression in the subepidermal connective tissue cells may play a role in conducting the local effect of the EA. Other studies have shown that either manual acupuncture or EA at the ST36 acupoint significantly increased components of the TRPV1-related signaling pathway in mice [49], and modified acupuncture-induced reflex excitatory cardiovascular responses in humans [50]. The results suggest that the TRPV1 signaling pathway is highly correlated to acupuncture effects and EA-induced expression of TRPV1-nNOS in the ST36 and the NTS/gracile nucleus is involved in the signal transduction of EA stimuli via somatosensory afferents-brain pathways [45, 46, 51].

Acupuncture induces NO release in humans

We have demonstrated, using dermal microdialysis in human subjects, that dialysate NO-cGMP releases in the subcutaneous tissue of the forearm skin along the PC acupoints are increased by EA stimulation [52]. The results are consistent with the results reported that transcutaneous electrical nerve stimulation (TENS) induces an elevation of NO and cGMP release biocaptured over PC acupoints in humans [53]. Recently, the effects of reinforcing method using manual acupuncture (MA) vs. reductive EA on local NO release have been examined using the novel biocapture device over skin regions in humans [54]. Results show that NO levels biocaptured over the skin regions are increased following MA by twisting/rotating the needle with gentle amplitude and moderate speed. In contrast, NO levels over the areas of the skin regions are moderately reduced by high-frequency EA (30 Hz), a reduction method. The laser acupuncture (LA) also induces NO release at acupoints with the more level at contralateral side than stimulating site measured by dialysis tube taped to the areas [55]. Kimura, *et al*. reported that acupuncture induces cutaneous vasodilatation in the forearms of humans, which is attenuated by application of NO synthesis inhibitor [56]. It is postulated that acupuncture stimulation improves local circulation and allows for a flush

of algesic or sensitizing substances, leading to pain relief, thus NO release mediates local effects of acupuncture as therapeutic mechanisms of acupuncture analgesia [57-59].

These results suggest that MA, EA, LA, and TENS consistently demonstrated an elevation of NO release. It is well-documented that NO improves circulation and microvascular endothelial function, which contribute to various cardiovascular disorders, thrombus formation [27-29], anti-inflammation, and pain relief [57-59].

CONCLUSION

The COVID-19 epidemic is spreading all over the world, and the etiological agent of COVID-19 has been confirmed as SARS-CoV-2. The effective treatment interventions are urgently needed since there is no satisfied treatment at the time of this writing. Many studies have been conducted on Chinese herbal remedies with protocols published for various stages of the COVID-19 disease, but acupuncture studies with regard to COVID-19 are sparse. Acupuncture therapy is relatively easy to practice with minimal risks to the patients but the potential mechanisms of acupuncture for the treatment of COVID-19 are unknown. NO is an antimicrobial and anti-inflammatory molecule with key roles in pulmonary vascular function in the context of viral infections. Previous studies have demonstrated that NO inhibits the replication cycle of SARS coronavirus, and NO gas inhalation to increase the level of NO results in restoring lung function by reducing airway resistance and improving virus-induced lung infections in SARS patients. Recent studies have suggested that NO deficiency and ED contribute to the development of COVID-19. Acupuncture is effectively relieving common symptoms of COVID-19 including breathlessness, nausea, insomnia, leukopenia, fatigue, vomiting, and abdominal pain. Several studies from independent groups consistently demonstrated that MA, EA, LA, and TENS induce local NO-cGMP release in humans. MA and EA also increase NO synthase expression and induces an elevation of NO production in plasma and over local skin regions in both animals and humans. Moreover, it has been suggested that exogenous NO supplies or interventions to elevate NO production may have protective effects against inflammation and acute lung injury for COVID-19 patients and health systems during this pandemic. Whether the therapeutic effects of acupuncture for treatment and prevention of COVID-19 require further investigation by well-designed clinical trials in order to further understand the therapeutic nature of therapy on COVID-19. The possible mechanisms of NO induction induced by acupuncture should contribute to better clinical outcomes and facilitating clinical studies of acupuncture on treatment and prevention of COVID-19.

REFERENCES

1. COVID-19 Dashboard by the Center for Systems Science and Engineering (CSSE) at Johns Hopkins University (JHU). ArcGIS. Johns Hopkins University. Online document at: https://gisanddata.maps.arcgis.com/apps/opsdashboard/index.html#/bda7594740fd40299423467b48e9ecf6 Accessed May 11, 2020.
2. Wadman M., Couzin-Frankel J., Kaiser J., Matacic C. How does coronavirus kill? Clinicians trace a ferocious rampage through the body, from brain to toes. Science. April 17 2020 doi: 10.1126/science.abc3208.
3. Ahn DG, Shin HJ, Kim MH, *et al*. Current status of epidemiology, diagnosis, therapeutics, and vaccines for novel coronavirus disease 2019 (COVID-19). J Microbiol Biotechnol. 2020; 30:313–24.
4. Wu L, Dong Y, Li J, *et al*. The effect of massage on the quality of life in patients recovering from COVID-19: a systematic review protocol. Medicine (Madr). 2020;99:e20529.
5. Yang Y, Islam MS, Wang J, Li Y, Chen X. Traditional Chinese medicine in the treatment of patients infected with 2019-new coronavirus (SARS-CoV-2): A review and perspective. Int J Biol Sci. 2020; 16:1708–1717.
6. Ho LT, Chan KK, Chung VC, Leung TH. Highlights of traditional Chinese medicine frontline expert advice in the China national guideline for COVID-19. Eur J Integr Med. 2020; 36: 101116.
7. Liu W-H, Guo S-N, Wang F, Hao Y. Understanding of guidance for acupuncture and moxibustion interventions on COVID-19 (Second edition) issued by CAAM. World J Acupunct Moxibustion. 2020; 30:1–4.
8. Manheimer E, White A, Berman B, Forys K, Ernst E: Meta-analysis: acupuncture for low back pain. Ann Intern Med. 2005; 142:651-663.
9. Vickers AJ, Cronin AM, Maschino AC, Lewith G, MacPherson H, Foster NE, Sherman KJ, Witt CM, Linde K, Acupuncture Trialists' Collaboration: Acupuncture for chronic pain: individual patient data meta-analysis. Arch Intern Med. 2012; 172:1444-1453.
10. Kaptchuk TJ. Acupuncture: theory, efficacy, and practice. Ann Intern Med. 2002; 136:374–83.
11. Han ZZ, Zhang Y, Wang PQ, Tang QL, Zhang K: Is acupuncture effective in the treatment of COVID-19 related symptoms? Briefings in Bioinformatics. 2021, doi: 10.1093/bib/bbab110
12. Coyle ME, Shergis JL, Huang ET, *et al*. Acupuncture therapies for chronic obstructive

pulmonary disease: a systematic review of randomized, controlled trials. Altern Ther Health Med. 2014; :10–23.

13. Vn Trott P, Oei SL, Ramsenthaler C. Acupuncture for breathlessness in advanced diseases: a systematic review and meta-analysis. J Pain Symptom Manage. 2020;59:327.e3–38.e3.
14. Zhang K, Li Y, Tang Q. Acupuncture for breathlessness in advanced diseases: methodological issues. J Pain Symptom Manage. 2020;59:e3–4.
15. Zhang B, Zhang K, Tang Q, *et al*. Acupuncture for breathlessness in COVID-19: a protocol for systematic review and meta-analysis. Medicine (Madr). 2020;99:e20701.
16. Cheong KB, Zhang JP, Huang Y, *et al*. The effectiveness of acupuncture in prevention and treatment of postoperative nausea and vomiting–a systematic review and meta-analysis. PLoS One. 2013;8:e82474.
17. Zhang Y, Lin L, Li H, *et al*. Effects of acupuncture on cancer-related fatigue: a meta-analysis. Support Care Cancer. 2018; 26:415–25.
18. Bacaro V, Benz F, Pappaccogli A, *et al*. Interventions for sleep problems during pregnancy: a systematic review. Sleep Med Rev. 2020; 50:101234.
19. Lee SH, Lim SM. Acupuncture for insomnia after stroke: a systematic review and meta-analysis. BMC Complement Altern Med. 2016; 16:228.
20. Zhang K, Gao C, Li C, *et al*. Acupuncture for acute pancreatitis: a systematic review and meta-analysis. Pancreas. 2019; 48:1136–47.
21. Zhang K, Li C, Gao C, *et al*. Efficacy and safety of acupuncture as an adjuvant treatment for acute pancreatitis: a protocol of systematic review and meta-analysis. BMJ Open. 2019;9:e029327.
22. Amorim D, Amado J, Brito I, *et al*. Acupuncture and electroacupuncture for anxiety disorders: a systematic review of the clinical research. Complement Ther Clin Pract. 2018; 31:31–7.
23. Cheng SI: COVID-19-related respiratory distress: Personal experience from a frontline Anesthesiologist. Medical Acupuncture. 2021:33 https://doi.org/ 10.1089/acu.2020.1467
24. Denninger JW, Marletta MA: Guanylate cyclase and the NO/cGMP signaling pathway. Bioch Biophy Acta. 1999; 1411:334-350.
25. Tousoulis D., Kampoli A.-M., Tentolouris C., Papageorgiou N., Stefanadis C. The role of nitric oxide on endothelial function. Curr Vasc Pharmacol. 2012; 10:4–18.
26. Green S.J. Nitric oxide in mucosal immunity. Nat Med. 1995; 1:515–517.
27. Quyyumi A: Endothelial function in health and disease: New insights into the genesis

of cardiovascular disease. Am J Med. 1998; 105:32-39.

28. Lind L, Granstam SO, Millgard J: Endothelium-dependent vasodilation in hypertension: A review. Blood Pressure. 2000; 9:4-15.
29. Cai H, Harrison DG: Endothelial dysfunction in cardiovascular diseases: The role of the oxidant stress. Circ Res. 2000; 87:840-4.
30. Martel J., Ko Y.-F., Young J.D., Ojcius D.M. Could nitric oxide help to prevent or treat COVID-19? Microb Infect. 2020 doi: 10.1016/j.micinf.2020.05.002.
31. Green SJ: Covid-19 accelerates endothelial dysfunction and nitric oxide deficiency. Microbes Infect. 2020; 22: 149–150.
32. Varga A., Flammer A.J., Steiger P., Haberecker M., Andermatt R., Zinkernagel A.S. Endothelial cell infection and endotheliitis in Covid-19. Lancet. 2020; 395:1417–1418.
33. Akerstrom S., Gunalan V., Keng C.T., Tan Y.-J., Mirazimi A. Dual effect of nitric oxide on SARS-CoV replication: viral RNA production and palmitoylation of the S protein are affected. Virology. 2009; 395:1–9.
34. Hoffman M., Kleine-Weber H., Schroder S., Kruger N., Herrler T., Erichsen S. SARS-CoV-2 Cell entry depends on ACE2 and TMPRSS2 and is blocked by a clinically proven protease inhibitor. Cell. 2020; 181:271–280.
35. Arora H., Panara K., Kuchakulla M., Kulandavelu S., Burstein K.L., Schally A. Alterations of tumor microenvironment by nitric oxide impedes castration-resistant prostate cancer growth. Proc Natl Acad Sci USA. 2018; 115:11298–11303.
36. Shulla A., Heald-Sargent T., Subramanya G., Zhao J., Perlman S., Gallagher T.A. A transmembrane serine protease is linked to the severe acute respiratory syndrome coronavirus receptor and activates virus entry. J Virol. 2011; 85:873–882.
37. Akerström S, Mousavi-Jazi M, Klingström J, Leijon M, Lundkvist A, Mirazimi A: Nitric oxide inhibits the replication cycle of severe acute respiratory syndrome coronavirus. J Virol. 2005; 79:1966-1969.
38. Akerström S, Gunalan V, Keng CT, Tan YJ, Mirazimi A: Dual effect of nitric oxide on SARS-CoV replication: viral RNA production and palmitoylation of the S protein are affected. Virology. 2009; 395:1-9.
39. Cinatl J, Morgenstern B, Bauer G, Chandra P, Rabenau H, Doerr HW: Glycyrrhizin, an Active Component of Liquorice Roots, and Replication of SARS-associated Coronavirus. Lancet. 2003; 361:2045-2046.
40. Chen L, Liu P, Gao H, Sun B, Chao D, Wang F, Zhu Y, Hedenstierna G, Wang CG: Inhalation of nitric oxide in the treatment of severe acute respiratory syndrome: a rescue trial in Beijing. Clin Infect Dis. 2004;39:1531-1535.

41. Ma SX, Ma J, Moise G, Li XY: Responses of Neuronal Nitric Oxide Synthase Expression in the Brainstem to Electroacupuncture Zusanli (ST 36) in Rats. Brain Res. 2005; 10:70-77.
42. Chen S, Ma SX: Nitric oxide on acupuncture (ST36)-induced depressor response in the gracile nucleus. J Neurophysiol. 2003; 90:780-785.
43. Rong, PJ, Ma SX: Electroacupuncture Zusanli (ST36) on release of nitric oxide in the gracile nucleus and improvement of sensory neuropathies in Zucker Diabetic Fatty rats. Evid Based Complement Alternat Med. 2009; Advance Access published on August 13, 2009. doi:10.1093/ecam/nep103.
44. Ji B, Hu J, Ma SX: Effects of electroacupuncture Zusanli (ST36) on food intake and expression of POMC and TRPV1 through afferents-medulla pathway in Obese Prone Rats. Peptides. 2013; 39:188-194.
45. Ibrahim TS, Chen ML, Ma SX. TRPV1 expression in acupuncture points: Response to electroacupuncture stimulation. J Chem Neuroanat. 2011; 41:129-136.
46. Pan P, Zhang X, Qian H, Shi W, Wang J, Bo Y, Li W: Effects of electro-acupuncture on endothelium-derived endothelin-1 and endothelial nitric oxide synthase of rats with hypoxia-induced pulmonary hypertension. Exp Biol Med (Maywood). 2010; 235:642-648. doi: 10.1258/ebm.2010.009353.
47. Almeida RT, Duarte ID: Nitric oxide/cGMP pathway mediates orofacial antinociception induced by electroacupuncture at the St36 acupoint. Brain Res. 2008 Jan 10;1188:54-60. doi: 10.1016/j.brainres.2007.10.060. Epub 2007 Nov 1.
48. Almeida RT, Galdino G, Perez AC, Silva G, Romero TR, Duarte ID: St36 electroacupuncture activates nNOS, iNOS and ATP-sensitive potassium channels to promote orofacial antinociception in rats. J Physiol Pharmacol. 2017;68:27-33.
49. Chen HC, Chen MY, Hsieh CL, *et al*. TRPV1 is a responding channel for acupuncture manipulation in mice peripheral and central nerve system. Cell Physiol Biochem. 2018, 49:1813-1824.
50. Guo ZL, Fu LW, Su HF, *et al*: Role of TRPV1 in acupuncture modulation of reflex excitatory cardiovascular responses. Am J Physiol Regul Integr Comp Physiol. 2018; 314:R655-R666.
51. Ma SX: Neurobiology of acupuncture: Toward CAM. Evid Based Complement Alternat Med. 2004; 1:41-47.
52. Lim N, Ma SX: Responses of nitric oxide-cGMP releases in acupuncture point to electroacupuncture in human skin *in vivo* using dermal microdialysis. Microcirculation. 2009; 16:434-443.

53. Ma SX, Mayer E, Lee P, Li XY, Gao EZ. Transcutaneous electrical nerve stimulation increased nitric oxide-cyclic cGMP release biocaptured over skin surface of the pericardium meridian and acupuncture points in humans. Acup & Electro-Therapeutics Res INT J. 2015; 40:73-86.

54. Ma SX, Lee P, Anderson TL, Li XY, Jiang I. Response of local nitric oxide release to manual acupuncture and electrical heat in humans: Effects of reinforcement methods. Evid Based Complement Alternat Med. 2017; 2017:1-8.

55. Jiang WL, Wei HJ, Guo ZY, Ni YR, Yang HQ, Xie SS: Changes in nitric oxide releases of the contralateral acupoint during and after laser acupuncture at bilateral same-name acupoints in human. Evid Based Complement Alternat Med. 2017;2017:5763458.

56. Kimura K, Takeuchi H, Yuri K, Wakayama I. Effects of nitric oxide synthase inhibition on cutaneous vasodilation in response to acupuncture stimulation in humans. Acupunct Med. 2013; 31:74-80.

57. Sandberg M, Lundeberg T, Lindberg LG, Gerdle B. Effects of acupuncture on skin and muscle blood flow in healthy subjects. Eur J Appl Physiol. 2003; 90:114-119.

58. Sandberg M, Lindberg LG, Gerdle B. Peripheral effects of needle stimulation (acupuncture) on skin and muscle blood flow in fibromyalgia. Eur J Pain. 2004; 8:163-71.

59. Sandberg M, Larsson B, Lindberg LG, Gerdle B. Different patterns of blood flow response in the trapezius muscle following needle stimulation (acupuncture) between healthy subjects and patients with fibromyalgia and work-related trapezius myalgia. Eur J Pain. 2005; 9:497-510.

Explore the quantum effects on reversible loss of consciousness in the brain

Gary G. Fan, MD

White Memorial Medical Center, Los Angeles, California 90033, USA

ABSTRACT

One of the most important open questions in science is how our consciousness is established. The definitive explanation of consciousness is still unconfirmed. The recent rise of quantum biology as an emerging field at the border between quantum physics and the life sciences suggests that quantum events have been implicated in photosynthesis, avian migration and olfaction, and quantum effects could play a non-trivial role in the neural processing in brain. Most recent studies proposed that general anesthetic, which switches off consciousness, does this through quantum means. This review aims to focus on some consciousness hypotheses derived from quantum mechanics and the framework of the quantum effects on neural processing for consciousness formation and origin by the convincing experimental evidence.

Keyword: Quantum effect, consciousness formation, microtubule, Posner molecule, Lithium, Xenon, brain

Corresponding author: Gary G Fan, MD., White Memorial Medical Center, Los Angeles, California 90033, USA/1720 East Cesar E Chavez Avenue, Los Angeles, CA 90033, USA. Tel: (626)-898-3196; E-mail: garyfan1161@gmail.com.

INTRODUCTION

In the twentieth century, medical research was mainly carried out at physics, chemistry, molecular biology and genetics level, which led the way for medicine to move to deeper level in 21st century. In fact, the knowledge about human body, especially the brain, we have learned is still superficial in the sense of so much mystery to be unveiled. What is the origin of consciousness and cognition? How are they processed in the brain? These two issues have been challenging the medical researchers for past decades.

Quantum biology is a new discipline arising from recent research that suggests that biological phenomena such as photosynthesis, enzyme catalysis, avian navigation or olfaction may not only operate within the bounds of classical physics but also make use of the several non-trivial features of quantum mechanics, such as coherence, tunnelling, entanglement and superposition. One of the most celebrated examples is the claimed long-lived quantum coherence observed in the transport of exciton energy in photosynthesis [1]. A more established role for quantum mechanics is found in the tunnelling of electrons and protons in enzyme catalysis [2]. Beyond these examples of quantum biology, quantum entanglement has been implicated in avian navigation [3], while quantum tunnelling has been proposed to be involved in olfaction [4, 5] and gene mutation [6]. The newest significant findings from research have expanded the role of quantum biology to more complex systems in which quantum dynamics might be enhanced by a finely tuned and constructive interplay between the quantum system and its surroundings, which makes the roots of quantum biology go much deeper. For instance, the studies in quantum neuroscience have gained impressive insights from the brain studies at atomic/subatomic or quantum level.

Quantum physics started in the early twentieth century and deals with the behavior of matter and light on the atomic and subatomic scale. It attempts to describe and account for the properties of molecules, atoms and their constituents — electrons, protons, neutrons, and other more esoteric particles such as quarks and gluons. These properties include the interactions of the particles with one another and with electromagnetic radiation.

POSSIBILITY OF QUANTUM EFFECTS IN THE BRAIN

All these fundamental particles that make up matter including living things have strange dynamic behaviors, different what we expect at macroscopic level. In the world of quantum particles, classical laws of physics are no longer applicable. The elementary particles have unique elusive eigenstates, which set up barriers for us to uncover the mystery of the brain.

Studies in quantum biology pave the way for the exploration of quantum effects on the brain. There is a theory that our brain can determine more definite superpositions for particles and that is what grants us our consciousness. The second interesting idea is based upon the quantum entanglement, which is established on the relationships and dependency that particles have with one another.

The emergence and loss of consciousness can happen in an instant under different conditions. The permanent loss of consciousness can be seen in a patient that is in a persistent vegetative state or death. The reversible loss of consciousness is the basis of anesthesia. It is a prerequisite for a patient to receive surgical treatment. The patient's consciousness temporarily lost when the patient received surgical treatment. Although we have gained a better understanding for the mechanism of anesthesia induction at cellular and molecular level in the brain. We still have a difficult time characterizing what we understand the process and origin of consciousness. According to most recent study [7], the general anesthesia, which switches off consciousness, could be initiated by quantum processing, measured by changes in electron spin.

In order to understand the quantum activity in the brain, let's review some facts. The element composition of the human body is mainly composed of oxygen (65%), carbon (18.5%), hydrogen (9.5%), nitrogen (3.2%), calcium (1.5%), and phosphorus (1%). There is also a small amount of other trace elements that play a role in the regulation of cellular function, information processing and signal transduction. Among those elements, hydrogen, oxygen, phosphorus, and calcium are more important in quantum neuroscience. The nuclear spin of hydrogen and phosphorus atom is at half-integer spin I=1/2. Calcium phosphate ($Ca(H_2PO_4)_2$) is a biological molecule composed of phosphorus, oxygen and calcium ions. It has been suggested to be an important promoter of quantum entanglement within the brain.

An atom consists of a central nucleus that is surrounded by electron(s). The nucleus contains protons and neutrons. Both particles are composed of quarks, in which the difference lies in the orientation and momentum of quarks. Proton is composed of two upper quarks and one lower quark arrangement. In contrast to proton, neutron is composed of one lower quark and two upper quarks arrangements. We know that the nuclear spin is very sensitive to the electric field if its spin number is greater than the integer 1, and the quantum decoherence is very fast at milliseconds to seconds. For example, the third element lithium 7 (Li7) in the periodic table, its nuclear spin is I= 3/2, its decoherence time is only 10 seconds. While the nuclear spin is half an integer (I=1/2), it is only sensitive to the magnetic field, and the quantum decoherence time is very slow. By contrast, lithium element 6 (Li6), its nuclear spin is at I=1/2, the decoherence time can reach 5 minutes.

Let's also review several important concepts in quantum mechanics and dynamics. Quantum dynamics studies the motion and interaction of subatomic particles at the minimum energy level. First, 'quantum spin' is the intrinsic angular momentum. In quantum mechanics, angular momentum is discrete, quantized in units of Planck's constant divided by 4 Pi. Niels Bohr proposed that angular momentum is quantized in 1913 and used this to explain the line spectrum of hydrogen. Second, 'quantum coherence and decoherence' is the fundamental concept of quantum physics. Quantum coherence is the ability of a quantum system to demonstrate interference. It is shared with the environment and appears to be lost with time. Therefore, Quantum decoherence is the loss of quantum coherence, which means that the interference from the environment will cause the information in the coherent system to be lost and cause the wave function to collapse. Third, 'quantum entanglement' refers to a pair of coherent quanta, in which one of quanta is changed, the other one will be perceived with zero-time difference, no matter how far away the quantum is. This is what Einstein called the ghost effect. Fourth, the 'uncertainty' of the quantum means the more precise you want to determine the position of a quantum, the less you know of its precise dynamics, such as its angular momentum and speed. Fifth, the 'wave-particle duality' of quantum means that a quantum is both a particle and also has characteristics of a wave. For example, the photon passes through a gap and is projected onto the opposite reflector. You can see the diffraction wave formed by the photon. Sixth, the 'superposition' of quantum is the feature of a quantum system whereby it exists in several separate quantum states at the same time. Any two (or more) quantum states can be added together ("superposed") and the result will be another valid quantum state. Seventh, the 'quantum tunneling effect' means that quantum can pass through macroscopic potential energy barriers without resistance. The phenomenon sometimes exhibited by moving particles that succeed in passing from one side of a potential barrier to the other although of insufficient energy to pass over the top.

QUANTUM NEUTRON IN LITHIUM PLAYS A ROLE IN THE CHANGE OF COGNITION AND CONSCIOUSNESS

Dr. J. A. Sechzer *et al*. chose the third element lithium from the periodic table to design an interesting experiment [8]. Lithium has long been used to treat manic depression in the clinic. Its pharmacokinetics are relatively clear. It is safe for living organisms, but the mechanism of action has yet to be determined.

The researchers fed different lithium isotopes with altered neutrons to pre-impregnated and impregnated female rats, then observe the efficacy on maternal cognition, consciousness

and behavior in different groups. The steady-state lithium 7 (Li-7) that exists in nature is composed of three protons and four neutrons in the nucleus surrounding three electrons. A steady-state lithium 6 (Li-6) is an isotope of Li-7 which lost one neutron from the nucleus. Li 6 and Li 7 both have the same atomic weight since the mass of the lost neutron is negligible. Their chemical properties are still the same.

The experiments were carried out in three female rat groups before and after conception (Table 1): group 1 with Li 7, group 2 with Li 6 and group 3 without lithium. They were fed for 10 days before pregnancy and 20 days during pregnancy, because the gestation period of rats is generally 19 to 23 days. The mothers' mental and behavioral changes were recorded and analyzed during pregnancy and after delivery. The results are very interesting. In the first group rats fed with Li 7, the mothers are unwilling to make a nest for their newborns during pregnancy and after delivery. They are also unwilling to feed and care for the newborns after

Table 1. Lithium isotopes with altering neutrons could account for the results from the experiments in maternal rats

Groups fed with Female	**Pre-impregnated**	**Impregnated Rats**	**Efficacy on mothering behavior**
Lithium 7 (99%)	10 days	20 days	nest building: absent
Pharmacy Lithium (Li-7:92%)	10 days	20 days	nursing: infrequent/short duration grooming of pups: infrequent state of alertness: "low"
Lithium 6 (95%)	10 days	20 days	nest building: excessive, nursing: very frequent/long duration grooming/retrieval of pups: excessive state of alertness: "very high"
Control -no lithium	10 days	20 days	all: "average."

Nuclear spin processing might be operational in the brain: two lithium isotopes (Li-7 and Li-6) with altered the number of neutrons have the opposite effects on the cognition, consciousness and behavior in maternal rats.

delivery and appear lethargic. The results are quite different in the second group rats fed with Li 6. The mothers constantly made nests for newborns and strived for perfection during pregnancy and after delivery. They fed newborns in a state of excitement and care for them with full of energy all day long. In contrast to both lithium groups, the mothers in the control group without lithium built nest and took care of their newborns in a common way and behaved normally. These studies suggest that altering quantum neutron in the lithium nucleus can affect the rats' mental state, cognition, consciousness and behavior.

A reasonable assumption is that one neutron lost from the lithium nucleus changes the lithium nuclear spin. The Li 7 nuclear quantum spin number is I=3/2, which is greater than the integer 1. Its nuclear rotation is very sensitive to electric field, and the quantum decoherence time is very short. Whereas Li 6 nuclear spin number becomes half integer I=1/2, it is only sensitive to magnetic field. Its quantum decoherence time is greatly extended, which facilitates the quantum entanglement.

QUANTUM SPIN INVOLVES CONSCIOUSNESS SWITCHING

This theoretical hypothesis is supported by the following Xenon experiments, in which the process of consciousness formation may change with altering Xenon quantum spin state. Xenon, the element 54 in the periodic table, is an expensive rare gas and an important anesthetic. It can induce the human body to reversible state while losing consciousness. There are several stable isotopes of Xenon in nature. The difference between these isotopes is the number of neutrons in the nucleus, which determines the state of xenon nucleus quantum spin. However, the chemical properties of these stable xenon isotopes are still the same. It has been known that xenon (Xe129) and xenon (Xe131) have nuclear spin number at I= 1/2 and I=3/2, in contrast to xenon (Xe132) and xenon (Xe134) with nuclear spin number at zero.

N. Li *et al* measured the effect of the above four xenon isotopes on mice when inducing loss of consciousness with a loss righting reflex in their experiment, in order to determine if the xenon isotopes with different nuclear rotation change the mice's consciousness [9]. The experimental rats were divided into two groups. The rats in first group inhale Xe132 and Xe134 without nucleus rotation. The rats in second group inhale Xe129 (1/2) and Xe131 (3/2) with nucleus rotation. The results from rat's loss of righting reflex (ED50) showed that the rats inhaled xenon Xe132 and Xe134 easily lost consciousness. By contrast, the second group rats inhaled xenon Xe129 and Xe131 presented resistance to loss of consciousness. Their awake time was also prolonged. These results indicate that Xe129 and Xe131 with nuclear spins can slow down the self-induced loss of consciousness and keep or enhance the state

of consciousness. This conclusion was supported by another experiments. The researchers found that Xe129 and Xe131 with nuclear spins may slow down the loss of consciousness caused by isoflurane, a very potent general anesthetic. But Xe132 and Xe134 without nuclear rotation can rapidly promote isoflurane-induced loss of consciousness at low dose.

QUANTUM SUPERPOSITION INSIDE MICROTUBULE MAY INFLUENCE ORIGIN OF CONSCIOUSNESS

The next question is why the nuclear spin may change the formation processing of consciousness. Does the formation of consciousness occur at the synaptic junctions between neuronal cells, or in the organelles inside neurons in the brain?

Recent studies revealed that it is possible that primitive consciousness takes place in the microtubules of neurons in brain [10]. The neuron in brain is composed of three parts: Axon which stretches out like long slender branch and transmit information to different neurons and other tissues; Dendrites that are short branches extended from the neurons, along which impulses received from other cells at synapses are transmitted to the cell body; Cell body which contains nucleus and cytoplasm with organelles. The microtubule, a cellular cytoskeleton organelle, is composed of 13 α and β tubulins to form a tubular cylinder. Each tubulin contains 86 aromatic amino acids in which the benzene ring of each amino acid forms a Pi-resonance electron cloud, a dipole resonance state coming along. An ordered collective resonance is formed. The oscillation frequency occurs at terahertz (10^{12} Hz). This dipole resonance oscillation formed in the microtubules may be the basis for the initial formation of consciousness. The dipole electron cloud resonates synchronously, and the polarity is opposite orderly in the state of consciousness. When consciousness lost, the electron cloud resonance changes from synchronization to discrete, and the polarity disappears.

Dr. Hameroff, professor of anesthesia at Tucson University in the United States, and Dr. Sir Roger Penrose, professor of mathematics and quantum physics at the University of Cambridge in the United Kingdom, proposed the theory called “Orchestra Objective Reduction” [11]. The objective reduction is a quantum process and orchestrated by cellular structure- microtubules. The consciousness depends on biologically ‘orchestrated’ coherent quantum processes in collections of microtubules within brain neurons. The quantum superposition inside microtubule may influence the quantum state returning to the macroscopic state. Recorded EEG (Electroencephalography) could be the macroscopic results from the resonant wave superposition and regression.

According to the results from the previous experiments of xenon isotopes in rats and

the theory of "Orchestra Objective Reduction", it can be postulated that the anesthetics Xe129 and Xe131 with nuclear spin enters the neuronal microtubules in which they may block or hinder the Pi electron cloud formed from the resonance ring of aromatic amino acids during the process of loss of consciousness. The Xe132 and Xe134 without quantum nuclear rotation promotes the discrete resonance of the Pi electron cloud, destroys the order of the dipole, and accelerates the loss of consciousness. Above studies and hypothesis also correlates with the research done by Fisher *et al*. into a possible mechanism by which neural entanglement might proceed with consciousness formation [12].

'POSNER MOLECULE' PROTECTS NEURAL QUANTUM ENTANGLEMENT

Dr. Matthew Fisher, professor of quantum physics at University in California Santa Barbra, discovered that the Posner cluster molecule, which is ubiquitous in the human body, can provide an ideal place for quantum coherence and entanglement at body temperature. One of biggest challenges to quantum modeling of consciousness is phenomenon of decoherence. The environment of biological systems is not ideal because it is too hot, too wet and too noisy destroying any quantum effects before they could prove useful. Max Tegmark calculated the timescales on which decoherence occurs in the environment of the brain is considerably shorter than neural firing rates measured in milliseconds [13]. Dr. Fisher's study proposed that for quantum spins in Posner molecule, the coherence times could be as long as hours to days. Posner molecule consists of nine calcium ions and six phosphates to form a hexahedron. The entangled phosphate spins lead to the formation of entangled Posner molecules, in which the nuclear spin of the phosphorus atom is half-integer I=1/2, which greatly prolongs the quantum coherence time (1-10 days). Therefore, the entangled Posner molecule makes it possible to give rise to quantum effects on the neural processes in brain.

Phosphorus is bound into phosphate or polyphosphate ions such as pyrophosphate. Phosphate ions constitute part of the adenosine triphosphate (ATP) molecule, an organic chemical that acts as a source of energy for the many essential actions that sustain living organisms. Fisher postulates that when adenosine triphosphate is hydrolyzed to adenosine monophosphate and pyrophosphate the two phosphorus nuclei in the pyrophosphate ion will have a specific spin alignment, either a singlet or one of three triplet states [14]. A quantum mechanical treatment of the enzyme catalyzed reaction that creates two phosphate ions out of pyrophosphate demonstrates that this reaction depends on the nuclear spin state. More specifically, the conditional outcome of the enzyme reaction, where the spin dynamics of the triplet states are unfavorable, results in that the phosphorus nuclear spins in the two distinct

phosphate ions emerge in singlet entangled state.

ATP and guanosine triphosphate (GTP) both are energy-rich molecules. ATP is the energy carrier in the cell and widely involved in the phosphorylation and dephosphorylation of cellular molecules in the body. It not only provides energy for all biological activities but also releases entangled phosphorus into their downstream molecules during the processing. Without protection, a pair of entangled phosphorus may quickly become decoherent. When the entangled phosphate is protected by Posner molecules, the time of quantum entanglement is maintained and extended. If a pair of entangled phosphates are split into different Posner clusters, they can continue to maintain quantum entanglement. These entangled phosphates can even be transported to remote location in the body.

GTP has specific roles in many signaling pathways and provides energy for tubulin polymerization [15]. The entangled phosphates are distributed to tubulin dimers in the GTP-bound state. Subsequently, the tubulin bound GTP is hydrolyzed to GDP for polymerization [16]. The roles of these entangled phosphates in the microtubules for consciousness formation are yet to be identified.

SUMMARY

1. Consciousness may arise inside neurons, rather than the connections between neurons or the transmission of neurotransmitters at synapses.

2. Quantum spin, quantum entanglement and quantum superposition may participate in the occurrence of consciousness.

3. The Pi electron cloud resonance in the microtubules of the neurons may be the initial state of consciousness formation.

4. Posner molecules in the body can provide an optimized environment for quantum processing in the brain.

REFERENCES

1. Bi-Xue Wang, *et al*. Efficient quantum simulation of photosynthetic light harvesting. *NPJ Quantum Information*. 2018; 4: 52.
2. De Vault D. Quantum-mechanical tunneling in biological systems. *Cambridge, UK: Cambridge University Press*. 1984; vol. 2.
3. Hamish G, *et al*. The quantum needle of the avian magnetic compass. *PNAS*. 2016; 113 (17): 4634-4639.

4. Turin L. A spectroscopic mechanism for primary olfactory reception. *Chemical Senses.* 1996; 21: 773-791.
5. Liu S, *et al*. Exploring the mechanism of olfactory recognition in the initial stage by modeling the emission spectrum of electron transfer. *PLoS One*. 2020.
6. Cooper WG. Roles of evolution, quantum mechanics and point mutations in origins of cancer. *Cancer Biochem Biophys.* 1993; 13 (3): 147-170.
7. Luca Turin, *et al*. Electron spin changes during general anesthesia in *Drosophila. PNAS*. 2014; 111(34): 3524-3533.
8. Sechzer JA, *et al*. Aberrant parenting and delayed offspring development in rats exposed to lithium. *Biol Psychiatry.* 1986; 21 (13): 1258-1266.
9. Na Li, *et al*. Nuclear Spin Attenuates the Anesthetic Potency of Xenon Isotopes in Mice: Implications for the Mechanisms of Anesthesia and Consciousness. *Anesthesiology.* 2018; 129: 271–277.
10. Adams B, Petruccione F. Quantum effects in the brain: A review**.** *AVS Quantum Science.* 2020; 2 (2): 022901.
11. Stuart Hameroff, Roger Penrose. Consciousness in the universe: A review of the 'Orch OR' theory. *Physics of Life Reviews.* 2014; 11: 39-78.
12. Fisher MPA. Quantum Cognition: The possibility of processing with nuclear spins in the brain. *Annals of Physics.* 2015; 362: 593-602.
13. Tegmark M. The importance of quantum decoherence in brain processes. *Phys. Rev.* 2000; 61: 4194-4206.
14. Weingarten CP, *et al*. A New Spin on Neural Processing: Quantum Cognition. *Front Hum Neurosi*. 2016; 10: 541.
15. Lowe J, *et al*. Refined Structure of α/β Tubulin at 3.5 A Resolution. *J. Mol. Biol*. 2001; 313: 1045.
16. Ayoub AT, *et al*. Analysis of the Strength of Interfacial Hydrogen Bonds between Tubulin Dimers Using Quantum Theory of Atoms in Molecules. *Biophys J.* 2014; 107: 740-750.

Memantine Displays Antimicrobial Activity by Enhancing Escherichia coli Pathogen-Induced Formation of Neutrophil Extracellular Traps

Liang Peng[1], Li Li[2, 3], Xiao-Long He[4], Jing-Yi Yu[3], Zhi-Jie Zeng[4], Wei-Jun Yang[4], Bao Zhang[3, 4], Tie-Song Zhang[2], Hong Cao[4], Sheng-He Huang[2, 3, 4], Li-Qun Liu[5]

[1]Department of Clinical Laboratory, The Fifth Affiliated Hospital of Guangzhou Medical University, Guangzhou, China; [2]Kunming Key Laboratory of Children Infection and Immunity, Yunnan Institute of Pediatrics, Kunming Children's Hospital, Kunming, China; [3]Department of Pediatrics, Saban Research Institute, Childrens Hospital Los Angeles, University of Southern California, Los Angeles, CA, United States; [4]Guangdong Provincial Key Laboratory of Tropical Diseases, Department of Microbiology, Southern Medical University, Guangzhou, China; [5]Department of Pediatrics, The Second Xiangya Hospital, Central South University, Changsha, China

Corresponding author: Sheng-He Huang, E-mail: shhuang@usc.edu; Li-Qun Liu, E-mail: llq91217@163.com.

Note: Liang Peng, Li Li, Xiao-Long He and Jing-Yi Yu have contributed equally to this work.

ABSTRACT

Bacterial infection remains one of the leading causes of death worldwide due to the continuous rise of multiple antibiotic-resistant bacteria. Focusing solely on bacteria as the drug targets is a major limitation inherent in the conventional antibiotic therapy. Recently, host-directed therapies have become such an innovative approach to modulate the host defense system and the interplay of innate and adaptive immunity. Our previous studies showed that memantine (MEM), an α7 nAChR antagonist, could efficiently block multi-drug resistant Escherichia coli-caused bacteremia and meningitis in a mouse model. However, the underlying mechanisms that govern the antibacterial effects of MEM are still unknown. In this study, we demonstrated that MEM is able to significantly suppress *E. coli* infection by enhancing *E. coli*-induced formation and release of NETs *in vitro* and *in vivo*. MEM could promote the trapping and bactericidal activities of the polymorphonuclear neutrophils (PMNs) in a manner dependent on α7 nAChR, since knockdown of this receptor noticeably reduces the survival ability of bacteria in PMNs while MEM no longer affects the survival of bacteria in PMNs. Our results also showed that when the expression of S100A9, an antiseptic protein, is inhibited, pathogen survival rates in PMNs increase significantly. MEM reverses this effect in a concentration-dependent manner. MEM stimulates the production of MPO, S100A9, and DNA in PMNs and accelerates the release of depolymerized chromatin fibers into the extracellular space, suggesting the formation of NETs. Taken together, our data suggest that MEM effectively blocks bacterial infection through the promotion of the antibacterial function of NETs induced by *E. coli*.

Keyword: bacterial infection, antibiotic resistance, memantine, neutrophil extracellular traps, α7 nAChR

INTRODUCTION

The emergence of antibiotic resistance has become a severe public health problem. Bacteria resistant to multiple antibacterial agents such as carbapenem-resistant enterobacteriaceae (CRE), methicillin-resistant Staphylococcus aureus (MRSA),

vancomycin-resistant enterococci (VRE), extensively drug- resistant tuberculosis (XDR-TB), and extensively drug-resistant Acinetobacter baumannii (XDRAB) are often referred to as "superbugs." These bacteria infect at least 2 million people per year in the USA alone, with 23,000 dying as a direct result of these infections (Khan and Siddiqui, 2014). It suggests that there is an emergent need to develop new antibacterial drugs with novel strategies (Yu *et al*., 2015).

Host-directed therapies in adjunct to traditional antibiotic drugs become such innovative approaches to modulating the host defense system and the interplay of the innate and adaptive immunity (Munguia and Nizet, 2017). Development of a serious bacterial infection basically represents a failure of innate immune cells to execute their antimicrobial defense function (Munguia and Nizet, 2017). Pharmacologically targeting powerful immune cell killing and boosting the host defense system against pathogens could be an important way to treat infections, and would reduce frequencies in inducing drug resistance (Yu *et al*., 2015; Munguia and Nizet, 2017; Chiang *et al*., 2018).

Polymorphonuclear neutrophils (PMNs), the most abundant leukocytes in humans and other primates, play a central role in innate host defense against invading microorganisms (Hosoda *et al*., 2017). Activation of reactive oxygen species (ROS) is an important mechanism by which PMNs kill bacteria (Nguyen *et al*., 2017). Another important bacterial clearance pathway utilizes neutrophil extracellular traps (NETs), which are structures composed of granule proteins and nuclear constituents that are released by neutrophils. NETs have been shown to bind, disarm, and kill pathogens including both Gram-positive (Staphylococcus aureus, Streptococcus pneumoniae, and Group A streptococci), Gram-negative bacteria (Salmonella enterica erovar Typhimurium and Shigella flexneri), and certain fungi (Candida albicans). The granular components of NETs are peptides and enzymes (e.g., elastase and myeloperoxidase), and the nuclear constituents are chromatin DNA and histones (Brinkmann *et al*., 2004; Wartha *et al*., 2007b). Brinkmann *et al*. showed that neutrophils produce NETs when activated with interleukin-8 (IL-8), phorbolmyristate acetate (PMA), or lipopolysaccharide (Brinkmann *et al*., 2004).

Our previous studies on host-pathogen interplay show that α7 nAChR (α7R), an essential regulator of inflammation, is critical for the pathogenesis of *E. coli*-induced sepsis and meningitis (Chi *et al*., 2011, 2012). Using α7R KO *in vitro* and *in vivo* model systems, we have demonstrated that α7R plays a detrimental role in the genesis of bacteremia and the penetration of *E. coli* and neutrophils across the blood-brain barrier (BBB). These findings support the notion that α7R could serve as a unique drug target for broad-spectrum host-directed antimicrobial agents against bacterial infections, which lead to bacteremia and

all too often sepsis. Using *in vitro* and *in vivo* models of the BBB and RNA-seq (Yu *et al*., 2015), our drug repositioning studies have shown that memantine (MEM), an FDA-approved drug for the treatment of Alzheimer's disease (AD), efficiently blocks pathogenicities induced by meningitic Escherichia coli E44 and IHE2015 (a multiple antibiotic-resistant strain) in a manner dependent on α7R. In addition, we found that MEM efficiently inhibits bacteremia caused by *E. coli* in an animal model (Wang *et al*., 2015; Yu *et al*., 2015).

Notably, NETs have been shown to be an important antibacterial mechanism, since NETs can capture microbial pathogens and exert bactericidal activity through the action of antimicrobial peptides, histone and other NET-associated components (Hosoda *et al*., 2017). Our laboratory has demonstrated that α7R is an essential regulator of the host inflammatory response against bacteria (Chi *et al*., 2011). α7R-mediated inflammatory effects could be blocked by its antagonist, MEM (Yu *et al*., 2015). Based on these findings, we hypothesized that MEM interacts first with the drug target α7R and then induce NET-mediated bacterial killing in PMNs. In this study we tried to confirm our hypothesis that the formation of NETs is associated with the ability of MEM to block infection by using *in vitro* and *in vivo* models.

MATERIALS AND METHODS

Chemicals and Reagents

Memantine hydrochloride and the NETosis assay kit were purchased from Cayman Chemical (Ann Arbor, MI). The NET activator PMA, phagocytosis inhibitor Cytochalasin D, MPO antibody, and a S100A9 antibody were purchased from Abcam (Cambridge, MA). The neutrophil elastase (NE) ELISA Kit was purchased from R&D Systems (Minneapolis, MN). DNA fluorescent dye Picogreen was purchased from Thermo Fisher Scientific (Waltham, MA), CHRNA7 (α7R encoding gene), and S100A9 siRNA (small interfering RNA) kits were purchased from Santa Cruz Biotechnology (Santa Cruz, CA). The CHRNA7 antibody was purchased from GenScript (Piscataway, NJ). The S100A9 ELISA kit was purchased from CUSABIO (Wuhan, China).

Bacterial Strains and Culture Conditions

Escherichia coli E44 is a rifampin-resistant strain derived from the RS218 strain (O18: K1: H7), which is a clinical isolate from the cerebrospinal fluid (CSF) of neonates with meningitis (Huang *et al*., 2001). RS218 and E44 have the same virulence phenotypes. E44-green fluorescent protein (GFP) is an E44 strain containing a GFP vector. Bacteria were cultured in L broth at 37ºC overnight without agitation, unless otherwise specified.

Detection of DNA and Neutrophil Elastase

The Ficoll-Paque method was used to isolate neutrophils from blood, and subsequently 1 × 10 PMNs were cultured in each well of a 96-well-plate. The cells were then treated with 100 nm PMA, different concentrations of E44, or E44 along with MEM for 4 h. After the fluorescent DNA dye Picogreen was added and incubated with the samples for 10 min, the fluorescence value of every group was estimated with fluorescence microplate reader. Neutrophil elastase activity was measured using NETosis assay kit (Cayman Chemical) according to the manufacturer's instruction.

Neutrophil Killing Assays

Neutrophil killing assays were performed as described by Katharina Beiter *et al*. (2006). A total of 1 × 10^6 PMNs were seeded in 24 well-plates and cultured with RPMI medium (containing 10 mM HEPES and 2% heat-inactivated human serum) with or without Cytochalasin D, which is a phagocytosis inhibitor. The cells were treated with *E. coli* E44 (MOI = 50) and different concentrations of MEM (1, 5, 25 μM) for 2 h. The bacteria were then collected and enumerated after being cultured on LB agar plates containing rifampicin (30 μg/ml). Neutrophil killing was calculated on the basis of the number of colony- forming units (CFUs) recovered from wells with neutrophils and the CFUs recovered from wells without neutrophils. NET- mediated killing was calculated on the basis of the number of CFUs recovered from Cytochalasin-D-treated neutrophils and the CFUs recovered from Cytochalasin-D-treated wells without neutrophils. Intracellular killing was determined as the difference between total killing and extracellular killing.

Quantification of trapping was performed as described by Wartha *et al*. (2007a). Neutrophils were seeded and activated with 25 nM PMA for 10 min. After washing, cells were treated with 10 mg/ml Cytochalasin D to inhibit phagocytosis. An MOI of 50 was used for infection with *E. coli* E44, and different concentrations of MEM were incubated with the cells. After brief centrifugation and incubation for 5 min, the supernatant was removed and used for serial plating to quantify viable bacteria. The cells were subsequently treated for 15 min with RPMI ± DNase (20 U/ml) to dissolve NETs. Viable bacteria were quantified by the plating of serial dilutions. The percentage of CFUs trapped in NETs was calculated with the following formula: %trapped = [(CFUDnase - CFURPMI) / (CFUDnase + CFUsupernatant)] × 100. CFUDNase represents total numbers of untrapped and trapped bacteria since the DNase concentration of 20 U/ml did not affect bacterial viability. Under the condition without addition of DNase, the trapped bacteria were killed by NETs and the CFURPMI represent the viable untrapped bacteria. The relative trapping was calculated with

the following formula: (%trapped in groups treated with MEM /% trapped in groups without MEM treatment) × 100.

To analyze DNA release from neutrophils induced by PMA, *E. coli*, or/and MEM, the DNA fluorescent dye Picogreen was added and incubated with the samples for 10 min, and the fluorescence value of every group was then estimated. Neutrophils without any treatment were used as the control group.

CHRNA7 and S100A9 Knockdown Experiments

Knockdown experiments were performed using human CHRNA7 and S100A9 siRNA (small interfering RNA) kits from Santa Cruz Biotechnology as described previously (Ichikawa *et al*., 2011; Schaal *et al*., 2018). Opti-MEM (Gibco Life Technologies) and Lipofectamine 2000 transfection reagent (Invitrogen, USA) were used to transfect HL60 cells with siRNAs according to the supplier's recommendations. An unspecific scrambled siRNA was served as control. HL-60 cells were inoculated in 24-well plate and siRNA knockdown experiments were performed using a final siRNA concentration of 25 pmol with 2 μL transfection reagent per well. Media was replaced by complete medium containing 10% FBS 4–6 h after transfection. After replacing the medium and incubating for an additional 24 h, cells were used for western blot analysis, survival assays, and immunofluorescence assays.

Human Neutrophil Isolation

Neutrophils were isolated from the peripheral blood of healthy donors as described by Halverson *et al*. (2015). The ethics committee of Southern Medical University (SMU) approved the study. Written informed consent was obtained from all participants. At first, whole blood was collected and mixed 5:1 in acid citrate dextrose. Red blood cells were then removed using dextran sedimentation and hypotonic lysis with KCl. The cell pellet was subjected to Ficol-Histopaque density centrifugation after the red blood cells had been lysed. The subsequent pellet was resuspended in 2 mL of HBSS (Hank's balanced salt solution, Invitrogen 14175-095). To determine the viable cell concentration, the collected cells were counted using a hemocytometer and Trypan blue staining.

Immunofluorescence Microscopy

PMNs separated from blood were incubated with E44, MEM, and PMA. PMNs without any treatment were used as the control group. After blocking with 5% (w/v) BSA in PBS, the cells were stained with primary antibodies against S100A9 or MPO at 4ºC overnight, then treated with a secondary antibody labeled with PE or FITC at room temperature for 1 h. The

cells were immersed in mount medium containing DAPI, and examined under a fluorescence microscope at the Congressman Dixon Cellular Imaging Core Facility, Children's Hospital, Los Angeles. To ensure that the fluorescence strength of each treatment was comparable, all the images were acquired with the same parameters.

Mice

C57BL/6J mice were obtained from the Animal Experimental Center of SMU. The animals were used at 6–8 weeks of age. All experiments were approved by the Animal Care and Ethics Committee of SMU. Mice (6 per group) were intraperitoneally injected with 2×10^7 E44 or with 2×10^7 E44 along with different concentrations of MEM (5–20 mg/kg of body weight). After infection with E44 for 24 h, mice were anesthetized and blood, liver, lung, and spleen tissue was collected. Blood samples were diluted and cultured on BHI agar plates containing rifampicin. Liver, lung, and spleen tissue was weighed, triturated, diluted, and cultured on BHI agar plates containing rifampicin.

Statistical Analysis

The data were analyzed by ANOVA and covariates were followed by a multiple comparison test such as the Newmann-Keuls test to determine the statistical significance between the control and treatment groups. Graph Pad Prism v5.0 software was used. Comparisons with a $p<0.05$ were considered to be statistically significant.

RESULTS

MEM Promoted the E44-Induced Formation of NETs

DNA is a major component of NETs. Accordingly, we measured DNA release from neutrophils in order to assess NET formation. As shown in Figure 1A, MEM was able to enhance DNA release from PMNs infected with E44 in a concentration-dependent manner when compared to the control without treatment. Additionally, we measured the formation of neutrophil elastase (NE) using the NETosis assay kit. Similar to what was found when DNA release was analyzed, while E44 alone stimulated the production of NE, MEM was able to significantly promote E44-indcued NE release in a concentration-dependent manner (Figure 1B). These results indicate that MEM enhances E44- induced NET formation.

MEM Promoted NET-Mediated Bacteria Trapping and Killing

Neutrophils kill bacteria either by phagocytosis (intracellular killing) or with NETs

(extracellular killing). A phagocytosis inhibitor Cytochalasin D was used to distinguish intracellular killing and extracellular killing. A total of 1×10^6 PMNs were cultured in 24-well plates with or without Cytochalasin D, and the cells were treated with E44 (MOI = 50) and different concentrations of MEM (0, 1, 5, and 25 μM) for 2 h. Subsequently, the bacteria were cultured on BHI agar plates, collected, and counted. As shown in Figure 2A, MEM significantly promoted the killing effect of PMNs on E44, including both intracellular killing and extracellular killing, in a concentration-dependent manner. Additionally, we found that

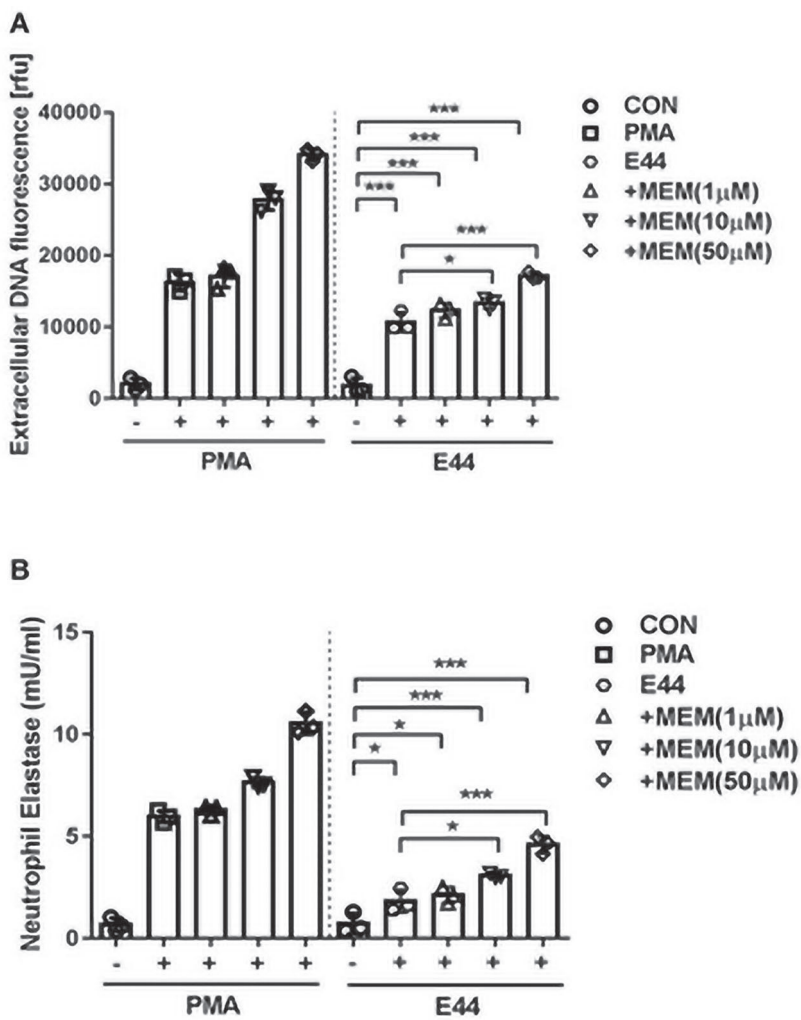

FIGURE 1. MEM enhanced E44-induced formation of NETs. (A) Detection of extracellular DNA using fluorescence microscope after the neutrophils infection with *E. coli* E44. A number of 1×10^5 collected PMNs was cultured in 96 well-plates. The cells was treated with 100 nm PMA (positive control) or E44 for 4 h. Then the released DNA was detected with the DNA fluorescent dye of Picogreen; (B) The expression levels of neutrophil elastase (NE) in neutrophils treated with PMA or E44 along with MEM. Bar graphs show the means ± SD of three different experiments. Scatter plots in the bar graphs represent the three biological replicates. Significant differences with regard to the controls are marked by asterisks (*P < 0.05; ***P < 0.001).

when DNA was digested with DNase, MEM promoted NET trapping in a concentration-dependent manner (Figure 2B). As shown in Figures 2C,D, MEM was able to enhance the intracellular killing ability of PMNs. It is worth noting that when the MOI was <50, the

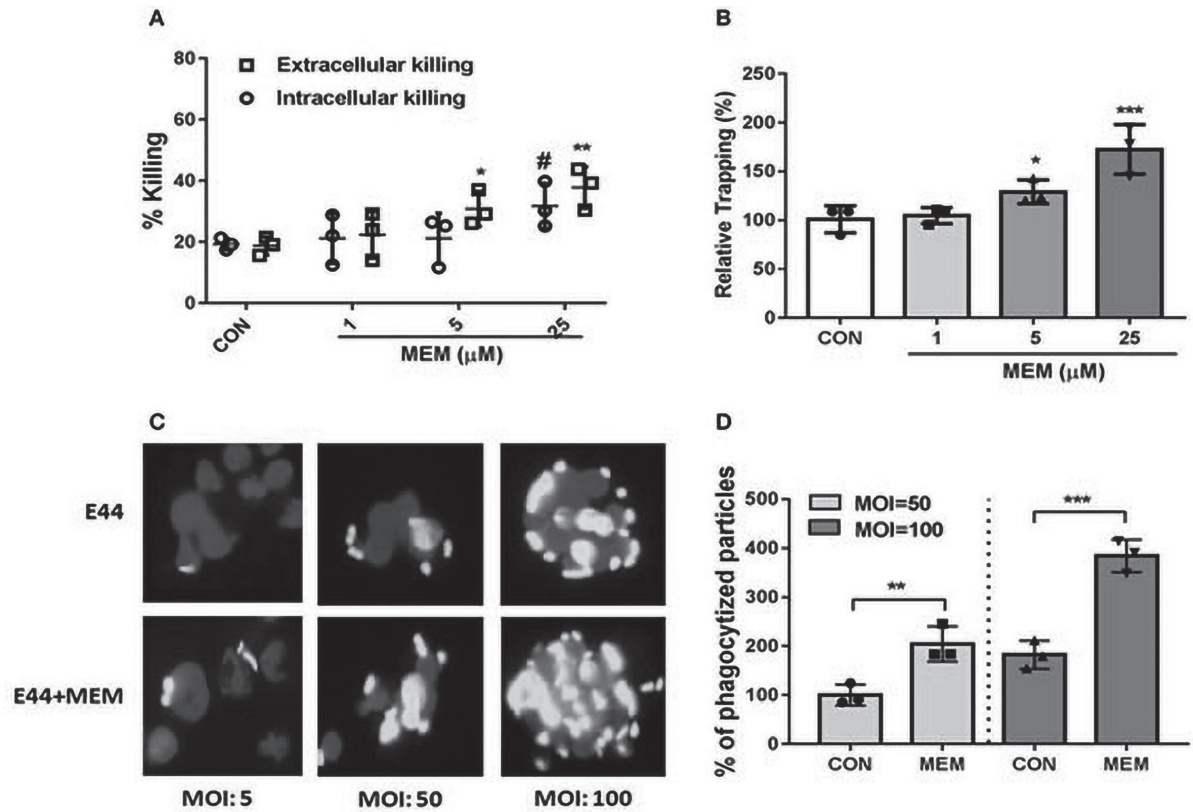

FIGURE 2. MEM enhanced bacterial killing by neutrophils. (A) Intracellular and extracellular killing of *E. coli* E44 after treatment with MEM. Neutrophil killing of bacteria includes two parts: intracellular killing and extracellular killing. A intracellular killing inhibitor of Cytochalasin D was used to distinguish intracellular killing of PMNs and extracellular killing microbes; (B) NETs trapping promoted by MEM. Neutrophils were stimulated for NET formation and infected with E44 at an MOI of 50. Different concentration of MEM was incubated with the neutrophils. Viable bacteria were quantified by plating of serial dilutions. The percentage of CFU trapped by NETs was calculated according to the formula described in section Materials and Methods; (C) MEM could enhance the intracellular killing ability of PMNs. Different MOI (5, 50, 100) was used for infection with E44-GFP, and a concentration of 50 μM MEM was added and incubated with PMNs for 1 h. PMNs without bacteria infection was used as a control group. Then the cells were collected by centrifuge and fixed on slide. DAPI was used for cell staining of nucleus (blue fluorescence). The intracellular killing of bacteria (green fluorescence) by neutrophils was counted, and 100 of neutrophils was assessed for each sample; (D) Phagocytized particles in PMNs treated with E44 or/and MEM. Phagocytized particles were counted under a fluorescence microscopy. CON represents cell treated with E44, and MEM group represents cell treated with E44 and memantine. Each bar represents the average of three different experiments ± SD (n = 3). Scatter plots in the bar graphs represent the three biological replicates. # $P < 0.05$ (P value of the intracellular killing %), *$P < 0.05$, **$P < 0.01$, ***$P < 0.001$ (P value of the extracellular killing %).

PMNs did not show an obvious change in morphology. However, when the MOI was >50, each PMN was observed to contain at least 50 E44 bacteria, along with a significant nuclear morphology change. Collectively, these results suggest that MEM not only promotes the formation of NETs, but also enhances the NET-mediated bacterial trapping and killing of *E. coli* E44.

MEM Enhanced the NET Function and Inhibits *E. coli* Dissemination *in vivo*

Mice were intraperitoneally injected with 2×10^7 E44 or 2×10^7 E44 along with different concentrations of MEM. Twenty four hours later, the mice were anesthetized and blood was collected. The serum was analyzed using Picogreen and the Mouse PMN elastase ELISA Kit (R&D Systems) to quantify the formation of NETs. As shown in Figures 3A,B, E44 significantly stimulated the release of DNA and elastase into blood. These results suggest that MEM promotes the formation of NETs *in vivo* after *E. coli* E44 infection.

To explore whether MEM blocks E44 dissemination, mice were intraperitoneally injected with 2×10^7 E44 or 2×10^7 E44 along with different concentrations of MEM. After infection with E44 for 24 h, the mice were anesthetized and blood, liver, lung, and spleen tissue was collected. Blood samples were diluted and cultured on BHI agar plates containing rifampicin. The liver, lung, and spleen tissue was weighed, triturated, diluted, and cultured on BHI agar plates containing rifampicin. As shown in Figures 3C–F, MEM effectively blocked the dissemination of E44 in infected mice.

CHRNA7 Knockdown Led to a Failure of MEM-Enhanced Intracellular Killing Ability of PMNs

S100A9 and α7R are both involved in the regulation of Ca^{2+} - mediated signal transduction. S100A9 is also an antimicrobial protein which is released by PMNs during bacterial infection. HL60 cells were stimulated with 1.3% DMSO to generate PMNs. A total of 1×10^6 PMNs of differentiated PMNs were cultured in 24-well plates and transfected with CHRNA7 or S100A9 siRNA using lipofectmine 2000. After the CHRNA7 and S100A9 genes were knocked down using siRNA, the intracellular killing ability of PMNs was tested (Figure 4A). demonstrated that MEM could enhance the intracellular killing ability of neutrophils in a manner of dose dependent. As shown in Figure 4B, the survival rate of E44 in the CHRNA7 knockdown group was significantly lower than that of the normal group. The addition of MEM did not affect the intracellular killing ability of PMNs, even when the concentration of MEM reached 50 μM. As shown in Figure 4C, after knockdown of S100A9, the survival rate of E44 in PMNs increased when compared to the normal group.

MEM Promoted the Expression of theBactericidal Enzyme MPO and S100A9

PMNs were treated with PMA, *E. coli* E44, and different doses of MEM. Subsequently, these cells were analyzed using immunofluorescence. To detect the formation of NETs, all cell samples were incubated with fluorescent MPO (green) and S100A9 (red) antibodies, and nuclei were stained by DAPI. The fluorescence value was analyzed with Image J software, and the relative fluorescence value was calculated as the fluorescence values of treatment groups/the fluorescence value of control group. Under the fluorescence microscope, we

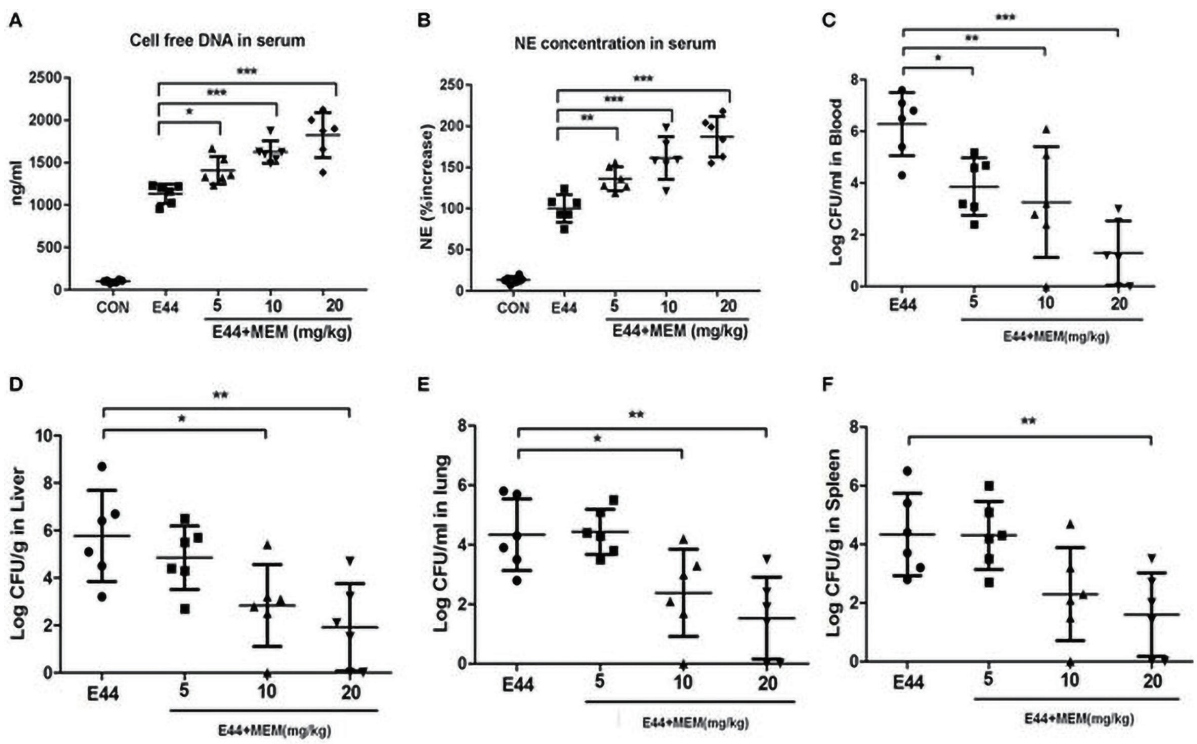

FIGURE 3. MEM promoted NETs formation and could block E44 dissemination in mouse model. Mice (6 per group) were intraperitoneally injected with 2 × 107 E44 or with 2 × 107 E44 along with different concentrations of MEM (5–20 mg/kg of body weight). After infection with E44 for 24 h, mice were anesthetized and blood, liver, lung, and spleen tissue was collected. The serum used to detect the cell free DNA using Picogreen and NE using a Mouse PMN Elastase ELISA kit. For NE detection, the serum was diluted 1:2. The blood was diluted from 1:10 to 1:108 and cultured on BHI agar plates containing rifampicin. Liver, lung, and spleen tissue was weighed, triturated, diluted, and cultured on BHI agar plates containing rifampicin. (A) Cell free DNA in serum; (B) NE concentration in serum; (C) The bacterial levels in blood of mice; (D) The bacterial levels in liver tissue of mice; (E) The bacterial levels in lung tissue of mice; (F) The bacterial levels in spleen tissue of mice. The mice were treated as described in Materials and Methods, and then the blood, liver, lung, and spleen tissues were collected. Blood samples were diluted and cultured on the BHI agar plates. The liver, lung, and spleen tissues were weighted and triturated, then diluted and cultured on the BHI agar plates. All values represent the means of determinations. Bacteria levels in blood are expressed as log CFU/ml, and in tissues are expressed as log CFU/g. *P < 0.05, **P < 0.01, ***P < 0.001.

observed that the nuclei of the control group cells maintained a segmented structure. However, the nuclear structures of cells in the groups treated with PMA, E44, and MEM were damaged significantly. These cells exhibited a mass production of MPO, S100A9, and DNA (Figures 5A–D). Additionally, depolymerized chromatin fibers were released into the extracellular space and formed a network structure, suggesting the formation of NETs. The expression level of S100A9 in cell culture medium induced by the MEM was also detected using ELISA method. The data as shown in Figure 5E demonstrated that MEM could

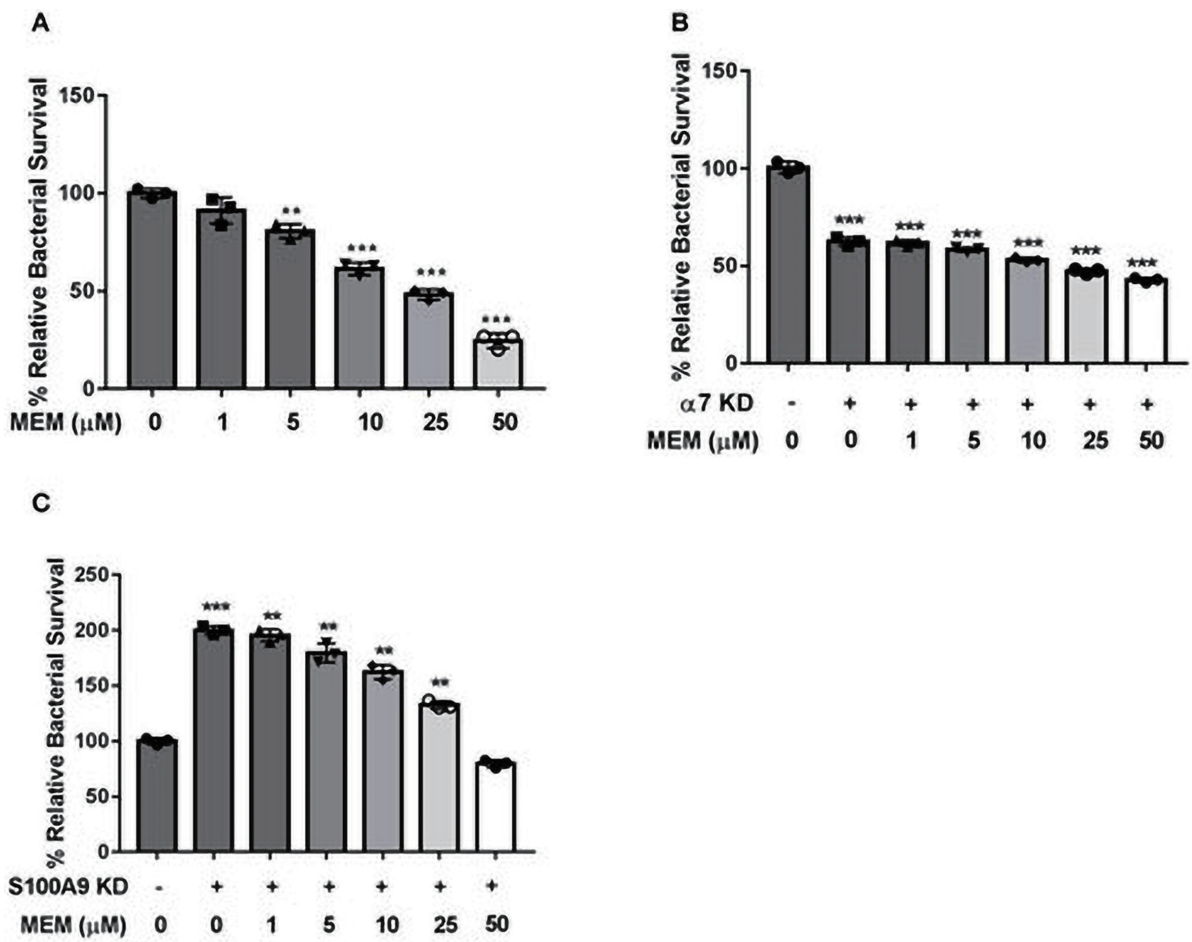

FIGURE 4. CHRNA7 knockdown led to a failure of MEM-enhanced intracellular killing ability of PMNs. A total of 1 × 106 of PMNs were cultured in 24-well plates and transfected with CHRNA7 or S100A9 siRNA. Cells were treated with *E. coli* E44 (MOI = 50) or/and different concentrations of MEM for 2 h. (A) Bacterial survival in PMNs with titration of memantine treatment; (B) Survival of E44 in PMNs with (+) or without (–) CHRNA7 knockdown after treatment with different concentration of MEM; (C) Survival of E44 in PMNs with (+) or without (–) S100A9 knockdown after treatment with different concentration of MEM. Relative survival was expressed as an n-fold increase or decrease relative to the basal level (Cells without siRNA and MEM treatment). Each bar represents the average of three different experiments ± SD. Scatter plots in the bar graphs represent the three biological replicates. **P < 0.01, ***P < 0.001 compared with the control.

significantly induce the expression of S100A9. Gene expression knockdown by transfection of siRNAs into PMNs weakened the promotion effects of E44 and MEM on the expression of MPO and S100A9 (Supplementary Data).

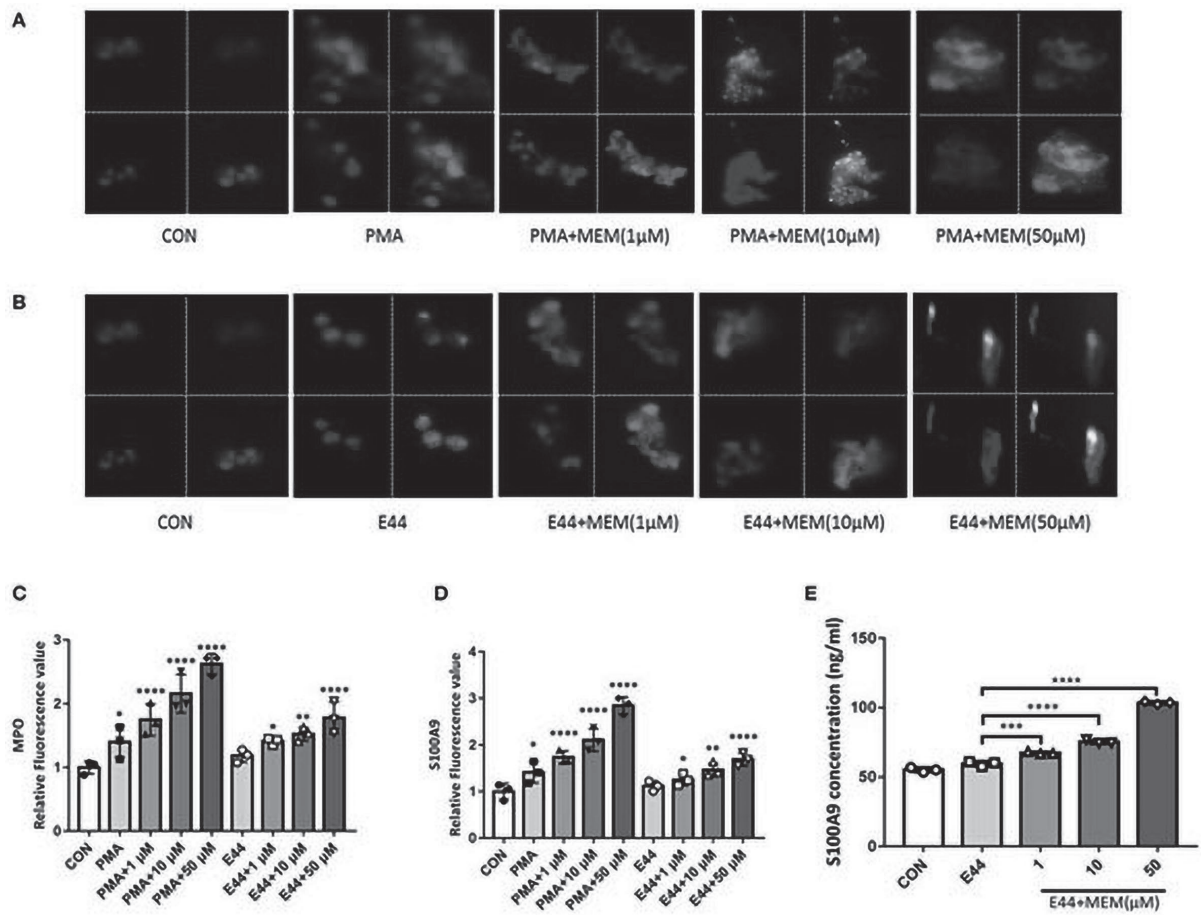

FIGURE 5. MEM promoted the expression of bactericidal enzyme MPO and antiseptic protein S100A9. The PMNs were treated with PMA, *E. coli* E44, different dose of MEM, and then incubated with fluorescent conjugated antibodies of MPO and S100A9, and the cell nucleus was stained with DAPI. (A) Expression of MPO and S100A9 in cells treated with PMA or PMA in combination with different concentration of MEM; (B) Expression of MPO and S100A9 in cells treated with E44 and different concentration of MEM; (C) Quantitative analysis of the relative fluorescence value of MPO induced by PMA, E44, and MEM; (D) Quantitative analysis of the relative fluorescence value of S100A9 induced by PMA, E44, and MEM; (E) Expression level of S100A9 in culture medium induced by E44 or/and MEM. A total of 1×10^6 of PMNs were cultured in 24-well plates, and treated with *E. coli* E44 or/and different dose of MEM for 2 h. Then the samples were collected and centrifuged. The S100A9 in the supernatant was detected using the S100A9 ELISA kit according to the manufacturer's instructions. Each bar represents the average of three different experiments ± SD. Scatter plots in the bar graphs represent the three biological replicates. *P < 0.05, **P < 0.01, ***P < 0.001, ****P < 0.0001 compared with the control. Colors: MPO is shown in green; S100A9 is shown in red; Cell nucleus stained with DAPI is shown in blue.

DISCUSSION

NETs have been considered to be a component of human innate immunity due to their ability to trap and kill pathogens. NETs are produced by activated neutrophils and consist of a DNA backbone with embedded antimicrobial peptides and enzymes. Granule proteins, histones, and chromatin together form an extracellular structure that traps and prevents the spread of bacteria (Brinkmann *et al*., 2004; Wartha *et al*., 2007b; Halverson *et al*., 2015). Proteases such as neutrophil elastase embedded in NETs degrade virulence factors (IpaB of S. flexneri and a toxin of S. aureus) (Weinrauch *et al*., 2002), bactericidal permeability-increasing protein (BPI), and histones. NETs also kill bacteria efficiently, and at least one of the NET components, histone, exerts antimicrobial activity at surprisingly low concentrations (Brinkmann *et al*., 2004).

In this study, we observed that pathogen-induced NET formation, including the release of elastase and DNA from neutrophils, was increased when the infected cells were incubated with MEM. In the mouse infection model, MEM could also induce the formation of NETs and inhibited the dissemination of *E. coli*. When compared to the control group, the distribution of bacteria in blood, liver, lung, and spleen tissues was significantly less in the MEM-treated group.

Previous reports suggest that α7R plays a detrimental role in the host defense against *E. coli* infection. It has been has confirmed that α7R is expressed on many types of cells, such as endothelial cells, fibroblasts, synoviocytes, polymorphonuclear neutrophils, dendritic cells, NK cells, B cells, and T cells (Tracey, 2009). Meningitic *E. coli* and nicotine can additively or synergistically induce the cellular release of Ca^{2+} which may expand bacterial cell signaling through the cholinergic α7R pathway (Chi *et al*., 2011). S100A9 is expressed abundantly in neutrophils and is able to regulate the ability of neutrophils to respond acutely to infection (Raquil *et al*., 2008; De Filippo *et al*., 2014; Yoshioka *et al*., 2016). The presence of S100A9 is critical in both murine and human NETs to inhibit bacterial growth (Achouiti *et al*., 2012). Results from the PMN intracellular killing assay indicate that the survival rate of E44 in the α7R knockdown group was significantly lower than that of the control group. Treatment with MEM did not affect the intracellular killing ability in this context. In contrast, after knockdown of S100A9, the bacterial survival rate in PMNs increased when compared to the control group. Furthermore,

MEM inhibited bacterial survival in PMNs in which S100A9 was knocked down in a concentration-dependent manner. MEM could significantly stimulate the production of MPO, S100A9, and DNA in PMNs and accelerated the release of depolymerized chromatin fibers

into the extracellular space, suggesting the formation of NETs.

Further investigation of factors that modulate the cytoplasmic EF-hand Ca^{2+} -binding protein S100A9-mediated signaling pathway may reveal more insights into the mechanisms responsible for enhancement of neutrophil antimicrobial activity. S100A9 could be regulated by phosphorylation, but the importance of this phosphorylation on the NET activity of this protein has not yet been extensively studied (Schenten *et al*., 2018). Along these lines, it is interesting to determine if the enhancement of NET release and bactericidal activity is phosphorylation-dependent. Exploring the mechanism underlying phosphorylated S100A9-induced NET formation may facilitate discovery of signaling molecules specifically optimized to promote targeted enhancement of innate immune responses. Also, it is important to examine the impact of this phosphorylation on pro-inflammatory cytokine expression and secretion in neutrophils.

In conclusion, our data provide evidence that MEM is a host-directed antimicrobial agent that has the potential to be developed as a novel therapeutic for the treatment of bacterial infection. Furthermore, our data demonstrate a potential mechanism by which MEM exerts antimicrobial functions related to the promotion of pathogen-induced NET formation.

DATA AVAILABILITY STATEMENT

All datasets generated for this study are included in the article/Supplementary Material.

ETHICS STATEMENT

The studies involving human participants were reviewed and approved by Ethics Committee of Southern Medical University. The patients/participants provided their written informed consent to participate in this study. The animal study was reviewed and approved by Animal Care and Ethics Committee of Southern Medical University.

AUTHOR CONTRIBUTIONS

S-HH, LP, L-QL, LL, J-YY, and X-LH conceived and designed the experiments. J-YY, LP, X-LH, LL, L-QL, Z-JZ, W-JY, and BZ performed the experiments. LP, X-LH, S-HH, J-YY, HC, and T-SZ analyzed the data. LP, S-HH, J-YY, X-LH, and HC contributed with reagents, materials, and analysis tools. LP, L-QL, S-HH, and J-YY wrote the paper.

FUNDING

This work was financially supported by the Public Health Service grant (R21NS083967 to S-HH), and the National Natural Science Foundation of China (No. 81670637 to LP; No. 81871198 to HC; No. 81873762 to L-QL). The funders had no role in study design, data collection and analysis, decision to publish, or preparation of the manuscript.

ACKNOWLEDGMENTS

This study assessed the value of technical assistance provided by Dr. Ambrose Jong and Ms. Chun Hua Wu.

SUPPLEMENTARY MATERIAL

The Supplementary Material for this article can be found online at: https://www.frontiersin.org/articles/10.3389/fcimb.2020.00047/full#supplementary-material.

CONFLICT OF INTEREST

The authors declare that the research was conducted in the absence of any commercial or financial relationships that could be construed as a potential conflict of interest.

REFERENCES

Achouiti, A., Vogl, T., Urban, C. F., Rohm, M., Hommes, T. J., van Zoelen, M. A., *et al*. (2012). Myeloid-related protein-14 contributes to protective immunity in gram-negative pneumonia derived sepsis. PLoS Pathog 8:e1002987. doi: 10.1371/journal.ppat.1002987

Beiter, K., Wartha, F., Albiger, B., Normark, S., Zychlinsky, A., and Henriques- Normark, B. (2006). An endonuclease allows Streptococcus pneumoniae to escape from neutrophil extracellular traps. Curr. Biol. 16, 401–407. doi: 10.1016/j.cub.2006.01.056

Brinkmann, V., Reichard, U., Goosmann, C., Fauler, B., Uhlemann, Y., Weiss, D. S., *et al*. (2004). Neutrophil extracellular traps kill bacteria. Science 303, 1532–1535. doi: 10.1126/science.1092385

Chi, F., Bo, T., Wu, C. H., Jong, A., and Huang, S. H. (2012). Vimentin and PSF act in

concert to regulate IbeA+ *E. coli* K1 induced activation and nuclear translocation of NF- κB in human brain endothelial cells. PLoS ONE 7:e35862. doi: 10.1371/journal.pone.0035862

Chi, F., Wang, L., Zheng, X., Wu, C. H., Jong, A., Sheard, M. A., *et al*. (2011). Meningitic Escherichia coli K1 penetration and neutrophil transmigration across the blood-brain barrier are modulated by alpha7 nicotinic receptor. PLoS ONE 6:e25016. doi: 10.1371/journal.pone.0025016

Chiang, C. Y., Uzoma, I., Moore, R. T., Gilbert, M., Duplantier, A. J., and Panchal, R. G. (2018). Mitigating the impact of antibacterial drug resistance through host-directed therapies: current progress, outlook, and challenges. MBio 9:e01932-17. doi: 10.1128/mBio.01932-17

De Filippo, K., Neill, D. R., Mathies, M., Bangert, M., McNeill, E., Kadioglu, A., *et al*. (2014). A new protective role for S100A9 in regulation of neutrophil recruitment during invasive pneumococcal pneumonia. FASEB J. 28, 3600–3608. doi: 10.1096/fj.13-247460

Halverson, T. W., Wilton, M., Poon, K. K., Petri, B., and Lewenza, S. (2015). DNA is an antimicrobial component of neutrophil extracellular traps. PLoS Pathog. 11:e1004593. doi: 10.1371/journal.ppat.1004593

Hosoda, H., Nakamura, K., Hu, Z., Tamura, H., Reich, J., Kuwahara-Arai, K., *et al*. (2017). Antimicrobial cathelicidin peptide LL 37 induces NET formation and suppresses the inflammatory response in a mouse septic model. Mol. Med. Rep. 16, 5618–5626. doi: 10.3892/mmr.2017.7267

Huang, S. H., Wan, Z. S., Chen, Y. H., Jong, A. Y., and Kim, K. S. (2001). Further characterization of Escherichia coli brain microvascular endothelial cell invasion gene ibeA by deletion, complementation, and protein expression. J. Infect. Dis. 183, 1071–1078. doi: 10.1086/319290

Ichikawa, M., Williams, R., Wang, L., Vogl, T., and Srikrishna, G. (2011).S100A8/A9 activate key genes and pathways in colon tumor progression. Mol. Cancer Res. 9, 133–148. doi: 10.1158/1541-7786.MCR-10-0394

Khan, N. A., and Siddiqui, R. (2014). War on terror cells: killing the host that harbours 'superbugs' is an infection control strategy in our fight against infectious diseases. Pathog. Glob. Health 108, 4–10. doi: 10.1179/2047773213Y.0000000125

Munguia, J., and Nizet, V. (2017). Pharmacological targeting of the host-pathogen interaction: alternatives to classical antibiotics to combat drug-resistant superbugs. Trends Pharmacol. Sci. 38, 473–488. doi: 10.1016/j.tips.2017.02.003

Nguyen, G. T., Green, E. R., and Mecsas, J. (2017). Neutrophils to the ROScue: mechanisms of NADPH oxidase activation and bacterial resistance. Front. Cell Infect Microbiol. 7:373. doi: 10.3389/fcimb.2017.00373

Raquil, M. A., Anceriz, N., Rouleau, P., and Tessier, P. A. (2008). Blockade of antimicrobial proteins S100A8 and S100A9 inhibits phagocyte migration to the alveoli in streptococcal pneumonia. J. Immunol. 180, 3366–3374. doi: 10.4049/jimmunol.180.5.3366

Schaal, C. M., Bora-Singhal, N., Kumar, D. M., and Chellappan, S. P. (2018).Regulation of Sox2 and stemness by nicotine and electronic-cigarettes in non-small cell lung cancer. Mol Cancer 17:149. doi: 10.1186/s12943-018-0901-2

Schenten, V., Plancon, S., Jung, N., Hann, J., Bueb, J. L., Brechard, S., *et al*. (2018). Secretion of the phosphorylated form of S100A9 from neutrophils is essential for the proinflammatory functions of extracellular S100A8/A9. Front. Immunol. 9:447. doi: 10.3389/fimmu.2018.00447

Tracey, K. J. (2009). Reflex control of immunity. Nat. Rev. Immunol. 9, 418–428. doi: 10.1038/nri2566

Wang, S., He, X., Yu, J. Y., Neely, M., Zhang, L., Peng, L., *et al*. (2015).Characterisation of a multidrug-resistant meningitic Escherichia coli strain (O75:K1:H5) isolated from an infant that is sensitive to memantine, a newly identified host-directed antimicrobial drug. Int. J. Antimicrob. Agents 46, 598–600. doi: 10.1016/j.ijantimicag.2015.08.002

Wartha, F., Beiter, K., Albiger, B., Fernebro, J., Zychlinsky, A., Normark, S., *et al*. (2007a). Capsule and D-alanylated lipoteichoic acids protect Streptococcus pneumoniae against neutrophil extracellular traps. Cell Microbiol. 9, 1162–1171. doi: 10.1111/j.1462-5822.2006.00857.x

Wartha, F., Beiter, K., Normark, S., and Henriques-Normark, B. (2007b).Neutrophil extracellular traps: casting the NET over pathogenesis. Curr. Opin. Microbiol. 10, 52–56. doi: 10.1016/j.mib.2006.12.005

Weinrauch, Y., Drujan, D., Shapiro, S. D., Weiss, J., and Zychlinsky, A. (2002). Neutrophil elastase targets virulence factors of enterobacteria. Nature 417, 91–94. doi: 10.1038/417091a

Yoshioka, Y., Mizutani, T., Mizuta, S., Miyamoto, A., Murata, S., Ano, T., *et al*. (2016). Neutrophils and the S100A9 protein critically regulate granuloma formation. Blood Adv. 1, 184–192. doi: 10.1182/bloodadvances.2016000497

Yu, J. Y., Zhang, B., Peng, L., Wu, C. H., Cao, H., Zhong, J. F., *et al*. (2015).Repositioning of memantine as a potential novel therapeutic agent against meningitic *E. coli*-induced

pathogenicities through disease-associated alpha7 cholinergic pathway and RNA sequencing-based transcriptome analysis of host inflammatory responses. PLoS ONE 10:e0121911. doi: 10.1371/journal.pone.0121911

A note from USACSA editorial board: this article contributed by authors has been published at Frontiers in Cellular and Infection Microbiology 10:47, 2020.

Rupture Zones of the 2014 M6 South Napa Earthquake in California Characterized by Fault-Zone Trapped Waves

Yong-Gang Li

University of Southern California, Los Angeles California 90089, USA

ABSTRACT

We use fault-zone trapped waves (FZTWs) to evaluate continuity between the West Napa (WNF) and Franklin (FF) faults and fault branching within the WNF zone in northern California. The FZTWs generated by 55 on-fault aftershocks of the 24 August 2014 Mw 6.0 South Napa earthquake are identified in three-component seismograms recorded at three dense arrays deployed across the resulting surface ruptures. Our 3D finite-difference simulations of the recorded FZTWs show that the WNF zone consists of a 400- to 500-m-wide, 5- to 7-km-deep, low-velocity waveguide, with seismic velocities reduced by 40 to 50%. Post-S coda durations of the FZTWs increase with distance between the aftershocks and the recording arrays, demonstrating that the low-velocity waveguide extends southward to the FF, within which seismic velocities are reduced by 30-35%. These FZTWs indicate that the combined WNF-FF zone is at least ~54 km long. The FZTWs generated by two explosions detonated within the main surface rupture of the WNF and recorded by a 15-km-long seismic array across the fault zone, demonstrate that the rupture is highly distributed on the multiple fault strands during the M6 South Napa earthquake. Within 1.5 km of the main 2014 surface rupture, there are at least two subordinate fault traces that formed 3- to 6-km-long surface ruptures. Finite-difference modeling suggests these subordinate rupture zones form low-velocity waveguides and

Corresponding author: Yong-Gang Li, University of Southern California, Los Angeles California 90089, USA. E-mail: ygli@usc.edu.

connect with the main rupture at ~2-3 km depth. FZTWs recorded at the Carneros Fault (CF), ~1-km west of the WNFZ, suggest that the CF connects with the WNFZ at shallow depths, even though there was not surface rupture on the CF during the 2014 earthquake. We suggest that the continuous and widely distributed WNF-FF may pose significant regional hazards from amplification and extended ground shaking along the fault-zone waveguides, even if surface rupture is limited to only a segment of the overall fault zone.

INTRODUCTION

The 2014 South Napa *M*6 mainshock occurred at a depth of 9.4-km, with aftershocks extending between 2 km and 12 km depth (Hardebeck and Shelly, 2014). The mainshock epicenter was located ~6 km northwest of the City of American Canyon and 1.7 km south of the southernmost mapped surface rupture. The epicenter was also close to mapped trace of the less known fault, the Franklin fault (FF) (Bryant, 2005; Graymer *et al*., 2002; Wesling and Hanson, 2008). However, the surface rupture did not fall on the main trace of any of these faults, but instead between the Carneros and West Napa faults and northwest along strike from the northern mapped end of the FF. 3D surfaces show that the Carneros Fault is a steeply dipping fault that runs just west of the near-vertical 2014 rupture plane (Graymer, 2014). The Carneros Fault does not appear to have been involved in the earthquake, although relocated aftershocks suggest possible minor triggered slip. To south, the FF is a steeply east-dipping fault, suggesting that the South Napa earthquake occurred on the northernmost reach of the FF within its 3D junction with the West Napa Fault (WNF). UAVSAR data (Donnellan *et al.*, 2014) and relocated aftershocks (Hardebeck and Shelly, 2014) suggest that the main WNF experienced triggered slip and afterslip along a length of roughly 20 km. Therefore, it is possible that the 2014 rupture took place along a largely unrecognized westerly strand of the WNF which is also steeply west-dipping based on focal mechanisms of the mainshock and connection of the surface rupture to the relocated hypocenter. Focal solutions by UC Berkeley show right-lateral motion along a plane having the similar strike and rake (Brocher *et al.*, 2015).

The 2014 mainshock produced ~14 km of surface rupture along the WNF, with maximum surface displacements of 40-45 cm (e.g., Hudnut *et al*., 2014). The mapped surface rupture consisted primarily of a zone of right-lateral fractures from less than one meter to more than tens of meters wide. Although the surface rupture varied along the rupture length,

it was usually observed as a zone of en echelon left-stepping fractures (Brocher *et al*., 2014). Combined UAVSAR and GPS estimates of fault slip for the *Mw* 6.0 South Napa Earthquake, show slip on a single fault at the south end of the rupture near the epicenter of the event, but the rupture branches out into multiple faults further north near the Napa area (Donnellan *et al.*, 2014). The eastern two sub-parallel faults break the surface, while three faults to the west are buried at depths ranging from 2-6 km with deeper depths to the north and west. The geodetic moment release is equivalent to a *M*6.1 event. Additional ruptures are observed in the interferogram, but the inversions suggest that they represent superficial slip that does not contribute to the overall moment release. The rupture propagated mostly to the north and up-dip, directing the strongest shaking toward the City of Napa, where peak ground accelerations between 45% *g* and 61% *g* and MMI intensities of VII-VIII were reported (Boatwright *et al*., 2014). The highest peak ground acceleration (1*g*) in the region was recorded near the town of Crockett, at the Carquinez Bridge probably due to local site conditions (Boatwright *et al*, 2015; Celebi *et al*., 2015) or to an unusual path effect. However, there are strong positive residuals in strong motion records at stations to the south of the earthquake, suggesting stronger shaking in the along-strike direction of faults in the region (Baltay and Boatwright, 2015). In particular, these positive residuals may align with the Quaternary-active Franklin or Southhampton faults. Such positive residuals are consistent with a fault-zone waveguide effect along these faults.

Intense fracturing during earthquakes, brecciation, liquid-saturation, and possibly high pore-fluid pressure near the fault are thought to create low-velocity zones that can efficiently trap seismic waves. Fault-zone trapped waves (FZTWs), also referred to as guided waves, arise from coherent multiple reflections and corresponding high reflection coefficients at the boundaries between the low-velocity fault zone and the surrounding higher velocity rocks (Li *et al*., 1990; Li and Leary, 1990). FZTWs have been used to characterize the magnitude of fault rock damage and multiple ruptures along active faults and post-earthquake healing process in our study of rupture zones of the 1994 *M*9.4 Landers and 1999 *M*7.1 Hector Mine earthquakes (Li *et al*., 1994, 1998, 2000, 2003, 2014; Vidale and Li, 2003; Cochran et al., 2009), and the rupture zone of the 2004 *M*6 Parkfield earthquake on the San Andreas Fault in California (Li *et al*., 1997, 2004, 2006; Li and Malin, 2008). In this paper, we use FZTWs generated by aftershocks and explosions to characterize the subsurface structure of fault rock damage along the West Napa Fault Zone (WNFZ) that ruptured in the *M*6 South Napa earthquake occurring southwest of the City of Napa, California on 24 August, 2014 as well as the adjacent faults (Fig. 1). The WNF zone is located east of the Hayward-Rodgers Creek Fault (HRCF) system and approximately 13 km west of the Concord-Green Valley Fault

(CGVF) system. Both fault systems have generated historic damaging earthquakes, including the 31 March 1898 *M*5.8-6.4 Mare Island earthquake (Hough, 2014) and the 3 September 2000 *M*5.2 Yountville earthquake (Langenheim *et a*l., 2006).

THE AFTERSHOCK DATA AND WAVEFORM ANALYSES

Four days after the *M*6 South Napa earthquake, the U.S. Geological Survey (USGS) installed three seismic arrays Array 1, Array 2 and Array 3 (A1, A2 and A3) consisting of a total of 50 short-period (4.5 Hz) seismic stations across the West Napa Fault (WNF) and adjacent faults for ~2 weeks (Catchings *et al*., 2014). 1.9-km-long A1 and A2 were deployed perpendicularly across the West Napa Fault Zone (WNFZ), at locations near the ends of the northern and southern surface ruptures, respectively (Fig. 1). A3 was deployed across the intersection of the Franklin and Southhampton faults, which could be southward continuations of the WNFZ. The station spacing along each array was 100 m, with vertical, fault parallel, and fault perpendicular velocity sensors (4.5 Hz) at each station. The seismometers recorded in continuous mode at 100 samples per second and were synchronized by internal GPS clocks before and after deployment. A1 consisted of 20 stations, referred to here as stations A1-01 to A1-20. A2 consisted of 20 stations. A3 consisted of 10 stations A3-1 to A3-10. Seven REFTEK-130 three-channel seismographs (R1 to R7) with 2Hz L22 sensors were deployed around the WNFZ. R1 to R4 were located close to the surface rupture and the south part of the WNF (Fig. 1).

Approximately 180 aftershocks and local earthquakes were recorded at the three seismic arrays and REFTEK stations between August 28 and September 9 (Julian dates 240 to 252) of 2014. We examined the waveform data from all the recorded events and selected 55 aftershocks from which seismograms show appropriate signal-to-noise ratio. Figure 1b shows locations of the 55 aftershocks, among which 41 aftershocks generated FZTWs. We identify the FZTWs on the basis of extended coda waves with large amplitudes that follow the S-arrival on seismograms recorded at stations within a fault zone. Generally, the coda length of the coherent guided waves increases with increasing hypocentral distance between the earthquake source and the recording site, while the difference between the P- and S-arrivals also increases with increasing hypocentral distances. Empirical studies have shown that the ratio of the post-S coda time to the time difference between the P- and S-arrivals is approximately higher than 1.2 for prominent FZTWs (Li *et al*., 2014). In this study, we use the ratio of post-S coda time to S-P arrival time difference $(t_C–t_S)/(t_S–t_P)$ higher than ~1.2, to indicate prominent FZTWs well generated and observed for aftershocks that occurred within

or close to the low-velocity fault zone. t_p and t_s are the P- and S-arrival times; t_c is the post-S coda time in which the amplitudes of FZTWs are above twice those of the background signals.

Post-S Coda Durations of FZTWs Increasing with Focal Depth

For example, we analyzed FZTWs generated by aftershocks E14, E7, E26, and E5 (see Fig. 1b), which occurred along the northern projection of the 2014 surface rupture at

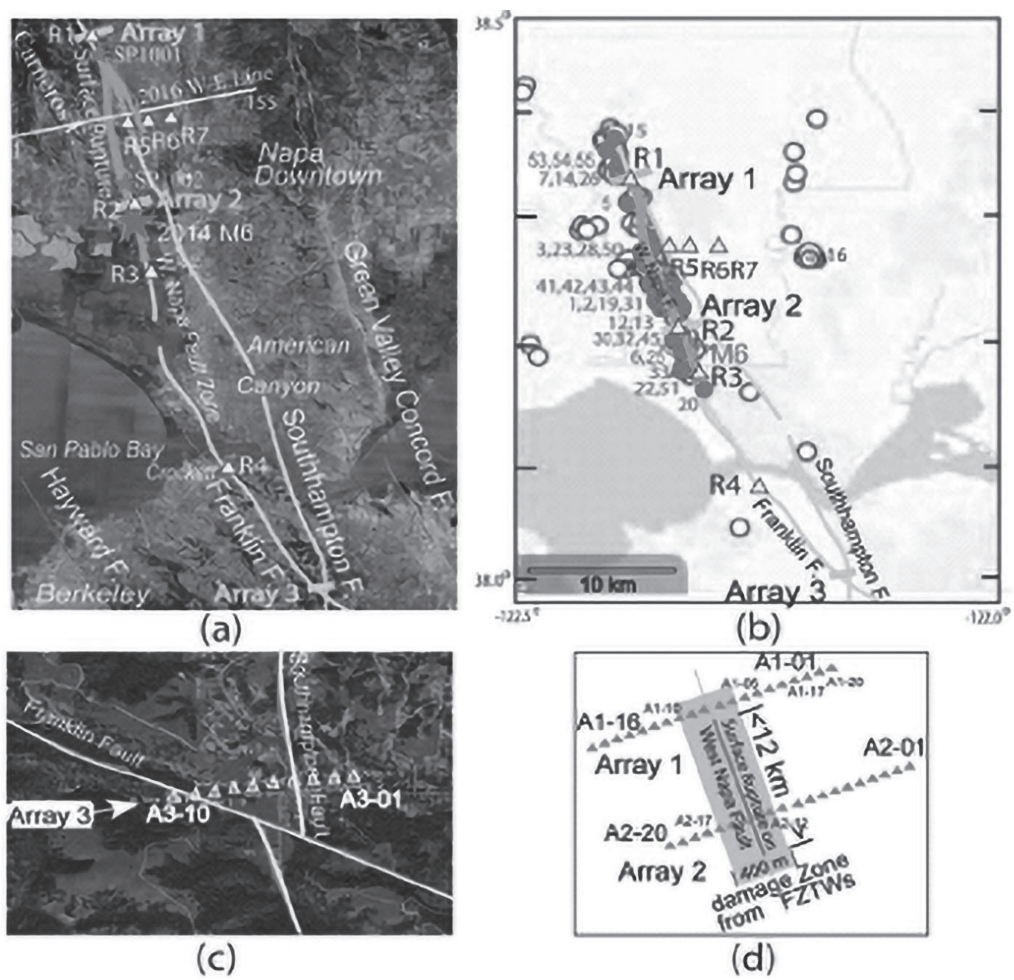

Figure 1. (a) Map shows the 2014 M6 South Napa earthquake (star). aftershocks (dots), surface ruptures (thick red line). three seismic arrays A1, A2 and A3 (blue bars). REFTEK seismographs RI-R7 (triangles), and faultsbrawn lines. (b) Map shows aftershocks (circles) recorded on the arrays between 08/28 and 9/9 of 2015, including 41 on-fault aftershocks (solid circles with numbers) generating FZTWs. The thick pink line denotes the 2014 surface rupture zone. (c) Map shows locations of 10 stations (triangles) of A3 that crosses the Franklin and South Hampton faults. (d) Schematic diagram showing station locations (triangles) of Al and A2 across the northern and southem parts of the WNF rupture zone. The red line denotes the 14-km-long surface rupture of the WNF within a 400-m-wide rupture zone (brawn band) determined by FZTWs.

depths increasing from 2.8 km to 6.6 km (Fig. 2). Their epicentral distances to the center of A1 range from 1 to 3 km. The raypaths between these aftershocks and A1 are sub-vertical. FZTWs with relatively large amplitudes and long post-S coda durations are prominent at five stations located within the rupture zone. At array A1, post-S coda durations of FZTWs increase from 0.8 s to 1.6 s as aftershock hypocenters increase from 2.8 km to 6.6 km. The $(t_C–t_S)/(t_S–t_P)$ ratio for on-fault aftershocks range from 1.3 to 1.6 with the maximum ratio for the shallowest event E14 at 2.8-km depth. The FZTWs recorded at arrays A1 and A2 for these

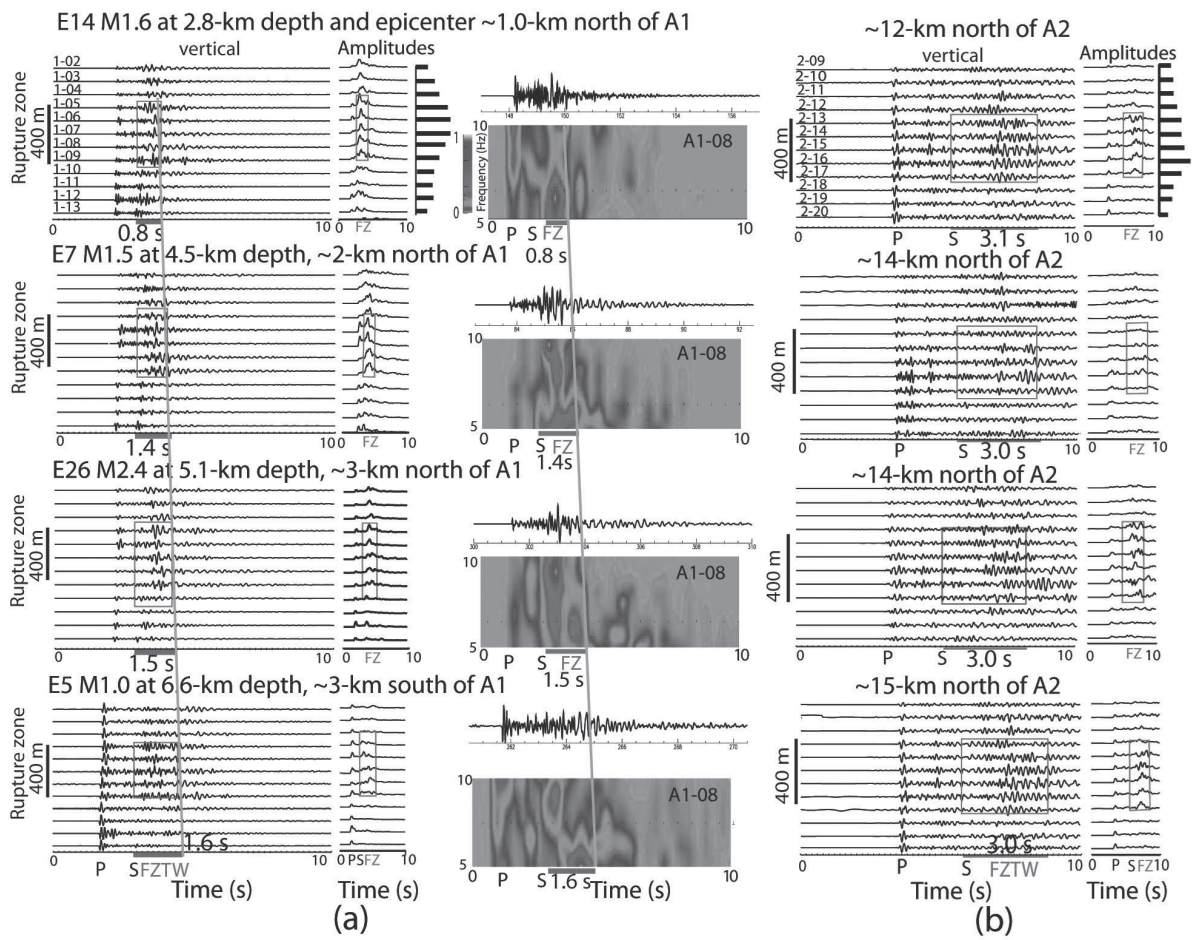

Figure 2. (a) Seismograms and amplitudes registered at 12 stations (A1-01 to A1-16) of A1 for four on-fault aftershocks E14, E7, E26, and E5. Histogram shows maximum amplitudes of post-S coda in 3 s windows for each seismogram recorded at A1. Spectral amplitudes of seismograms at station A1-08 of A1 within the rupture zone are computed and normalized (0–1). FZTWs (in boxes) are observed at stations A1-05 to A1-09 of A1 and stations A2-13 to A2-17 of A2. Post-S coda durations of FZTWs at A1 increase from 0.8 to 1.6 s as aftershock depths increase from 2.8 to 6.6 km (the move-out denoted by the slope of a gray line). (b) Same plot as shown in (a) but for the data recorded at 12 stations (A2-09 to A2-20) of A2 for these aftershocks. Post-S coda durations of FZTWs registered at A2 are 3.0-3.1 s.

aftershocks suggest that a remarkable low-velocity damage zone along the WNFZ likely extends further northward from the surface rupture of the 2014 M6 South Napa earthquake to depths of at least 5-6 km.

In another example, we evaluated FZTWs generated by three aftershocks E31, E2 and E32 (see Fig. 1.1) occurring at depths of 4.8, 7.7, and 9.3 km depths between A1 and A2, and recorded at the two arrays (Fig. 3). Prominent FZTWs are observed at stations within

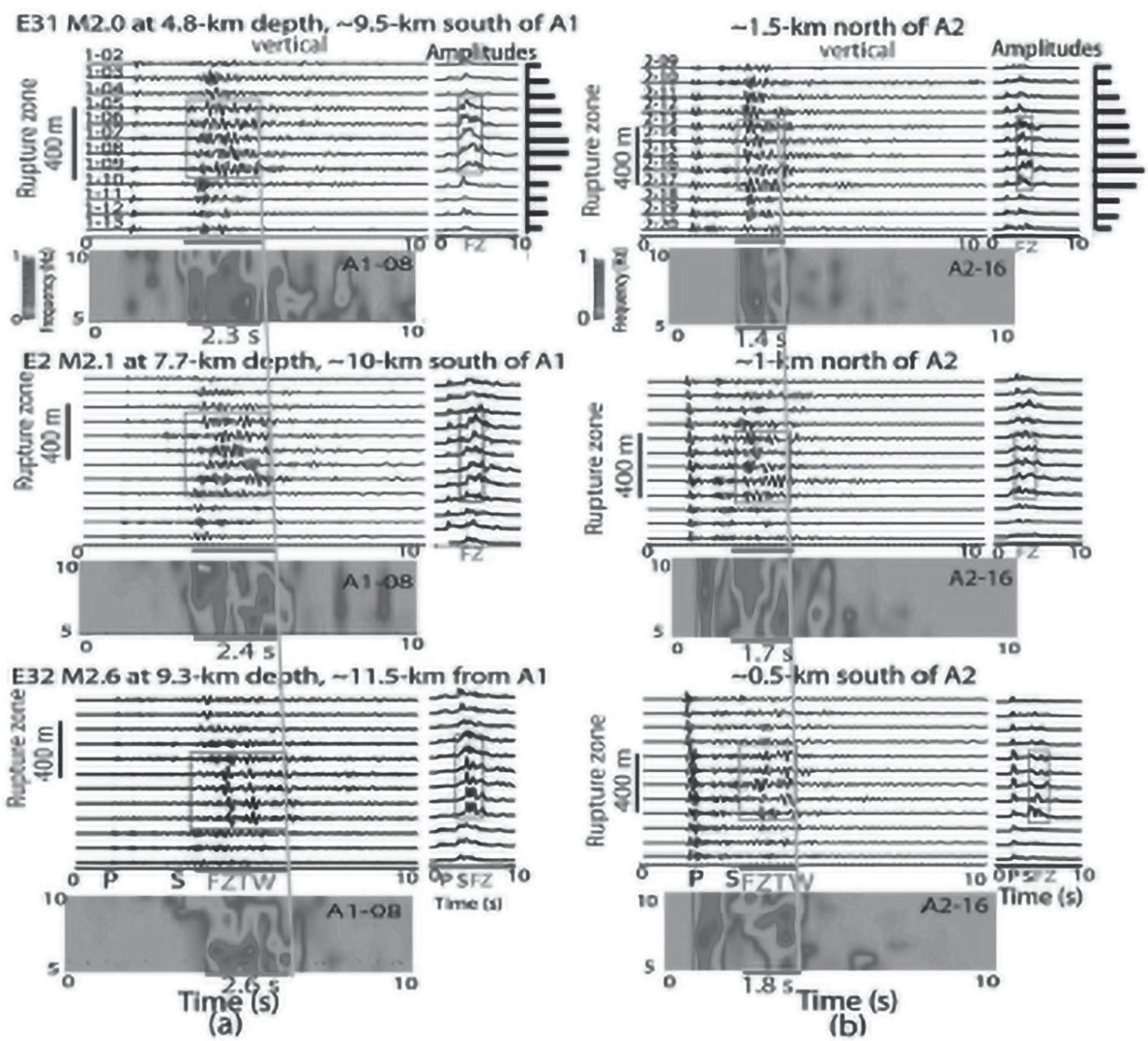

Figure 3. (a)Seismograms, amplitudes, andnormalized spectral amplitudes registered at A1 from three on-fault aftershocks E31. E2 and E32 at 4.8. 7.7 and 9.3 km depth. Post-S coda durations of FZTWs for stations of Al within the rupture zone are 2.3-2.6 s for these aftershocks. (b) Same as in (a), but for A2. Prominent FZTWs (in boxes) seen at stations A1-5 to A1-9 of A1 and stations A2-12 to A2-17 of A2. Histograms show the maximum amplitude of post-S coda at each array station. The post-S coda durations of FZTWs at A2 increase from 1.4 s to 1.7 s (denoted by a grey line) as aftershock depths increase from 4.8-km to 7.7 km. There is only a slight increase (0.1s)for focal depths between 7.7 km and 9.3 km. FZTWs are not shown at away-tault stations.

and near the 2014 surface rupture zone for each aftershock. The post-S coda durations of FZTWs (measured at A2) increase from 1.4 s to 1.7 s as their focal depths increase from 4.8 km to 7.7 km) but the post-S coda durations only slightly increase from 1.7 s to 1.8 s for aftershocks with focal depths between 7.7 km and 9.3 km, suggesting that a significant low-velocity waveguide likely extends to approximately 7.7 km depth at A2. Post-S coda durations (2.3 to 2.6 s) of FZTWs recorded A1 for the same aftershocks. The $(t_C–t_S)/(t_S–t_P)$ ratio for aftershocks E31 and E2 range from 1.2 to 1.4, suggesting a remarkable low-velocity waveguide along the rupture zone to depth ~5-7 km between A1 and A2, but the ratio for the deep aftershock E32 is 1.1, indicative of weak waveguide effect below ~7 km.

Post-S Coda Durations of FZTWs Increasing with Epicentral Distance

To examine the continuity of the rupture zone along the WNFZ at seismogenic depths, Figure 4 shows FZTWs recorded at A1, A2, and A3 for an on-fault aftershock E51 (see Fig. 1b) located ~6 km south of A2 at ~5 km depth. FZTWs from E51 are prominent at stations of A1 and A2 located within the rupture zone. Post-S coda durations of the FZTWs average ~2.8 s at A1 and ~1.7 s at A2. In contrast, post-S coda durations are much shorter at stations located outside of the rupture zone. At A3, we observe FZTWs with 3.8 s of post-S coda durations at stations A3-02 and A3-03 located near the Southhampton Fault (F1), and at stations A3-09 and A3-10 located near the Franklin Fault (F2). The FZTWs traveling ~28-km distance from aftershock E51 to array A3 show 3.8 s post-S coda duration while the FZTWs traveling ~18-km distance from the same aftershock to A1 show 2.8 s post-S coda duration, suggesting that either (a) rocks within the fault zone to the north from E51 along the WNFZ have been more severely damaged than those along the fault zone to south from E51 and A3 along the Franklin Fault, or (b) The deeper travel path to A3 only samples the deeper (and higher velocity) part of the waveguide. The $(t_C–t_S)/(t_S–t_P)$ ratios for FZTWs are 1.2-1.3 at A1 and A2 along the WNF but ~0.8 for A3, showing less trapping efficiency of the waveguides south of E51 along the FF. In general, these ratios are smaller than those for FZTWs generated by aftershocks occurring within the central part of the rupture zone between A1 and A2 (see Figs. 1.3 to 1.8), indicating the low-velocity waveguide south of A2 has weaker trapping efficiency than that along the central part of the rupture zone at seismogenic depths. Alternatively, the smaller ratios may infer weaker excitation of FZTWs because they originate lower than or at the bottom of the rupture zone.

FZTWs Observed at Three Cross-Fault Arrays and Along-Fault REFTEK Stations

We analyzed waveform data recorded at REFTEK-130 seismographs (R1-R7) deployed

along the WNFZ and the Franklin Fault. For example, Figure 5 shows prominent FZTWs recorded at four stations R1 to R4 located close to the faults, but not at station R7 located ~2 km away from the WNF for three on-fault aftershocks E26, E13 and E20 occurring at depths of 5 km, 9.6 km and 8.7 km, respectively.

We measured post-S coda durations of FZTWs increasing from 1.5 s to 5 s as the hypocentral distances between aftershock E26 and four on-fault stations R1–R4 increase

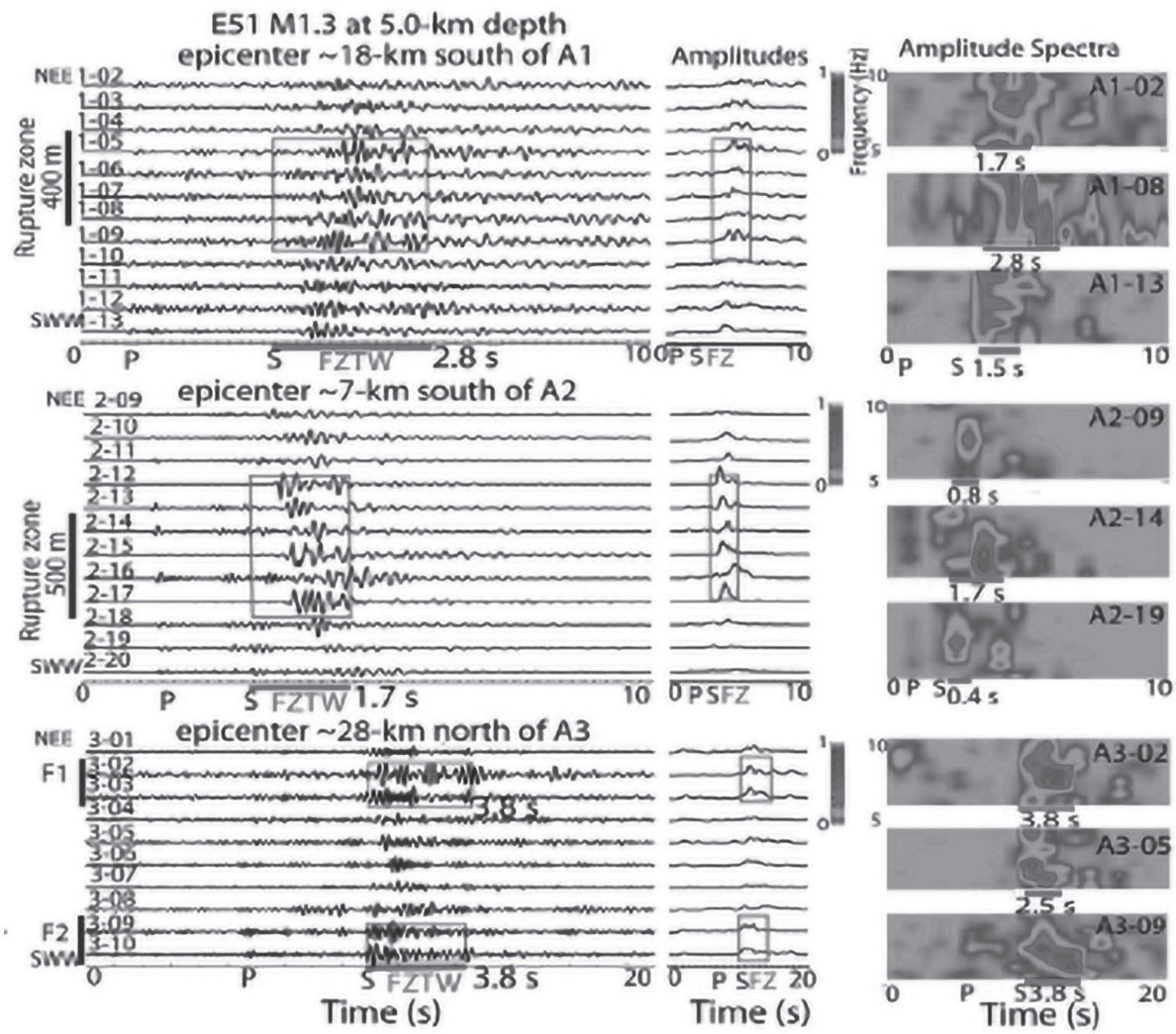

Figure 4. Vertical-component seismograms, amplitudes, and normalized spectral amplitudes at arrays A1, A2 and A3 for an on-fault aftershock E51. FZTWs (in boxes) are observed at stations A1-05 to A1-09 of A1, stations A2-12 to A2-17 of A2, and stations A3-02. A3-03. A3-09, and A3-10 of A3. Post-S coda durations of FZTWs average 2.8 s at A1 and 1.7 s at A2. Spectral amplitudes of seismograms show FZTWs with ~2.8 s and~1.7 s coda durations at stations A1-08 and A2-14. Much shorter durations are observed at stations A1-02. A1-14, A2-09. and A2-19 outside of the rupture zone. FZTWs with 3.8 s duration appear at stations A3-02 and A3-03 near the FF (denoted by F1). and at stations A3-09 and A3-10 near the Southhampton Fault (F2).

from ~6 km to ~36 km. Similarly, we measured post-S coda durations of FZTWs increasing from 1.8 s to 3.9 s as the hypocentral distances between aftershock E13 and REFTEK stations R1–R4 increase from ~10 km to ~23 km. We measured post-S coda durations of FZTWs increasing from 1.8 s to 3.3 s as the hypocentral distances between aftershock E20

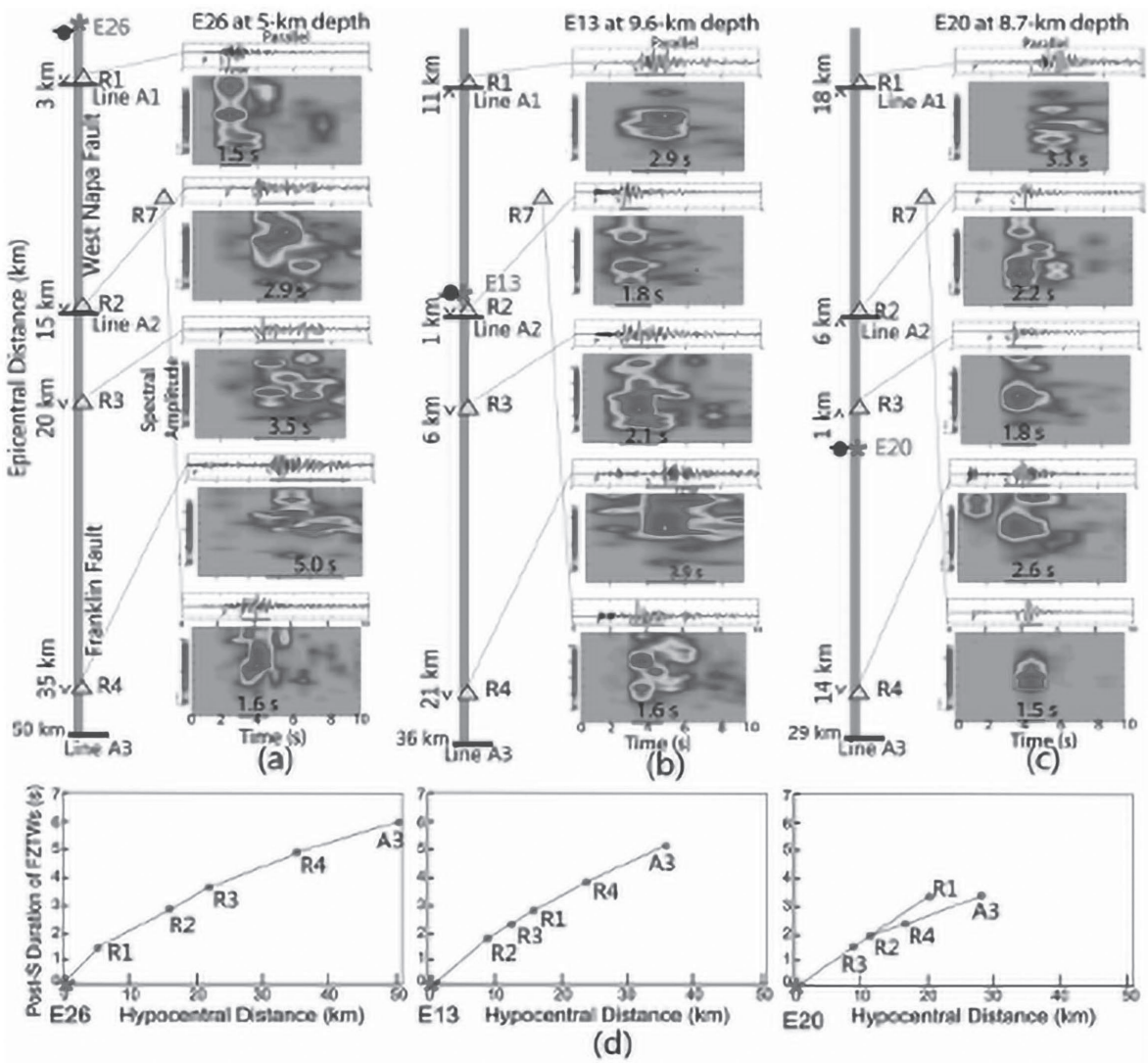

Figure 5. Seismograms and normalized spectral amplitudes at four on-fault R1-R4 and one off-fault seismometers R7 (triangles)deployed along the WNF and FF (gray lines) for aftershocks (a)E26, (b) E13 and (c) E20 (stars). Epicentral distances between aftershocks and recording stations are plotted in the schematic diagrams. The post-S durations of FZTWs are marked by horizontal red bars with measured duration time. (d) Post-S durations of FZTWs (red dots)measured at four on-fault stations to R4 along with the WNFZ and the FF. and the cross-fault seismic array A3 for three on-fault aftershocks E26, E13 and E20 versus hypocentral distances between three aftershocks and stations. showing that the post-S coda durations of FZTWs increase with increasing travel distances, with larger increasing rate along the WNFZ than along the Franklin Fault.

and stations R1-R4 increase from 9 km to 20 km. In contrast, the post-S coda durations at station R7 out of the WNFZ is 1.5-1.6 s. The $(t_C–t_S)/(t_S–t_P)$ ratios for these FZTWs at R1–R4 range from 1.0 to1.6 with the larger ratio for FZTWs recorded at R1 and R2 located within the WNFZ rupture zone and smaller ratio at R4 close to the Franklin Fault, indicating the stronger waveguide trapping effect along the WNFZ rupture zone than the FF. Moreover, we measured FZTWs recorded at four REFTEK stations for 30 on-fault aftershocks (refer to Li et al., 2016). The measurements of FZTWs at R1 and R2 are consistent with those at co-located stations of arrays A1 and A2 within the rupture zone for the same aftershocks. We notice the P-type FZTWs with the post-P coda durations of 1.2-1.5 s at stations A2-13 to A2-16 of array A2 located within the WNFZ for shallow aftershocks E14 and E15.

SUBSURFACE DAMAGE STRUCTURE INFERRED FROM FZTWS

We have observed significant FZTWs generated by 41 Napa aftershocks and recorded on three cross-fault seismic arrays (A1, A2, and A3) and four REFTEK seismographs (R1 to R4) deployed along the WNFZ and the Franklin Fault. The $(t_C–t_S)/(t_S–t_P)$ ratios for FZTWs are equal to or larger than 1.2 on most seismograms recorded at A1, A2, and R1 to R3 for sources and receivers both located within or along the rupture zone of the 24 August 2014 *M*6 South Napa earthquake. However, the $(t_C–t_S)/(t_S–t_P)$ ratios for FZTWs on seismograms recorded at R4 and A3 located along the south WNF and Franklin fault (FF) that did not rupture in the 2014 *M*6 earthquake are ~0.8-1.0 s, indicating a waveguide having moderate trapping efficiency along the south WNFZ and the FF. In contrast, the $(t_C–t_S)/(t_S–t_P)$ ratios on seismograms recorded at all seismic stations for aftershocks occurring far away from the WNFZ and FF are less than 0.5, indicating no significant FZTWs were excited by these off-fault events.

Figure 6a shows measured post-S coda durations of FZTWs recorded at on-fault stations of arrays A1, A2, A3 and REFTEK stations R1 to R4 for the 41 aftershocks occurring within the WNFZ *versus* their hypocentral distances between aftershocks and seismic stations (refer to Li *et al*., 2016 for details). The measurements show that post-S coda durations of FZTWs recorded at A1, A2, R1, R2 and R3, which were located on or close to the surface rupture of the 2014 *M*6 South Napa earthquake, increase from ~1.0 s to ~4.0 s as hypocentral distances of these aftershocks increase from ~3-km to ~21-km. The longer coda durations of thee FZTWs result from their greater travel distances within the low-velocity waveguide. Although an ~14-km-long surface rupture was observed, the subsurface rupture likely extends beyond the northernmost and southernmost ends of the surface rupture, consistent

with aftershock alignments (Hardebeck and Shelly, 2014) and afterslip observations (Hudnut *et al*., 2014). The post-S coda durations of FZTWs recorded at R4 and A3, which were deployed at the south WNF and FF, increase from ~2.5 s to ~6.0 s as hypocentral distances of these aftershocks increase from ~20-km to ~50-km, but show a smaller increasing rate than that for A1, A2, R1, R2, and R3. The post-S coda durations of FZTWs generated by these aftershocks suggest that the low-velocity waveguide along the WNFZ extends continuously to the FF, but the waveguide trapping efficiency of the south WNFZ and FF is weaker than that along the WNFZ with surface rupture during the 2014 *M*6 South Napa earthquake. Although there is an amount of scatter in the data in Figure 6a, the data are in general consistent with a continuous low-velocity waveguide at seismogenic depths along with the 2014 rupture zone. The aftershocks with shorter hypocentral distances (either at shallower depths or nearer to seismic arrays) show the greatest $(t_C–t_S)/(t_S–t_P)$ ratio for guided waves, implying strongest trapping efficiency of the waveguide at shallow depths between A1 and A2. We note that for all aftershocks with similar hypocentral distances, the two shallowest aftershocks E14 and E42 occurred at 2.8 km and 4.25 km depth, show the highest $(t_C–t_S)/(t_S–t_P)$ ratios of 1.4-1.6, implying a more prominent low-velocity waveguide at the shallow depths.

FZTWs recorded at A1, A2, A3, R1, R2, R3 and R4 show that the low-velocity waveguide along the WNFZ extends further southward to at least A3 but possibly with a more moderate fault zone velocity reduction. The existence of a relatively low-velocity waveguide to the south of the 2014 *M*6 South Napa earthquake is also consistent with the ground motion observations by Baltay and Boatwright (2015).

Empirical studies have shown that the generation of FZTWs is strongly dependent on the source location with respect to the low-velocity waveguide (e.g., Li and Leary, 1990; Li and Vidale, 1996), whereby earthquakes located within the waveguide generate stronger FZTWs than earthquakes located out of the waveguide. Thus, the relative amplitudes of the FZTWs allow us to delineate the geometry of subsurface rupture zone. Figures 6b and 6c show the locations of 55 aftershocks in a 3-D volume, including 41 aftershocks with prominent FZTWs recorded at A1, A2, R1, R2 and R3 that have $(t_C–t_S)/(t_S–t_P)$ ratios greater than 1.1 and 14 aftershocks without prominent FZTWs and with $(t_C–t_S)/(t_S–t_P)$ ratios less than 0.7. Hypocenters of aftershocks that generated prominent FZTWs delineate the NNW-SSE-striking rupture zone that dips to the west at > 80°. The most recently damage zone at depth is several kilometers longer than the ~14-km-long 2014 surface rupture and likely extends to at least ~7-8-km depth near the mainshock hypocenter but only ~5-6-km deep in the northern portion of rupture zone.

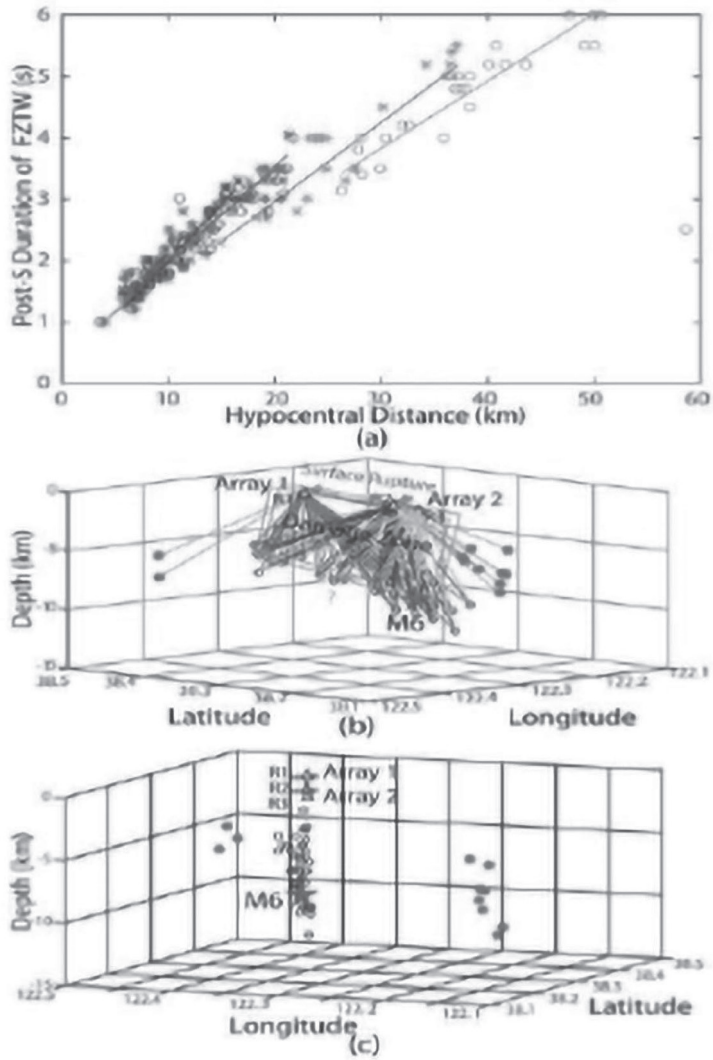

Figure 6. (a) Measured post-S coda durations of FZTWs recorded at arrays Al, A2 and A3 (red. blue and green circles), and stations R1, R2 and R3 (red, blue and pink stars) for 41 aftershocks at various depths within the WNFZ rupture zone. Post-S coda durations of FZTWs are plotted versus hypocentral distances between the aftershocks and recording stations, showing the more rapid increase of durations with distance for aftershocks at distances <20-km due to the greater velocity reduction and the greater waveguide effect within the shallower portion of the central part of rupture zone. The lines are the least-squares fit to the measurements. (b) 3D volume showing hypocenters of 55 aftershocks recorded at arrays A1 and A2 (green bars), and stations R1, R2 and R3 (yellow triangles)deployed across and along the WNFZ (thick red line). Thin lines are ray paths between Al (red), A2 (blue), R1 (red), R2 (blue), R3 (pink) and the aftershocks (open circles) that generated FZTWs. Green lines are ray paths between recording stations and aftershocks (stars) without clear FZTWs. The damage zone of the WNFZ (bounded by two rectangular planes) likely extends to ~5-6 km depth beneath A1 and~7-8 km depth beneath A2. (c) 3D volume viewed along the WNF. Locations of aftershocks (open circles) generating FZTWs delineate the nearly vertical rupture zone.

3-D FINITE-DIFFERENCE SIMULATIONS OF FZTWS GENERATED BY AFTERSHOCKS

We developed models of the WNFZ subsurface rupture zone on the basis of the hypocenters of aftershocks that generated prominent FZTWs and the measurements of FZTW coda durations and waveguide trapping efficiency (Fig. 6a). With layer depths, fault dip, and velocities of the surrounding basement rocks based on an existing velocity model for the region (Fig. 7a) from Stidham *et al*. (1999) and Brocher *et al*. (2005), we constructed a velocity model (see Fig. 7b and Table 1) for the WNFZ and Franklin Fault. Velocities and attenuation (Q) in our model are depth dependent because increasing pressure with increasing depth influences the density and the bulk modulus of rocks as well as the healing rates of damaged rocks (Byerlee, Rice, 1992; Sibson, 1996; Marone, 1998). The depth-dependent pressure increase may also influence the development of fault gouge due to normal stress and rock strength (Scholz, 1990). For these reasons, we used varying velocities with depth in our model. Our 3-D model includes a 20-km-long 400-m-wide rupture zone within which velocities are reduced by 25–50% relative to wall-rock velocities beneath the West Napa Fault where A1, A2, R1, R2 and R3 were located, and a 30-km-long fault zone within which velocities are reduced by 20–35% beneath the Franklin Fault where R4 and A3 were located (Fig. 7b). We infer a maximum velocity reduction within a 200-m-wide damaged fault core at shallow depths (see model parameters in Table 1). The depth of the low-velocity rupture zone increases from 5-km beneath A1 to 8-km beneath A2 and A3. The damage zone diminishes below those depths. To compute synthetic seismograms, we used a 3-D finite-difference code

Table 1. Model Parameters for West Napa Rupture Zone and Franklin Fault

Model parameters WNF (FF)	Layer 1	Layer 2	Layer 3	Layer 4	Layer 5
Depth of the layer bottom, km	1.0	3.0	5.0	8.0	10.0
Waveguide width, m, Damage zone/core	400/200	400/200	300/150	200/100	
Waveguide *S* velocity, km/s	1.0/0.75 (1.3/1.0)	1.3/1.0 (1.7/1.3)	1.8/1.25 (2.3/1.6)	2.0/1.5 (2.6/2.0)	
Waveguide *P* velocity, km/s	2.0/1.5 (2.6/2.0)	2.6/2.0 (3.4/2.6)	3.5/2.5 (4.5/3.2)	4.0/3.0 (5.2/4.0)	
Waveguide *Q*-value	20	30	50	60	
Wall-rock *S* velocity, km/s	1.5	2.0	2.5	3.0	3.5
Wall-rock *P* velocity, km/s	3.0	4.0	5.0	6.0	6.5
Wall-rock *Q*-value	50	80	100	150/200	

that fits waveforms of FZTWs recorded at A1 and A2. The finite-difference computer code is second order in time and fourth order in space (Graves, 1996; Vidale *et al*., 1985), and it propagates the complete wave-field through an elastic media with a free surface boundary and spatially variable anelastic damping (an approximate Q).

The low-velocity waveguide, composed of a 200-m-wide fault core zone of maximum velocity reduction sandwiched within a 400-m-wide damage jacket with milder velocity reduction, is embedded in the higher-velocity surrounding rocks with a free surface. The north portion of the waveguide with greater velocity reductions along the WNF rupture zone is 20-km long while the southern portion of the waveguide with more moderate velocity reductions along the FF is 30-km long (Table 1). The seismic array was placed across the waveguide along the fault strike. The seismic waves were derived from a double-couple source (according to the mainshock focal mechanisms) with radiation patterns. When the grid spacing is 50-m or 25-m, the maximum frequency of synthetic waveforms is 3-Hz or 6-Hz.

We simulated the FZTWs recorded at A1, A2 and A3 as well as R4 for aftershocks that occurred at various depths and epicentral distances via a trial-and-error, forward-modeling procedure to obtain the well-fit model parameters. For example, Figure 7c shows synthetic waveforms, using the inferred velocity model (Fig. 7b), agreeable with seismograms recorded at seismic array A1 for three on-fault aftershocks (E8, E31 and E2 in Fig. 1b). We use a double-couple source within the fault zone. FZTWs with large amplitudes and ~2.2-2.4 s of post-S coda durations are observed at five near-fault stations A1-05 to A1-09 of A1 within the rupture zone. The consistency of the observed and computed seismograms suggests that the 2014 rupture zone consists of a remarkable low-velocity waveguide formed by severely damaged rocks. Seismic energy is trapped and best propagated with large amplitudes along the waveguide for frequencies between 1 and 6 Hz. We compare synthetic waveforms (Fig. 7d) developed from our velocity model (Fig. 7b) with seismograms recorded at array A2 for three on-fault aftershocks E33, E22 and E26. The post-S-wave coda durations of synthetic FZTWs are 2.2-3 s at five stations A2-13 to A2-17 of A2 located within the rupture zone. Figure 7e shows synthetic FZTWs with 3.5-5.2 s post-S coda durations at stations A3-09 and A3-10 of array A3 near the FF, consistent with the observed data recorded at A3 for three on-fault aftershocks E22, E12 and E18. Figure 7f shows synthetic and observed FZTWs with 3.3-4.5 s post-S coda durations at REFTEK station R4 for these three aftershocks. In general, the coda durations of FZTWs increase as their travel distances within the waveguide increase, however, the increasing rate for FZTWs traveling along the WNF rupture zone within which rocks were severely damaged in the 2014 *M*6 mainshock is higher than along

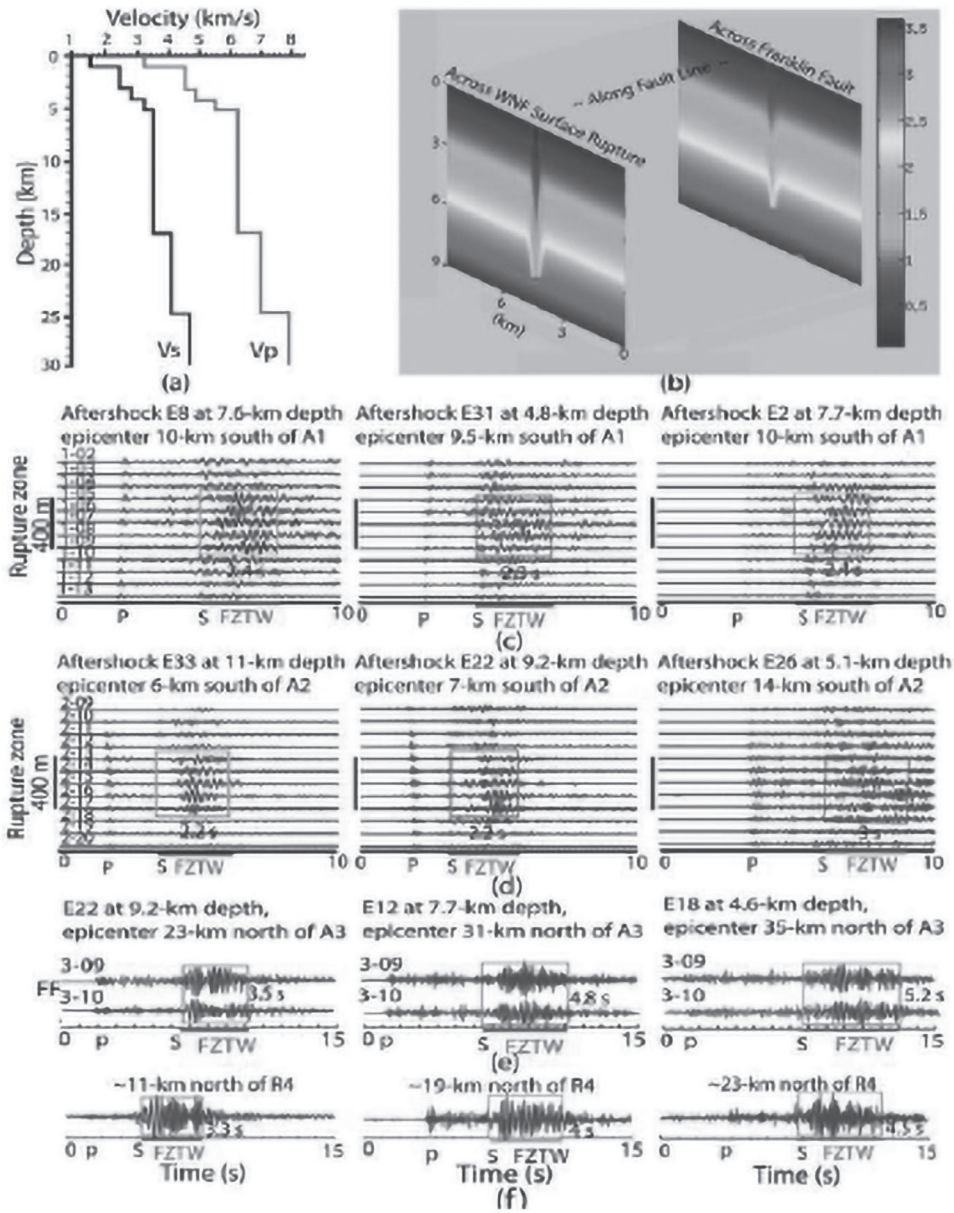

Figure 7. (a) 1-D P-and S-velocities for the Napa region from Brocher *et al*. (2005) used for wall-rock velocities in ourmodel. (b) A 2-D slice of our 3-D velocity model of the WNFZ at A2. The 400-m-wide rupture zone is exposed at the surface. Velocities within the rupture zone along the WNFZ are reduced by 40-50% from wall-rock velocities. but reduced by 30-35% along the FF. (c) 3-D finite-difference synthetic seismograms (blue lines) using the model in (b) with observed seismograms (red lines) at seismic array A1 for three aftershocks (E8, E31 and E2) located at depths of 7.6. 4.8 and 7.7 km, and ~10-km south of Al. Seismograms were <8 Hz filtered. (d) Synthetic and observed seismograms at array A2 for aftershocks E33, E22 and E26 at depths of 11, 9.2 and 5.1 km, and 6. 7 and 14 km south of A2. (e) Synthetic and observed seismograms at stations A3-09 and A3-10 of array A3 across the Franklin Fault for aftershocks E22, E12 and E18 at depths of 9.2, 7.7 and 4.6 km, and 23. 31 and 35 km north of array A3. (f) Synthetic and observed seismograms at REFTEK station R4 located at the south WNF for aftershocks E22. E12 and E18 located at 11. 19 and 23 km north of R4, showing FZTWs (in green boxes) recorded at stations within the rupture zone.

the south WNF and the FF that were unbroken at the surface in the 2014 *M*6 earthquake. We note that the FZTW coda durations (2.2 s) for deep aftershocks E22 and E33 at 9-11 km depths is shorter than those (2.3-2.4 s) from aftershocks E2, E8 and E31 at depths of 4.8-7.7 km, although the hypocentral distances of the deep events are greater than those of the shallower events. We suggest the shorter coda for the deeper event results from a diminished low-velocity waveguide below ~7-8 km depth.

The model parameters given in Table 1 are not uniquely constrained by this forward modeling because there are trade-offs among them. However, our inferred velocity model resulted from 3-D finite-difference simulations of FZTWs provides a first-order estimate of the overall structure of the WNFZ and Franklin Fault in the subsurface.

THE FZTWS GENERATED BY EXPLOSIONS

In September of 2016, an active seismic experiment with shots conducted in Napa Valley by the USGS (Catchings *et al*., 2016). A 15.4-km-long seismic line (called 2016 W-E Line in Fig. 8) consisting of 155 stations with vertical and horizontal L28 4.5-Hz sensors was deployed across the West Napa Fault Zone (WNFN) and adjacent faults. The station spacing is 100 m. The W-E seismic line nearly perpendicularly crossed multiple surface ruptures along at least three fault strands of the WNFZ. 36 shots were detonated along the two seismic lines, and two explosions (called SP1001 and SP1002 in Fig. 8) were detonated within the west rupture zone along the main trace of the WNFN at ~3.5-km north and ~5-km south of the 2016 W-E Line, respectively. Small amount of explosives set off at the bottom of 7-10-m-deep drill holes allows seismic energy generated by tiny artificial sources to eliminate the near-surface soil affect and travel through the subsurface geological layers efficiently. Because the length of the 2016 W-E Line is much longer than the cross-fault seismic arrays in the 2014 experiment, the FZTWs recorded in the 2016 experiment will provide more information on the rupture branching during the 2014 *M*w 6.0 earthquake and allow us to measure the width of multiple rupture zones more accurately.

In the same way, we use the ratio of post-S coda time to S-P arrival time difference $(t_C–t_S)/(t_S–t_P)$, to indicate prominent FZTWs well generated and observed for explosions detonated within the low-velocity rupture zone when the ratio is higher than 1.2. Figure 9 shows band-pass (2-6 Hz) filtered seismograms recorded at 2016 W-E Line for explosion SP1001. The FZTWs with large amplitudes and long durations (2.0-2.5 s) after S-wave at stations located within the main and branch rupture zones exposing at the surface along multiple strands of the WNFZ associated with the 2014 *M*6 earthquake. The time differences

between the P- and S-arrivals are approximately 1.5 s. Thus, $(t_C–t_S)/(t_S–t_P)$ ratios for these FZTWs generated by shot SP1001 range from 1.4 to 1.7, suggesting that remarkable low-velocity waveguides formed by damaged rocks along multiple fault strands of the WNFZ at shallow depth in the 2014 *M*6 South Napa earthquake. The longest post-S coda (~2.5 s) of FZTWs with largest $(t_C–t_S)/(t_S–t_P)$ ratio (~1.7 s) are registered at stations (numbered from 48 to 54) located within the ~500-600-m wide rupture zone along the main strand of the WNFZ (called WNFm), indicating that fault rocks of the WNFm experienced most severely damage in the 2014 mainshock. Comparatively, we observe FZTWs with 2.1-2.3 s post-S coda durations and 1.4-1.5 $(t_C–t_S)/(t_S–t_P)$ ratios at stations (from 61 to 65, and from 69 to 72) located within ~300-400-m wide WNFe1 and WNFe2, indicating that fault rocks along the east rupture zones experienced slightly less damage than those along the main rupture zone. We observe wavetrains with relative large amplitudes and ~1.5-s post-S coda duration in seismograms recorded at stations (numbered from 32-35) close to the Carneros Fault. These wavetrains are likely the leaking-mode FZTWs produced within the low-velocity waveguide

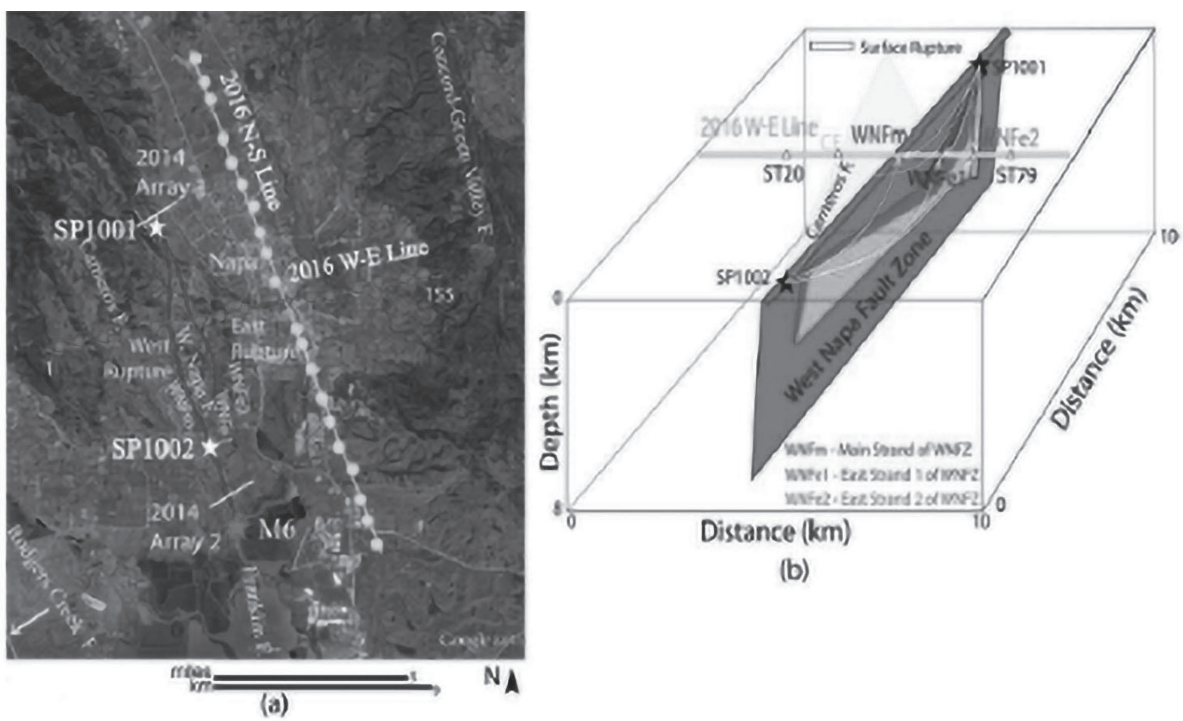

Figure 8. (a) Map shows the 2014 M6 South Napa earthquake (red star), multiple surface ruptures (red lines) along the main and east strands WNFm. WNFel and WNFe2 of the WNFZ, Array 1 and Array 2 (yellow bars) in 2014, the 2016 W-E Line (red line)and N-S Line (green line), 36 in-line shots (red and green circles explosions SP1001 and SP1002 (white stars) and adjacent faults (brawn lines). (b) 3-D volume shows schematic geometry of multiple fault strands of the WNFZ and the CF, which connect at ~3-km depth. White curves denote ray paths from explosions to stations.

when a seismic source is located outside the waveguide. The $(t_C–t_S)/(t_S–t_P)$ ratio of these wavetrains is ~1.0, suggesting that a ~400-m-wide waveguide with more moderate velocity reduction and weak trapping effect exists along the CF than those along the WNFZ at shallow depth. The CF did not rupture in the 2014 *M*6 earthquake although minor slips might occur on it due to strong shaking by the nearby earthquake.

Regarding to shot SP1002, we observe prominent FZTWs with large amplitudes and post-S coda durations of ~4 s at stations located within rupture zones along multiple strands of the WNFZ and ~3 s at stations close to the Carneros Fault (refer to Li *et al*., 2016). The time differences between the P- and S-arrivals are approximately 2.2 s at stations within the WNFZ, and 2.5 s at stations near the CF. The $(t_C–t_S)/(t_S–t_P)$ ratio for FZTWs recorded at the WNFZ is ~1.8, showing remarkable low-velocity damage zones produced along multiple

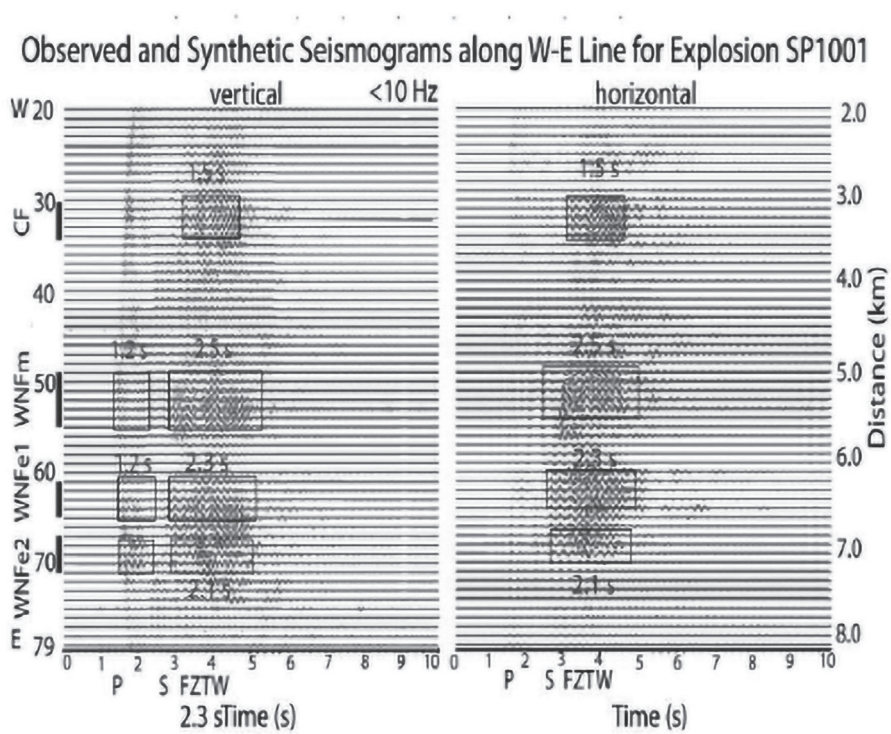

Figure 9. Observed (red lines) and 3D finite-difference synthetic (blue lines) vertical- and horizontal-component seismograms at 60 stations of the 2016 W-E Line for explosion SP1001. Seismograms have been 1-6 Hz band-pass filtered. Large-amplitude FZTWs (in boxes) with 2.5-s, 2.3-s and 2.1-s post-S durations at stations located within the 400-500-m wide rupture zones(marked by vertical bars) on the main fault (WNFm) and east strands WNFel and WNFe2 of the WNFZ. FZTWs with 1.5 s post-S coda duration are at stations within the 400-m wide CF. The duration of FZTWs is the average value of measurements at stations within the rupture zone. We notice P-type FZTWs at stations located within rupture zones. The FZTWs at the adjacent Camneros fault show relatively short S-code duration.

strands of the WNFZ in the 2014 *M*6 earthquake. The post-S durations and $(t_C–t_S)/(t_S–t_P)$ ratios measured at multiple strands of the WNFZ are similar although surface breaks along these fault strands are separated southward, suggesting that rupture zones along multiple fault strands might merge at depth. Therefore, the FZTWs generated by SP1002 detonated on the southern main WNF can propagate northward along multiple fault strands. The $(t_C–t_S)/(t_S–t_P)$ ratio of FZTWs recorded at the CF is ~1.2, showing that the CF has weaker trapping effect than the WNF. Combined with the surface expression and geometry of the WNF and CF, we tentatively explain that the CF runs subparallel to the north WNF, and likely connects the southern WNF-FF at shallow depth. Fault Rocks within the CF could be damaged by historical earthquakes and probably slightly damaged by the 2004 *M*6 mainshock even though it did not rupture in the 2014 South Napa earthquake.

We have synthesized seismograms generated by explosions SP1001 and SP1002, based on the structure model shown in Figure 8b. However, the low-velocity waveguides along WNFm and WNFe1/WNFe2 strands of the WNFZ are 500-m (400-m) and 400-m (300-m) wide in the top layer (second top layer) of the model, within which seismic velocity reduced by 50%, 45% and 40% from surrounding rocks. The CF is 400-m (300-m) wide in the top layer (second top layer) of the model, within which seismic velocity reduced by 35%. These fault traces are separated at the surface (Fig. 8). but we assume that they merge at 2-3 km depth. The 2006 W-E Line is placed across the multiple waveguides. The seismic waves were generated by an explosion source within the WNFm at ~3.5-km (~5-km) from the seismic array for SP1002 (SP1002). Figure 9 shows the 3-D finite-difference synthetic waveforms using these model parameters for comparison with seismograms for explosion SP1001. An explosion source was placed within the main rupture zone. Both P- and S-FZTWs generated by explosion appear at stations located within multiple rupture zones along the WNFZ and the CF. The synthetic FZTW post-S-wave coda durations are comparable with observations at stations located within these low-velocity fault-zone waveguides. The longest post-S coda (~2.5 s) of FZTWs is at stations (from 48 to 54) located within the ~500-m wide rupture zone WNFm, within which fault rocks experienced most severely damage in the *M*6 mainshock. Comparatively, FZTWs with 2.1-2.3 s post-S coda durations appear at stations (from 61 to 65, and from 69 to 72) located within ~400-m wide rupture zones WNFe1 and WNFe2, within which fault rocks experienced slightly less damage than those within the main rupture zone. In contrast, ~1.5-s post-S coda duration is at stations (from 32-35) within the ~400-m wide the Carneros Fault with more moderate velocity reduction and weak trapping effect than those along the WNFZ rupture zones at shallow depth. The synthetic P-FZTWs with ~1.2-s coda durations are also agreeable with those in vertical-component seismograms recorded at

stations within WNFZ rupture zones.

We then computed spectral amplitudes and post-S coda durations in seismogram recorded at 60 stations of the 2016 W-E Line for SP1001 and SP1002 (Fig. 10). We observe largest spectral amplitudes and longest post-S coda durations of FZTWs at stations within multiple rupture zones along the WNFZ and moderate spectral amplitudes and post-S coda durations of FZTWs at stations on the CF. These measurements show remarkable low-velocity waveguides formed by highly damaged rupture zones along multiple fault strands of the WNFZ, which likely connect at depth as they run southward. The CF that had no surface breaks but might be lightly damaged due to strong shaking from the nearby 2014 *M*6 earthquake runs sub-parallel to the north WNF and connects the south WNF-FF so that the FZTWs generated by explosion SP1002 could propagate along the waveguide to seismic stations located within or close to the CF.

DISCUSSION AND CONCLUSION

Using FZTWs generated by 55 on-fault aftershocks of the 2014 M6 South Napa earthquake and recorded on three seismic arrays across the 2014 surface ruptures of the WNF, our 3D finite-difference simulations and analysis of these FZTWs in time and frequency indicate that the WNF zone consists of an ~400-500-m-wide, 5-7-km-deep, waveguide within which seismic wave velocities are reduced by 40 to 50%. Measured S coda durations of these

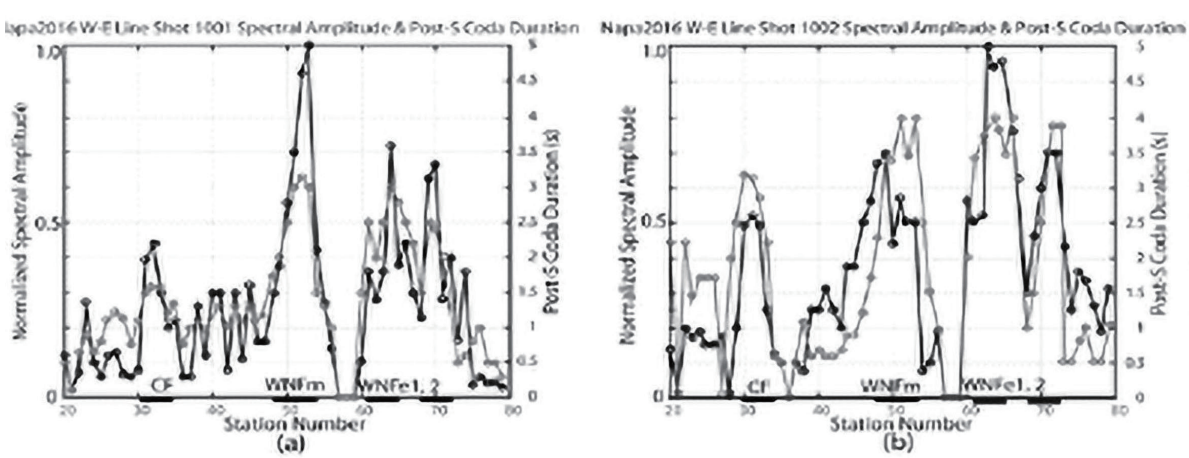

Figure 10. Measured spectral amplitudes (black dots with line) and post-S coda duration (gray dots with line) of seismograms recorded at 60 stations of the 2016 W-E Line for (a) SP1001 and (b) SP1002. Spectral amplitudes are normalized. Larger amplitudes and longer post-$ durations of FZTWs appear within rupture zones (black bars) of the WNFZ.

FZTWs increase with distance between the aftershocks and the recording arrays, suggesting the low-velocity waveguide extends southward to the FF, within which seismic velocities are reduced by 30-35%. FZTWs indicate that the combined WNF-FF zone is at least ~54 km, but potential fields data indicate that the WNF may extend to the Maacama fault, suggesting a WNF-FF zone that is at least 110 km long. FZTWs generated by two explosions detonated within the main surface rupture of the WNF and recorded by a 15-km-long seismic array across the fault zone show that the faulting is highly distributed. Within 1.5 km of the main 2014 surface rupture, there are at least two subordinate fault traces that formed 3- to 6-km-long surface ruptures. Our trial and error forward modeling of FZTWs using a 3-D finite difference code suggests that these subordinate rupture zones form low-velocity waveguides and connect with the main rupture at ~2-3 km depth. FZTWs recorded at the CF, ~1-km west of the WNFZ, suggest that the CF connects with the WNFZ at shallow depths, although there was no surface rupture on the CF during the 2014 event. We suggest that the continuous and widely distributed WNF-FF may pose significant regional hazards from amplification and extended ground shaking along the fault-zone waveguides, even if surface rupture is limited to only a segment of the overall fault zone.

ACKNOWLEDGMENTS

This research is supported by Southern California Earthquake Center's award 15195. Funding and support for data acquisition was provided by the USGS. The Author thanks Rufus Catchings, Mark Goldman and many researchers working in the USGS Napa experiments in 2014 and 2016.

REFERENCE

Baltay, A.S and J. Boatwright (2015). Ground motion observations of the 2014 South Napa earthquake, Seis. Res. Lett., 86, 355-360, doi: 10.1785/0220140232.

Brocher, T.A., A. Baltay, J.L. Hardebeck, J. Polet, E. Langenheim, A.L. Llenos, J.J. Lienkaemper, D.P. Schwartz, J.L. Blair, T. Dawson, K.W. Hudnut, D.R. Shelly, D. Dreger, J. Boatwright, B.T. Aagaard, D. J. Wald, R.M. Allen, W.D. Barnhart, K.L. Knudsen, B.A. Brooks, K.M. Scharer (2015). The *M*6.0 24 August 2014 South Napa earthquake, Seism. Res. Lett. 86, no. 2A, doi: 10.1785/0220150004.

Bryant, W.A. (compiler) (2005). Digital database of quaternary and younger faults from the Fault Activity Map of California, Version 2.0: California Geological Survey.

Byerlee, J. (1990). Friction, overpressure and fault-normal compression, Geophys. Res. Lett., 17, 2109-2112.

Catchings, R.D., M.J. Rymer, M.R. Goldman, R.R. Sickler, and C.J. Criley (2014). A method and example of seismically imaging near-surface fault zones in geologically complex areas using Vp, Vs, and their ratios, Bull. Seismol. Soc. Am., 104, 1989-2006, doi: 10.1785/0120130294.

Catchings, R. D., M. R. Goldman, Y. G. Li, and J. H. Chan (2016). Continuity of the West Napa-Franklin fault zone inferred from guided waves generated by earthquakes following the 24 August 2014 Mw 6.0 South Napa earthquake, Bull. Seismol. Soc. Am. 106, no. 6, 2721-2746, doi: 10.1785/0120160154.

Çelebi, M., S. F. Ghahari, and E. Taciroglu (2015). Unusual downhole and surface free-field records near the Carquinez strait bridges during the 24 August 2014 *M*w 6.0 South Napa, California, earthquake, Seis. Res. Lett., V8, N4, doi: 10.1785/0220150041.

Cochran, E.S., Y.G. Li, P. M. Shearer, S. Barbot, Y. Fialko, and J.E. Vidale (2009). Seismic and geodetic evidence for extensive, long-lived fault damage zones, Geology, v9.37; no. 4, 315–318, (doi:10.1130/G25306A.1; Data Repository item 2009082).

Donnellan, A., J.W. Parker, B. Hawkins, S. Hensley, C.E. Jones, S.E. Owen, A.W. Moore, J. Wang, M.E. Pierce, and J.B. Rundle (2014). Combined UAVSAR and GPS estimates of fault slip for the *M*6.0 South Napa earthquake, Abs. S31G-04, presented at 2014 Fall Meeting, AGU, San Francisco, Calif., 15-19 Dec.

Graves, R.W., 1996. Simulating seismic wave propagation in 3D elastic media using staggered-grid finite differences, Bull. Seis. Soc. Am., 86, 1091-1106.

Graymer, R.W. (2014).Three-dimensional fault framework of the 2014 South Napa earthquake, San Francisco Bay region, California, Abs. S33F-4930, presented at 2014 Fall Meeting, AGU, San Francisco, Calif., 15-19 Dec.

Hardebeck, J.L., and D.R. Shelly (2014). Aftershocks of the 2014 *M*6 South Napa Earthquake: Detection, Location, and Focal Mechanisms, Abs. S33F-4927, presented at 2014 Fall Meeting, AGU, San Francisco, Calif., 15-19 Dec.

Hough, S.E. (2014). Where was the 1898 Mare Island earthquake? Insights from the 2014 South Napa earthquake, 2014 Fall Meeting, American Geophysical Union, San Francisco, California, December 2014, Abs. S44D-03.

Hudnut, K.W., T.M. Brocher, C.S. Prentice, J. Boatwright, B.A. Brooks, B.T. Aagaard, J.L. Blair, J. Fletcher, J.E. Erdem, C.W. Wicks, J.R. Murray, F.F. Pollitz, J. Langbein, J. Svarc, D.P. Schwartz, D.J. Ponti, S. Hecker, S. DeLong, C. Rosa, B. Jones, R. Lamb, A. Rosinski, T.P. McCrink, T.E. Dawson, G. Seitz, R.S. Rubin, C. Glennie, D. Hauser, T.

Ericksen, D. Mardock, D.F. Hoirup, and J.D. Bray (2014). Key recovery factors for the August 24, 2014, South Napa earthquake, U.S. Geol. Surv. Open-File Rep. 2014–1249, 51 p.

Langenheim, V.E., R.W. Graymer, and R.C. Jachens (2006). Geophysical setting of the 2000 ML 5.2 Yountville, California, earthquake: Implications for seismic hazard in Napa Valley, Ca., Bull. Seis. Soc. Am. 96, 1192–1198.

Li, Y.G., P.C. Leary, K. Aki, and P.E. Malin (1990). Seismic trapped modes in the Oroville and San Andreas fault zones, Science 249, 763–766.

Li, Y.G., and P.C. Leary (1990). Fault-zone trapped seismic waves, Bull. Seis. Soc. Am., 80, 1245-1271.

Li, Y.G., K. Aki, D. Adams, A. Hasemi, W. H. K. Lee (1994). Seismic guided waves trapped in the fault zone of the Landers, California, earthquake of 1992, J. Geophys. Res., 99, 11,705-11,722.

Li, Y.G. and J.E. Vidale (1996). Low-velocity fault zone guided waves; numerical investigations of trapping efficiency, Bull. Seis. Soc. Am., 86, 371-378.

Li, Y.G., W.L. Ellsworth, C. H. Thurber, P. E. Malin, and K. Aki (1997). Observations of fault-zone trapped waves excited by explosions at the San Andreas fault, central California, Bull. Seis. Soc. Am., 87, 210-221.

Li, Y.G., J.E. Vidale, K. Aki, F. Xu, and T. Burdette (1998). Evidence of shallow fault zone strengthening after the 1992 *M*7.5 Landers, California, earthquake, Science, 279, 217-219.

Li, Y.G., J.E. Vidale, and K. Aki (2000). Depth-dependent structure of the Landers fault zone using fault zone trapped waves generated by aftershocks, J. Geophys. Res., 105, 6237-6254.

Li, Y.G., J.E. Vidale, D. Oglesby, S.M. Day and E. Cochran (2003). Multiple-fault rupture of the M7.1 Hector Mine, California, earthquake from fault-zone trapped waves, J. Geophys. Res., 108, ESE 11, 1-25.

Li, Y.G., J.E., Vidale, and S.E. Cochran (2004). Low-velocity damaged structure of the San Andreas fault at Parkfield from fault-zone trapped waves, Geophy. Res. Lett., 31, L12S06.

Li, Y.G., P. Chen, E.S. Cochran, J.E., Vidale, and T.Burdette (2006). Seismic evidence for rock damage and healing on the San Andreas fault associated with the 2004 *M*6 Parkfield earthquake, Special issue for Parkfield *M*6 earthquake, Bull. Seis. Soc. Am., 96, No.4, S1-15, (doi:10.1785/0120050803).

Li, Y.G. and P.E. Malin (2008). San Andreas Fault damage at SAFOD viewed with fault-

guided waves, Geophys. Res. Lett., 35, L08304, (doi:10.1029/2007GL032924).

Li, Y.G., G. De Pascale, M. Quigley, and D. Gravely (2014). Fault damage zones of the M7.1 Darfield and *M*6.3 Christchurch earthquakes characterized by fault-zone trapped waves, Tectonophysics, V618, 79-101.

Li, Y.-G., R. D. Catchings, and M. R. Goldman (2016). Subsurface fault damage zone of the 2014 *M*w6.0 South Napa, California, earthquake viewed from fault-zone trapped waves, Bull. Seismol. Soc. Am. 106, 2747-2763.

Marone, C., 1998. The effect of loading rate on static friction and the rate of fault healing during the earthquake cycle, Nature, 391, 69-72.

McGarr, A., M. Boettcher, J.B. Fletcher, R. Sell, M. J. S. Johnston, R. Durrheim, S. Spottiswoode, and A. Milev (2009). Broadband records of earthquakes in deep gold mine and a comparison with results from SAFOD, California, Bull. Seis. Soc. Am., 99, No.5, 2815–2824, (doi: 10.1785/0120080336).

Melgar D., J. Geng, B.W. Crowell, J.S. Haas, Y. Bock, W.C. Hammond, and R.M. Allen (2015). Seismogeodesy of the 2014 *M*w6.1 Napa earthquake, California: Rapid response and modeling of fast rupture on a dipping strike-slip fault, J. Geophys. Res., 120, 14 July 2015, (doi: 10.1002/2015JB011921).

Mooney, W.D. and Ginzburg A. (1986). Seismic measurements of the internal properties of fault zones, PAGEOPH 124, 141-157.

Rice, J.R. (1992). Fault stress states, pore pressure distributions, and the weakness of the San Andreas fault, in Fault Mechanics and Transport Properties of Rocks, eds. B. Evans and T.-F. Wong, 475-503, Academic, San Diego.

Scholz, C.H. (1990). The Mechanics of Earthquakes and Faulting, Cambridge Univ. Press, New York.

Sibson, R.H. (1996). Structural permeability of fluid-driven fault-fracture meshes. J. of Struct. Geol., 18, 1031-1042.

Suess, M., & Shaw, J.H. (2003). P wave seismic velocity structure derived from sonic logs and industry reflection data in the Los Angeles basin, California. J. Geophys. Res., 108 (B3), 2170. doi: 10.1029/2001JB001628.

Vidale, J.E., D.V. Helmberger, and R.W. Clayton (1985). Finite-difference seismograms for SH waves, Bull. Seis. Soc. Am. 75, 1765-1782.

Vidale, J.E. and Y.G. Li (2003). Damage to the shallow Landers fault from the nearby Hector Mine earthquake, Nature, 421, 524-526.

新冠疫情对医学领域的影响以及医疗行业的未来发展趋势

李永田 ▶ 国际生物医学科学学会 洛杉矶

截止 2021 年 9 月 1 日，新冠病毒 COVID-19 大流行已经超过 20 个月，在全球范围内至今还没有看到新冠病毒大流行会很快得到控制的曙光，新的病例还不断增加，病毒的变异株还在不断被发现，我们预计病毒可能会持续存在并成为常态。当然我们更希望在全世界的医学精英的通力合作和先进科技以及疫苗的普及下及早控制。新冠疫情使全球经济都造成了影响，对人类生存，社会发展和医学领域都带来了巨大影响，催生和加快了医学领域的许多行业发展并出现了新的竞争格局，医疗行业的未来发展趋势也有了变化。在这个前所未有的时代，我们讨论一下新冠疫情对医学领域的几个重大影响和医疗行业在未来的发展趋势，以及未来医院和医疗系统关注哪些重点，为 2021 年及以后做好准备。

一、新冠病毒流行把 mRNA 制药行业推向了新的高潮

我们都知道辉瑞和莫德纳制药公司的 mRNA 疫苗在新冠病毒流行中最先得到美国 FDA 紧急授权使用，并且在 21 年 8 月 23 日辉瑞疫苗第一个被 FDA 正式批准，其审批速度已经超出正常审批过程。mRNA 疫苗的大规模应用，在人类历史上属于首次。正是因为这个挑战性的实践，加速了科学家和投资者把 mRNA 疫苗看作了是一次新的机遇，加快了将 mRNA 疫苗技术应用到其他疾病范畴。

今年 4 月 Malvern Panalytical 科技公司和著名的 ONCOLOGY 杂志编委会成员 Copur 博士同时认为，mRNA 疫苗技术开启了疫苗学或癌症免疫治疗的新时代。三个

多月前，全世界第五大制药厂赛诺菲宣布，向 mRNA 疫苗设施投资 4.76 亿美元。

科学家们也将继续探索多种癌症的 mRNA 治疗方法。正如德克萨斯大学 MD 安德森癌症中心的研究人员所解释的那样，mRNA 疫苗将指导患者的细胞根据肿瘤的基因突变产生蛋白质片段，促使免疫系统寻找其他具有突变蛋白质的细胞并攻击剩余的肿瘤细胞。中国上海斯微生物科技也在今年 6 月 1 日正式完成了近 2 亿美元融资，开发自主知识产权的 mRNA 疫苗，多线推进疫苗用于新冠病毒、肿瘤及其他罕见病的治疗。

除了 mRNA 疫苗已经对艾滋病毒、狂犬病和流感在人体试验之外，科学家说 mRNA 疫苗的下一个重点治疗的一些疾病将是疟疾，结核，乙型肝炎，囊性纤维化等。休斯顿卫理公会研究所 RNA 治疗项目医学主任 John Cooke 博士说“mRNA 疫苗几乎可用于所有病原体靶向治疗，输入了刺激免疫反应的特定蛋白质的代码，基本作用上是无限的。”

可以预见，mRNA 制药行业将迎来发展的春天。

二、合作乃是控制疫情大流行和今后工作的方向之一

全球医疗机构乃至各国政府在如何应对突发的公共卫生事件上，对采取各种安全措施、数据可用性和基础设施的建设等关键问题上，在 COVID-19 大流行中都暴露了其脆弱性。很明显依靠任何一个医疗机构自己的能力“单独行动”是不可能取得抗疫的全面胜利。尤其是医疗物资的保障上，供应商和非医疗公司纷纷介入，要共同提供资源，共同临时合作来应对危机。

21 年 8 月 29 日 CNN 的报道显示，佛罗里达州、南卡罗来纳州、德州和路易斯安那州的几家医院氧气的供应出现问题，正面临着氧气即将耗尽的风险。医疗设备性能改进公司的高级主管 Donna Cross 告诉 CNN，随着 COVID-19 病例的持续上升，对氧气供应的需求越来越大，医院也无法跟上这些需求的步伐。

成功的医疗机构或医疗组织将建立在这种思维方式的基础上，找到缩小差距的方法，并与具有解决问题的独特技能的合作伙伴进行创新。首先是在疫苗，药物和医疗器械的开发和生产方面，通过各种合作，研发应对病毒的检测、病毒的抑制和治疗的相关药品都受到了极大重视。预期会有更多医药公司参与 mRNA 疫苗的生产和创新药物以及医疗器械的研发与制造，以缓解全球疫苗和呼吸器以及氧气等抗疫必须品的短缺。

◎ 建立一个协作生态系统并且尽可能合作

GEOFFREY MARTIN 是 GE 医疗咨询公司的首席执行官，他首先强调要建立一个具有战略性和敏捷性的供应链。不然突然的疫情会造成手忙脚乱。MARTIN 认为成功的医疗物品的供应链正在成为提供医疗过程的关键因素和重要组成部分，这个重要性在以前的医疗实践中从未见过。我们看到一种趋势就是又回到了传统的时代，要采用更多的自我分销模式，而不是希望分销商的准时交货。要选择可靠的供应商和备用供应商，不要过度依赖一个供应商。随着许多医院争先恐后地寻找与大流行相关的供应品时，要在价格、性能和信任之间取得战略平衡。但是获得最低价格不是唯一的考虑，重要的是在危机中要对你的订单有“优先考虑”。通常供应商规模小没有关系，地理位置更近和以最快的速度和确定能获得所急需医疗物资最为重要，以便在需要关键物品时可以迅速拿到手上。

期望在医疗用品供应链中看到更多自动化软件和人工智能 (AI)。除了将员工从重复性工作中解放出来之外，这些技术还可以帮助决策者识别发展的趋势并为员工提供资源。例如，在医疗机构内可以分析预测并提醒管理人员注意将来的疾病状态及其相关的供应需求趋势。供应链经理可以使用人工智能工具来掌握新的运输物流，将供应物品运送到广泛分散的家庭医疗场所等。

◎ 合作竞争是医疗领域的一种可行的策略

MARTIN 认为，合作竞争是医疗领域的一个主要趋势。当一些供应商将大型商店、全国性医药连锁店视为威胁的时候，其他供应商则看到了机会。他们的战略是利用这些有实力的大型商店作为参与者来降低医疗成本，增加下游市场的占有率并专注于核心专业服务，同时保持与患者的高度联系。比如在一些供应商的努力下，将简单的诊断服务和慢性病管理与像 CVS 和沃尔玛这样的大型连锁店合作，提供一些有价值的服务，确定与零售机构合作，填补这一空白，增加了病人访问量并以更低的成本提供更好的患者服务，供应商也得到了很好的回报。

这样做的结果，不但改善社区健康服务，同时扩大了市场，服务可以有意地对社区健康和合作伙伴产生重大影响。例如，在 40 岁及以上的女性大约一半没有进行乳房 X 光检查。如果大型零售商能提供乳房 X 光检查服务会成功地激励这一人群，接受店内乳房 X 光检查的方便服务。

三、新冠疫情大流行加快了在线远程数字医疗平台建设的步伐

◎ 大量资本涌入远程虚拟医疗行业

根据 CB Insight 的最新数据，2021 年第一季度的 139 项远程医疗投资达到了 42 亿美元，几乎是去年同期病毒流行开始时筹集的 22 亿美元的两倍。这是有史以来全球远程医疗在一个季度的最高投资。

第一季度的资金注入，催生了 Modern Health 等 6 家公司成为远程医疗领域的“独角兽”，一家公司的估值达到 10 亿美元。此外，由投资公司 Northpond 领投，给一家远程护理管理平台 Current Health，在大流行期间收入同比增长 3,000%。

◎ 随着疫情远程虚拟医疗的应用迅速增加

首先回顾一下疫情开始时候的的虚拟初级保健就诊，在 2020 年 2 月，美国只有不到 1% 的医疗保险初级保健就诊是通过远程医疗进行的；到 4 月，在大流行的推动下，短短两个月通过远程医疗进行该初级保健就诊的已上升至 43%。随着患者和医生都采用新的虚拟化就诊方式，这种趋势持续增长。不断变化的市场需求和不断发展的战略模式要保持一致，对未来医疗体系的发展非常重要。

新冠疫情开始前后，美国曾经做过一个调查，指出在疫情之前 90% 以上的病人不使用远程医疗，而到疫情爆发后恰恰相反，有近 90% 都在使用，现在已经变成常态。因此有人认为，即使是疫情结束后，仍然会有 70% 的病人继续使用远程医疗。可以想象，将来的医疗体系如果没有远程医疗是不完美的。医院普通病房的需求会下降，家庭病床的数量会增加。

◎ 远程虚拟医疗的临床适用病种或范围

都哪些疾病适用于远程医疗呢？美国的一些医学专家认为，有 4 类疾病适用于远程医疗。首先是慢性疾病患者的医疗管理，包括高血压等慢性心血管疾病，糖尿病，代谢和免疫性疾病；其次是非急性医疗问题，比如：心理与精神健康，肌肉和关节问题和诸如感冒等引起头疼或周身不适的一些小毛病；第三类是健康保健问题，包括疾病的预防等；第四类是会有少部分急诊后的随访。所有这些，神经和精神疾病将是远

程医疗的一个重要服务方向。

另外，高度专业化重症监护（ICU）可以通过远程医疗服务，使得小型农村医院可以获得这个机会以改善患者的 ICU 监护，不然这些偏远的农村医院很难招聘这些专业人才，例如呼吸血气检测，专科放射医生，IT 人员和客户服务代表等。

◎ 远程虚拟医疗的前景

新冠疫情加快了全球的远程医疗的建设，疫情也加快了中国互联网医疗的建设。现在需要抓住这个机会求发展，将来没有在线远程数字医疗服务的医疗机构是不完美的。可以肯定地说，包括在线门诊咨询，病情随访，远程会诊，网上药店等等都会受到包括病人本身，医疗行业乃至政府等极大地关注，远程医疗会得到更好的发展。美国远程医疗管理平台 Current Health 首席执行官 Chris McCann 在一份声明中表示：“在接下来的 5 年中，我们将看到大部分医疗服务都在患者家中提供，医院将专门用于重症监护、创伤和手术”。也有其他一些医疗领域专家认为，到 2040 年，很多医疗实践将在病人家里、门诊或虚拟环境中提供。

◎ 远程虚拟医疗发展中期待的配套项目及医疗机构需要思考的问题

为了适应上述远程虚拟医疗的发展，人工智能和自动化也势必会以更快的速度在医疗领域占据一席之地。比如，人工智能在放射医学领域的加快应用，不但可减少放射科医生的冗余任务、消除基于偏差的读取错误、识别图像中的数据模式以预测风险并增强工作流程，而且可以对快速远程虚拟医疗提供极大的方便。美国 GE 医疗公司与英特尔的合作已经在使用通过边缘和云部署的数字成像解决方案来增强患者诊疗服务，并用以降低医院和医疗系统的成本。两家公司共同预计，他们的解决方案将通过提高资产绩效、降低患者风险和放射线剂量暴露（具有更快的图像处理速度）以及加快诊断和治疗时间来提供更高的医院效率。

远程虚拟医疗对病人及医疗资源的管理需要实时信息来推动，许多大型医疗机构正在利用实时信息来推动医疗流程的管理。例如，指挥中心软件平台需将系统工程、预测分析和问题解决相结合，以管理进出医疗系统的患者流量，同时旨在保持临床质量、安全和患者体验。

自动化正在简化严重依赖重复性任务的医疗业务的工作，也对非临床领域的自动

化同样提出要求。例如医疗用品供应链和客户服务等。我们期待在医疗领域看到新的传感器（HL7、摄像头）等新型设备，以加快远程虚拟医疗服务的能力。

在疫情下，中国工信部日前发文倡导积极发挥人工智能应用，鼓励攻关并生产相关的辅助诊断智能设备、快速测试方法等，助力疾病智能诊治。进一步推进远程医疗和智慧医疗的发展，解决医疗资源短缺的问题。从而为制造企业带来新的发展机遇。

为了适应远程虚拟医疗的发展，要解决预约就诊的效率和透明度的问题，比如一些患者可能需要等待数周或数月才能预约，并且对何时可以获得检查结果只有一个模糊的概念。医疗机构需要评估当前阻碍远程就诊病人满意度的障碍，并部署分析和以患者为中心的技术，以提高医疗的便利性、速度和透明度。例如，当美国西海岸卫生系统采用精确预约程序最大限度地减少影像检查之间的时间浪费时，他们每年能够多开辟 5,000 个新的检查，患者的预约时间可以更快。为了实现这个目标，要求医疗机构的预约程序就应该像我们在网络上购买东西一样，从下单到交货每分钟都能跟踪它们的位置。患者期望他们的医疗服务提供者具有同样高的效率和透明度。

虽然患者希望远程虚拟医疗的便利性和易用性，但个性化医疗仍然是他们忠诚度的试金石。根据 2020 年对医疗保健消费者的一项调查，“理想”的医疗体验需要个人接触，无论这种接触是虚拟发生还是亲自发生。患者表示，临床医生花时间倾听、表现出医生的关心和相互清晰的沟通是最重要的。

为了改善这些服务，为了使改进的努力富有成效，医疗机构推动的计划必须对其结果有衡量标准。例如，一家主要的学术医疗中心创建了一个交流培训计划，教授和医生在与患者互动时遵循的最佳实践就是，患者评价医生“明白患者的意思”“尊重患者”“解释清楚”。结果，一年之后，患者对医生的正面评价比例上升了 9 个百分点。

除了这些期待之外，在新冠病毒疫情的影响下，给医疗领域和相关机构提出一些新的问题：

虚拟医疗和数字化是否正在成为我们作为一个医疗机构的工作战略的一部分？我们如何才能更好地利用虚拟方式来创建更安全、更高效的诊疗方式？我们如何利用数据和人工智能来提高生产力并改善临床结果？

新冠疫苗浅析

刘西平 ▶ PhD, NantWorks/ConjuChem, Culver City, CA 90230, USA

从新冠疫情爆发至今已近两年，并已构成全球性大流行。科学家和公众都参与其中，血清阳性、中和抗体、疫苗证书和突破性感染等术语已为大众所熟悉。人们对新冠病毒和疫苗都有了一定了解，也产生了许多疑问。有人会认为接种疫苗后就不会再感染新冠病毒；有人又认为疫苗没什么作用，就算接种疫苗后还会有染上新冠病毒的可能性。事实上，世界上确实还没有任何一种疫苗可以达到 100% 的有效，所以全剂量接种疫苗者仍有可能染病。本人曾参加过病毒以及肿瘤疫苗的研究和开发工作，对疫苗的特性有一些初步认识和体会，随着新冠疫苗的推出，温故而知新。在美国华裔教授学者协会 2021 年新春联欢晚会上，很荣幸给大家做了一个有关新冠疫苗的演讲。最近协会专刊正在征稿，承蒙协会会长马胜兴教授之邀将我演讲的内容做了一些更新和编辑，希望在当前新冠病毒不断突变的情形下对了解我们身体是如何进行抵抗病毒感染以及新冠疫苗所诱导的抗体是如何发挥作用有所帮助。本文从世卫组织的“疫苗解释说明”系列文章中引用了许多关于疫苗的信息，从疫苗的作用原理、制造方式到确保安全，也参考了许多关于疫苗的文献和报告，在此一并致谢。

一、疫苗是如何发挥作用的？

在疫苗尚未存在的时代，是一个比现在要危险得多的世界。如今完全能够避免的疾病，在当时每年会夺走数以百万计的生命。在公元 18 世纪后叶，天花是一种有高度传染性的疾病，当时的患者死亡率约为 30%。英国医生爱德华·詹纳注意到，挤奶工人可能会患上轻度的牛痘，但却很少进一步染上致命的天花，这使他意识到种“牛痘”

可预防天花。为了证实这一想法，詹纳将牛痘接种到一个 8 岁男孩手臂，让孩子患了牛痘。在男孩康复后，詹纳又给这孩子接种了天花痘，不出所料，这孩子没有出现天花病症。也就是说牛痘令这名男孩对天花产生了免疫。1798 年，詹纳的实验结果公布于世，“疫苗”这个词第一次出现了。英文的“Vaccine”的词源正是来自于拉丁文的“Vacca”（母牛）。在过去一个世纪，疫苗帮助全世界大幅度减少了很多疾病的伤害性。在麻疹疫苗于 1960 年问世之前，每年约有 260 万人死于这种疾病。而麻疹疫苗令 2000 年至 2017 年间的麻疹致死人数减少了 80%。在几十年前，数百万人患上脊髓灰质炎，导致肢体瘫痪或死亡，现在小儿麻痹症几乎消失了。

要真正了解疫苗是如何发挥作用的，首先要了解我们的身体是如何抵抗疾病的。当病原体（例如新冠病毒）侵入我们的身体时，它们会对人体发起攻击并大量繁殖。这种入侵称为感染，是导致疾病的原因。人体有许多防御病原体的方法。皮肤、粘液和纤毛都可充当物理屏障，首先是防止病原体进入身体。如果病原体确实感染了身体，便会触发身体内的免疫系统，对病原体进行攻击和清除。人类免疫系统可分为两大类：一类是先天免疫又称固有免疫，是指机体先天具有的正常生理防御功能，对各种不同的病原体的入侵作出相应的免疫应答。天然杀伤细胞，巨噬细胞，单核细胞，嗜中性粒细胞，肥大细胞和树突细胞是参与先天免疫细胞的例子。这些细胞通过吞噬作用破坏病原体。与先天免疫系统不同，另一类是后天免疫又称获得性免疫，是一种经由与特定病原体接触后，产生能识别并针对特定病原体启动的免疫反应。在后天免疫中 T 细胞和 B 细胞分别负责细胞免疫和体液免疫。T 细胞不产生抗体，而是细胞直接起作用。所以 T 细胞的免疫作用叫作 " 细胞免疫 "。B 细胞是通过产生抗体起作用。抗体存在于体液里，所以 B 细胞的免疫作用叫作 " 体液免疫 "。其中 IgG 是血清中含量最多的免疫球蛋白，具有抗菌、抗病毒、抗毒素等特性，对毒性产物起中和、沉淀、补体结合作用。后天免疫可以在初次感染某种病原体后产生免疫记忆，并在下一次感染这种病原体时产生更强的抵抗力。病原体感染能使人类产生免疫力，防止再感染。疫苗正是通过模拟病原体感染来诱导机体的免疫记忆，当接种者真正遇到病原体入侵时可免除或减少疾病危害。人类先天免疫和后天免疫的组成如图 1 所示。

二、疫苗是如何进行开发的？

所有疫苗都含有能够产生免疫反应的活性成分即抗原，或者是含有能够产生抗原的模板（核糖核酸或脱氧核糖核酸）。根据疫苗抗原的特性主要分为三类：一是全病

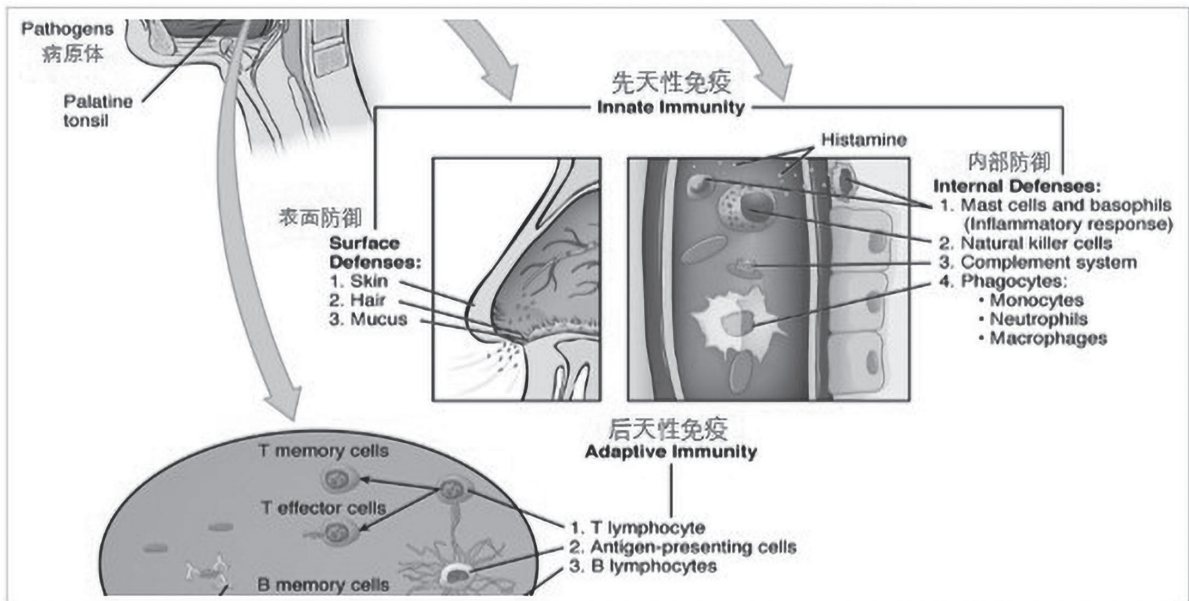

图 1. 人类免疫系统可分为两大类：先天性免疫和后天性免疫。

毒疫苗，包括灭活和减毒疫苗；二是蛋白疫苗，包括编码蛋白质的核酸疫苗；三是多肽疫苗。除了抗原外，不同疫苗可能还含有一些其它成分，主要有：1. 稳定剂：它们可以是糖（乳糖、蔗糖）、氨基酸（甘氨酸）、明胶和蛋白质。稳定剂可防止疫苗内部发生化学反应，并防止疫苗成分附着在疫苗瓶上。2. 表面活性剂：它们可防止疫苗液体形式的元素沉淀和结块。3. 佐剂：有些疫苗还含有佐剂。佐剂通过将疫苗在注射部位保留更长时间，或者刺激局部免疫细胞，提高对疫苗的免疫反应。在一种疫苗开发中除了抗原是新的成分外，其它成分早已在其它疫苗中安全使用过。

与药物一样，每种疫苗都必须经过广泛而严格的测试，以确保其安全性。一种新的疫苗首先要在动物身上进行测试，以评估其安全性及其预防疾病的潜力。如果疫苗能够引发免疫反应，它将分成三期在人体临床试验中进行测试。第一期：为少数志愿者接种疫苗，以评估其安全性，确认能产生免疫反应，并确定正确的剂量。通常在这一阶段，疫苗测试是在年轻和健康的成年志愿者中进行。第二期：随后为数百名志愿者接种疫苗，以进一步评估其安全性和产生免疫反应的效能。这一阶段的参与者与疫苗拟接种对象具有相同的特征（如年龄、性别）。在这个阶段通常要进行多个试验，对不同年龄组和不同疫苗配方作出评估。这一阶段通常还包括没有接种疫苗的一组人作为对照组，以确定接种组的变化是由疫苗引起，还是偶然发生的。第三期：为成千上万的志愿者接种疫苗，并与没有接种疫苗但接受了对照产品的类似人群进行比较，以确定疫苗对其旨在预防的疾病是否有效，并考察其在更广大人群中的安全性。在第

二和第三期试验中，志愿者和试验研究者均不知道被接种者中谁接种了正在测试的疫苗，谁接受了对照产品，这种试验方法又称为“双盲法”。在试验结束和确定了全部结果后，志愿者和试验研究者才被告知谁接种了疫苗，谁接受了对照产品。根据各组中的患病人数，按受试者是否接种了疫苗计算患病的相对风险。由此即可算出疫苗效力，即疫苗在多大程度上降低了患病风险。在得出所有这些临床试验的结果后，还需要采取一系列步骤，包括审查疫苗的有效性和安全性，以进行监管和公共卫生政策审批。

三、 新冠疫苗的靶点是什么？

新冠肺炎（COVID-19）是一种由新发现的冠状病毒（SARS-CoV-2）引起的传染病。大多数感染新冠毒病的人会出现轻中度呼吸系统疾病，老年人以及那些患有心血管疾病、糖尿病、慢性呼吸系统疾病和癌症等基础病的人更容易发展为重症。新冠病毒是一种 RNA 病毒，属于冠状病毒科乙型冠状病毒属严重急性呼吸道综合征相关冠状病毒种。它与 2003 年引发非典型肺炎的 SARS 病毒同科同属不同种，是已知的第七种可感染人类的冠状病毒。新冠病毒基因组长度约三萬個核苷酸，组成上类似 SARS 病毒，病毒粒子由宿主细胞提供的脂质双层所包裹，其中含有核酸及核衣壳蛋白（N），还有三种主要蛋白：包膜蛋白（E）、膜糖蛋白（M）和刺突蛋白（S）。大量的研究分析表明新冠病毒感染宿主细胞是通过刺突蛋白与宿主细胞表面受体血管紧张素转换酶 2（ACE2）结合介导的。刺突蛋白是一种由三个相同亚基以非共价键结合形成的同源三聚体，每个亚基由 1273 个氨基酸构成。刺突蛋白蛋白的序列主要包括 N 端结构域（NTD）、受体结合结构域（RBD）和跨膜结构域（TD）等。由于刺突蛋白与宿主细胞受体 ACE2 结合是新冠病毒感染周期中的关键步骤，可以推测如果能够阻止或封闭刺突蛋白蛋白与宿主细胞受体 ACE2 结合，就能起到预防新冠病毒的感染。这为新冠疫苗研发策略和靶点定位提供了方向。

世界上许多研究机构已经广泛开展了针对新冠病毒中和抗体的研究工作，大都采用针对刺突蛋白或 ACE2 蛋白的中和抗体来阻断刺突蛋白与 ACE2 之间的结合，从而阻断病毒进入细胞。目前已有 8 种新冠疫苗获批在人体使用，另有 13 种新冠疫苗获得有限批准使用，还有 35 种新冠疫苗正在临床 III 期试验中。根据不同的开发技术平台，可将新冠疫苗分成四大类。第一类就是 mRNA 疫苗，由美国辉瑞（Pfizer）和莫德纳（Moderna）研发； 第二类是蛋白质疫苗，由美国诺瓦瓦克斯（Novavax）研发；

第三类是采用腺病毒作为载体型，至少有三家公司在研发，包括美国强生（J&J），英国阿斯利康（AstraZeneca）以及中国康希诺（CanSinoBIO）。第四类疫苗是灭活病毒疫苗，主要由三家中国公司研发，分别是北京科兴（Sinovac）；北京生物制品研究所以及武汉生物制品研究所。除了灭活病毒疫苗外，所有其它三类疫苗均采用刺突蛋白作为唯一抗原。灭活病毒疫苗除了刺突蛋白以外，还含有病毒的其它成分也可以作为抗原。新冠疫苗的靶点和作用机制如图 2 所示。

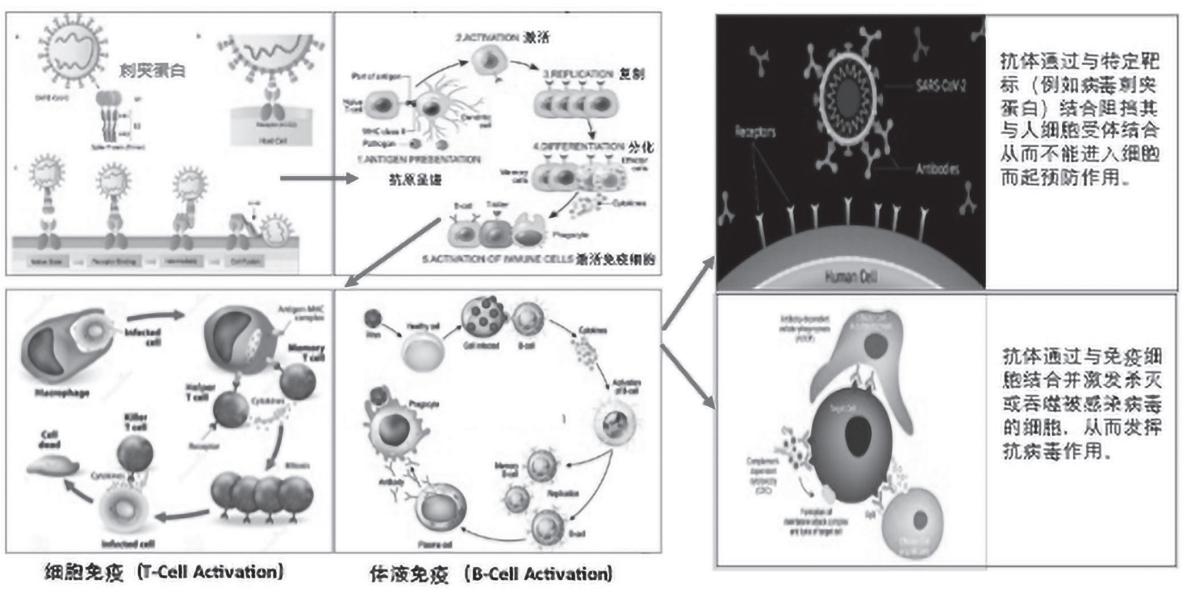

图 2. 新冠疫苗的靶点和作用机制。

四、疫苗效力的影响因素有哪些？

根据要求疫苗须达到 50% 或 50% 以上的效力才能获得批准。在临床试验完成后，通过比较各组中的患病人数，按受试者是否接种了疫苗计算患病的相对风险。由此即可算出疫苗效力，即疫苗在多大程度上降低了患病风险。如果疫苗效力很高，接种疫苗组中患病人数会比接种安慰剂组中患病人数少得多。例如，如果一种疫苗经证实的效力为 80%，这就意味着，在接受临床试验者中，接种此疫苗的受试者患病风险比接种安慰剂的受试者低 80%。这是通过比较接种疫苗组与安慰剂组的病例数计算出的结果。80% 的效力并不意味着接种疫苗组中 20% 的人将患病 . 疫苗有效率计算如示意图 3 所示。

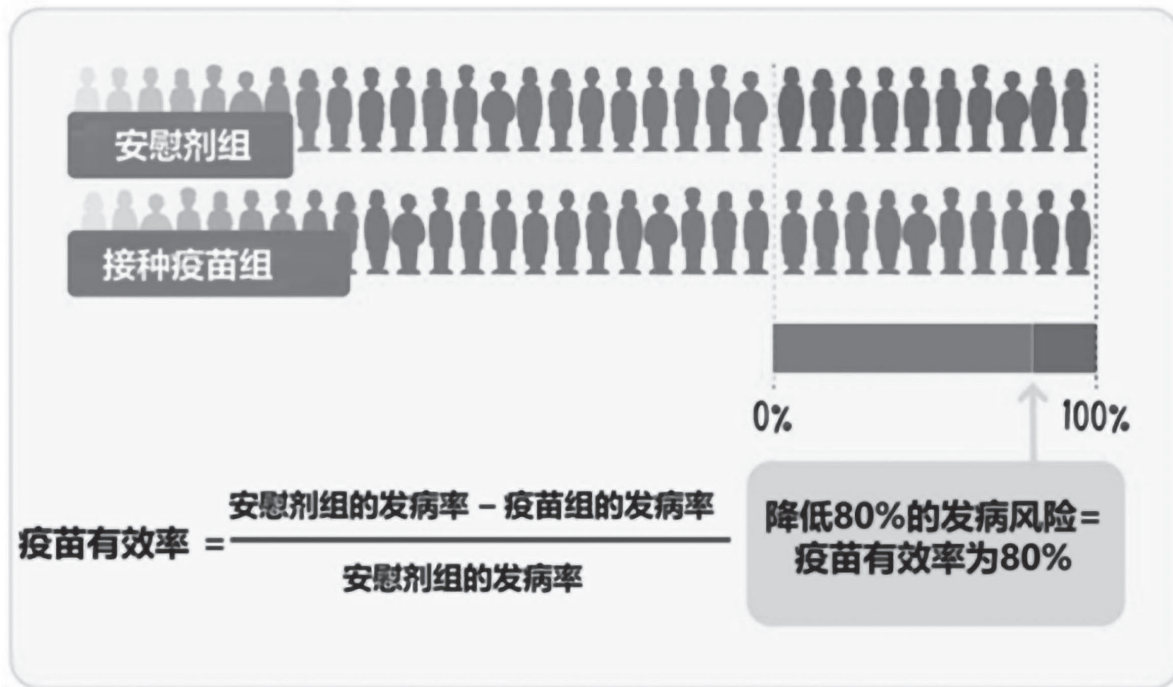

图 3. 疫苗有效率计算示意图。

目前获批的新冠疫苗均采用灭活原始病毒或来自于原始病毒刺突蛋白作为抗原，因此所诱导出来的抗体特异性是针对原发株的。病毒在自我复制时会发生一些变化，这些变化被称为“突变”。具有一个或多个突变的病毒称为原始病毒的“变异株”。大多数病毒突变对病毒引起感染和疾病的能力几乎没有影响。但是当病毒突变发生在某些部位时，比如刺突蛋白受体结合结构域（RBD）与 ACE2 相互作用位点，就有可能影响到病毒的特性，造成传播容易程度、疾病严重程度或疫苗效力强弱发生改变。现有 4 种变异株包括英国阿尔法（alpha, α），南非贝塔（beta, β），巴西伽玛（gamma，γ），以及印度德尔塔（delta, δ）需要特别关注（Variants of Concern (VOC)）。新冠病毒发生了突变，现在接种的疫苗还有效吗？无论是核酸疫苗、病毒载体疫苗还是灭活疫苗都会引发涉及一系列抗体和细胞的广泛免疫反应，一般来说病毒的变化或突变不会使疫苗完全无效，或多或少能提供一些针对变异株的保护。根据 Markus Hoffman 等报道来自 SARS 病毒感染的患者血清可以部分交叉中和新冠病毒刺突蛋白驱动的入侵并揭示了新冠病毒和非典病毒之间的重要共性[1]。从这个结果上看，在短时间内新冠病毒发生小规模突变对新冠疫苗的保护效果会有影响但不会完全没有作用。Jamie Lopez Bernal 等于 2021 年 7 月 21 日在新英格兰医学杂志发表了新冠疫苗对德尔塔（delta, δ）变异株的预防效果[2]。他们发现在已接种第二剂辉瑞疫苗后，该疫苗对两种变异株的预防效果差异不大：对 alpha 变异株的效果为 93.7%（95% CI，91.6 ～ 95.3），对

delta 变异株的效果为 88.0%（95% CI，85.3 ～ 90.1）。新冠疫苗针对 Alpha 和 Delta 变异株有效性的比较如图 4 所示。

影响疫苗效力的另一个因素是接种后疫苗效力能持续多长时间？已有报道接种疫苗后所诱导的抗体滴度随着时间延长会有所下降，针对病毒感染的保护力将减弱发生突破感染。从发表了的临床资料来看，接种疫苗后尽管有突破感染的病例，但大多没有症状，或症状很轻，几乎没有重症病人[3]。2021 年 9 月 5 日，中国科学院研究员王祥喜团队发表论文《接种第三剂灭活疫苗能够增强抗新冠病毒回忆应答的强效性、广谱性和持续性》[4]。这项研究通过对新冠早期康复者、接种 2 剂和 3 剂灭活疫苗志愿者血清学分析，发现接种 3 剂灭活疫苗的血清样本表现出更为迅速的免疫应答反应、更加持久的体液免疫反应，以及对诸多突变株包括德尔塔（delta, δ）等更加广谱的中和能力。这为接种第三剂灭活疫苗提供了理论依据。

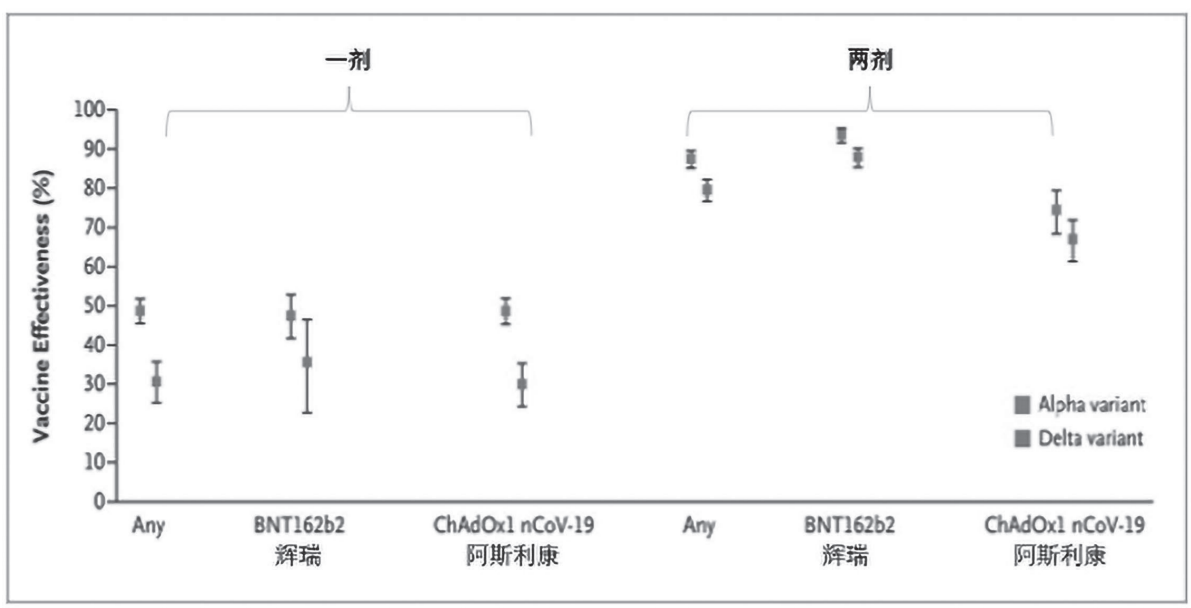

图 4. 新冠疫苗针对 Alpha 和 Delta 变异株有效性的比较。

五、 结语

疫苗已经证明能有效对抗现有变异株，尤其是能有效预防重症、住院和死亡。但一些变异株对疫苗预防轻症和感染的能力造成了一些影响。这意味着，病毒变化或变异不太可能使疫苗完全无效，但由于现有疫苗对变异病毒的效果下降，每个人对疫苗产生反应不一，而且每个人免疫后抗体滴度高峰和持续时间不一样，疫苗需要加强在所难免。根据变异株而设计的第二代新冠疫苗也将很快面世，以适应新的病毒变异。

所幸的是，当代科学技术使疫苗的升级换代相对容易，因佐剂辅剂等都没改变，临床试验相对可以缩短。同时人类不单只在疫苗上有成功的策略，在治疗上也会找到确实可靠的方法。

六、参考文献

1. Markus Hoffmann, *et al*. SARS-CoV-2 Cell Entry Depends on ACE2 and TMPRSS2 and Is Blocked by a Clinically Proven Protease Inhibitor. *Cell*. Volume 181 Issue 2 Pages 271-280.e8 (April 2020).
2. Jamie L Bernal, *et al*. Effectiveness of Covid-19 Vaccines against the B.1.617.2 (Delta) Variant. *N Engl J Med*. 2021; 385:585-594.
3. Nawal Al Kaabi, *et al*. Effect of 2 Inactivated SARS-CoV-2 Vaccines on Symptomatic COVID-19 Infection in Adults. *JAMA*. 2021;326(1):35-45.
4. Kang Wang, *et al*. A third dose of inactivated vaccine augments the potency, breadth, and duration of anamnestic responses against SARS-CoV-2. This article is a preprint and has not been peer-reviewed.

特別報導

讓世界充滿愛德華情

朋友們好! 我是惠玲,
大家多保重啊, 我爸爸媽媽九十歲了,
他們心明眼亮, 關節好, 好開心啊. 真
的要特別謝謝愛德華的美國心腦康,
特效眼明素和強骨質素. 我老公的最
愛是美國蟲草至尊, 真的棒啊!
大家盡量少出門, 外出一定戴口罩, 勤
洗手. 多關心父母家人, 讓大家都早上
美國靈芝尊, 晚上特效養肝素, 好朋友
們都幸福平安, 開心快樂!

太棒啦

親愛的前大洛杉磯最高行政長官
Antonovich和夫人
關心您

9552 Las Tunas Dr., Temple City, CA 91780
電話: 626-821-9878
傳真: 626-821-0380
免費電話: 1-888-6697-888
www.edvip.com

FARMERS INSURANCE

FIANNA LI

Agent

Fianna Li Agency

4110 EDISON AVE STE 202
CHINO, CA 91710
Tel 909-590-3588
Cell 626-905-8393
Fax 877-275-1036 CA Producer LIC 0M81277
fli@farmersagent.com

我们不仅仅是您的保险经纪，更是您的责任与资产管家

About Us

Farmers Insurance 是全美最大的几家保险公司之一，主营车子，房屋，商业，劳工，人寿保险及理财产品。而我们办公室更是致力于全方面高品质的专业服务。

Our Advantages

- 全面安心的保障
- 专业高效的理赔
- 耐心细致的服务

Our Business

商业/劳工保险

专精餐饮，仓库，零售店铺，贸易，商业地产，批发业，海外仓等

车辆/房屋保险

专业且迅速的理赔团队，律师团队及我们经纪办公室为您的保单保驾护航

人寿保险

多种 Term Life 保险价格优惠，储蓄型寿险为您量身定制退休计划

909-590-3588
fli@farmersagent.com
877-275-1036
www.farmersinsurance.com

美国长寿源有限公司
US LONGEVITY SOURCE INC.

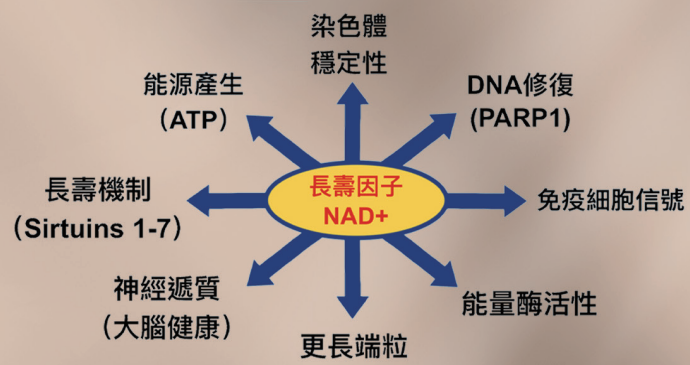

联系电话：3109976120
www.sodlongevity.com

精选保险理财
STAR CHOICE INSURANCE SERVICES

加州健保：个人，团体

- 医疗保险
- 人寿保险
- 汽车保险
- 房屋保险
- 商业保险
- 劳工保险

AMY CHOI 徐浩婷

909-590-3588
626-215-6601

Ca license: 0B93747

4110 Edison Ave #202, Chino, Ca 91710
E-mail: amychoi@starchoiceinsurance.com